INFORMATION TO USERS

This manuscript has been reproduced from the microfilm master. UMI films the text directly from the original or copy submitted. Thus, some thesis and dissertation copies are in typewriter face, while others may be from any type of computer printer.

The quality of this reproduction is dependent upon the quality of the copy submitted. Broken or indistinct print, colored or poor quality illustrations and photographs, print bleedthrough, substandard margins, and improper alignment can adversely affect reproduction.

In the unlikely event that the author did not send UMI a complete manuscript and there are missing pages, these will be noted. Also, if unauthorized copyright material had to be removed, a note will indicate the deletion.

Oversize materials (e.g., maps, drawings, charts) are reproduced by sectioning the original, beginning at the upper left-hand corner and continuing from left to right in equal sections with small overlaps.

Photographs included in the original manuscript have been reproduced xerographically in this copy. Higher quality 6" x 9" black and white photographic prints are available for any photographs or illustrations appearing in this copy for an additional charge. Contact UMI directly to order.

Bell & Howell Information and Learning
300 North Zeeb Road, Ann Arbor, MI 48106-1346 USA

UMI®
800-521-0600

Singular Value Decomposition of Arctic Sea Ice Cover and Overlying Atmospheric Circulation Fluctuations

by

Dingrong Yi

Department of Atmospheric and Oceanic Sciences
McGill University
Montreal

A thesis submitted to the
Faculty of Graduate Studies and Research
in partial fulfillment of the requirements for the degree of
Master in Science

ABSTRACT

The relationship between the Arctic and sub-Arctic sea-ice concentration (SIC) anomalies, particularly those associated with the Greenland and Labrador Seas' "Ice and Salinity Anomalies (ISAs)" occurring during the 1960s/1970s, 1970s/1980s, and 1980s/1990s, and the overlying atmospheric circulation (SLP) fluctuations is investigated using the Empirical Orthogonal Function (EOF) and Singular Value Decomposition (SVD) analysis methods. The data used are monthly SIC and SLP anomalies, which cover the Northern Hemisphere north of 45^0 and extend over the 38-year period 1954–1991.

One goal of the thesis is to describe the spatial and temporal variability of SIC and atmospheric circulation on interannual and decadal timescales. Another goal is to investigate the nature and strength of the air-ice interactions. The air-ice interactions are investigated in detail in the first SVD mode of the coupled variability, which is characterized by decadal-to-interdecadal timescales. Similar decadal timescale signals of ice-cover fluctuations (and salinity fluctuations) are also found by Belkin et al (1998). Subsequently, the nature and strength of the air-ice interactions are studied in the second SVD mode, which shows a long-term trend. The interactions in the third SVD mode which has an interannual timescale are briefly mentioned. Evidence of significant air-ice interactions is revealed by a close resemblance between EOF_1 and the coupled SVD_1 of SLP and SIC.

To further understand these relationships, we present composite maps based on the time expansion coefficient of SVD_1 as well as SVD_2 of SIC. We also present spatial maps of temporal correlation coefficients between each of the first two leading SVD(SIC) expansion time coefficients and the atmospheric circulation anomalies at each grid. In the first and third SVD modes, the interactions between the atmosphere and sea ice are strongest with the atmosphere leading sea ice by 1 to 2 months. It is worth noting that in the second mode, the interactions are stronger with atmosphere lagging sea ice by 1 to 2 months than atmosphere leading sea ice by 1 to 2 months, although both magnitudes are similar. However, delayed interactions with SIC anomalies leading atmospheric fluctuations by up to several years are also evident

and are much more significant than the interactions with the atmosphere leading the sea ice by the same time period.

Résumé

On étudie la relation entre les anomalies de concentrations de glace de mer dans l'Arctique et le sub-Arctique, en particulier les "Anomalies de glace et de salinité" dans la Mer de Groenland et du Labrador, qui ont eu lieu en 1960/1970, 1970/1980 et 1980/1990, et les anomalies dans la circulation atmosphérique. A cet effet, on utilise les méthodes d'analyse de données de Fonctions Empiriques Orthogonales (EOF) et Decomposition en Valeurs Singuliers (SVD). Les données analysées sont des anomalies mensuelles de concentrations de glace de mer (SIC) et pression atmosphérique au niveau de la mer (SLP) sur l'Hemisphère Nord au nord de 45°, couvrant la période de 38 ans de 1954 à 1991.

Un des objectifs de cette thèse est de décrire la variabilité temporelle et spatiale de la concentration de glace de mer et de la circulation atmosphérique aux échelles de temps interannuelles et interdécennales. Un deuxième objectif est d'analyser la nature et l'intensité des interactions entre la glace de mer et l'atmosphère. Ces interactions sont analysées en détails dans le premier mode SVD, qui est characterisé par des échelles de temps décennales à interdécennales. Belkin et al. (1998) ont aussi observé des signaux d'étendue de glace et de salinité à des échelles de temps similaires. La nature et l'intensité des interactions entre la glace et l'atmosphère sont aussi étudiées dans le deuxième mode SVD, qui montre une tendence décroissante. On décrit brièvement les interactions dans le troisième mode, qui est dominé par des échelles de temps interannuelles. La forte ressemblance entre EOF1 et SVD1 des deux variables suggère que les interactions entre la glace de mer et l'atmosphère sont significatives.

Pour comprendre ces relations plus en profondeur, on présente les cartes des patrons de variabilité associées aux valeurs extrêmes des séries temporelles du SVD1 et SVD2 de la glace de mer. On présente aussi des cartes de correlations spatiales entre

les séries temporelles de chacun des deux premiers SVD(SIC) et les anomalies dans la circulation atmosphèrique à chaque point de grille. Dans le premier et troisième mode SVD, les interactions entre la glace de mer et l'atmosphère sont plus intenses quand l'atmosphère précède la glace d'un ou deux mois. Dans le deuxième mode, les interactions sont plus intenses quand la glace précède l'atmosphère d'un ou deux mois que quand l'atmosphère précède la glace d'un ou deux mois, bien que leurs magnitudes soient semblables. Par contre, on observe l'existence des interactions à long terme quand la glace précède l'atmosphère de plusieurs années. Ces interactions sont plus significatives que celles qu'on observe quand l'atmosphère précède la glace du même nombre d'années.

ACKNOWLEDGMENTS

I would like to express my thanks to my supervisor, Professor Lawrence A. Mysak, for his guidance throughout this work. His constant encouragement and invaluable discussions made my study at McGill an enjoyable experience. I am also deeply indebted to him for his patience with my writing.

I am very grateful to Miss Silvia Venegas for her many helpful discussions and assistance throughout this work, and for her proof-reading the thesis and translating the abstract into French. Besides, she generously offered the Global Sea-Ice and Sea-Surface Temperature data set (GISST2.2), the global monthly SLP data set, GMSLP2.lf, and the program for calculating the power spectrum of a time series. The GISST2.2 was kindly supplied to her by Robert Hackett, and the GMSLP2.lf by Tracy Basnett, both of whom are from the Hadley Centre for Climate Prediction and Research, UK. The program for calculating the power spectrum was supplied by Dr. Michael Mann. I am indebted to Drs. Robert Hackett, Tracy Basnett and Michael Mann for making these materials available and permitting me to use them.

I would like to express my gratitude to Dr. Halldor Bjornsson and Mr. Alan Schwartz for help in solving many computer problems; to Dr. Hai Lin for the assistance with NCAR Graphics; to Mr. Will Cheng for linguistic advice; and to Mr. Rick Danielson for solving the NCAR Graphics shading problem.

During the course of this work, I was supported by NSERC and AES grants awarded to Prof. L.A. Mysak, and also by an award from the C^2GCR FCAR Centre grant.

Last, but not least, I would like to thank my husband, Linghua Kong, and my parents for their patience, understanding and support.

Contents

List of Figures

List of Tables

Chapter 1

Introduction

The large-scale interactions between the sea-ice concentration (SIC) in the Arctic and the overlying atmospheric circulation have long been the subject of considerable interest and, more recently, the focus of a number of data and modeling studies (e.g., Walsh and Johnson, 1979b; Mysak and Manak, 1989; Walsh and Chapman, 1990; Mysak et al., 1990; Chapman and Walsh, 1992; Fang and Wallace, 1994; Slonosky et al., 1997; Tremblay and Mysak, 1997). These investigations have been prompted in the past by the fact that the thermal gradients at the ice-ocean boundary are among the largest on the surface of the earth during the non-summer months (Walsh and Johnson, 1979b). Since the nature of high-latitude atmospheric circulation depends on the distribution of the diabetic heating at ice margins, we might expect that the interannual and decadal scale fluctuations of SIC would contribute to the atmospheric variability on these timescales. At the same time, the atmospheric forcing also causes variability of SIC through thermodynamical and dynamical processes. Therefore, a quantitative understanding of ice-atmosphere interactions is complicated by feedback processes between these two components of the atmosphere-ice-ocean system.

On longer timescales, model experiments and qualitative arguments suggest that the SIC may play a major role in climate change issues, especially with regard to the rising CO_2 concentration in the atmosphere (Walsh, 1983). This is based on one or more of the physical properties of sea ice (Walsh, 1983). The formation of sea ice

increases the surface albedo from about 0.13 over open water to about 0.5 in the case of snow-free ice and to about 0.75 in the case of snow-covered ice (Pounder, 1965). Thus, due to the ice-albedo positive feedback mechanism, enhanced high-latitude warming caused by rising CO_2 could result in a decrease in SIC in the Arctic (e.g., Manabe and Stouffer, 1994).

Sea ice is important for climate in other ways as well. For example, the low thermal conductivity of sea ice results in an effective reduction of the vertical fluxes of sensible and latent heat at the surface, thereby insulating the ocean from the atmosphere and reducing the formation of clouds in the lower atmosphere (Power and Mysak, 1992). Secondly, because of the latent heat associated with melting and freezing, sea ice acts as a thermal reservoir which delays the seasonal temperature cycle (Walsh, 1983). Finally, sea ice alters the ocean salinity distribution and hence the ocean density stratification, both vertically by the expulsion of brine during the water freezing process and horizontally by the large-scale transport of low-salinity ice. More specifically, as the stratification in the Greenland Sea, Iceland Sea, Norwegian Sea, Baffin Bay and Labrador Sea is relatively weak and the density of sea-water is almost entirely salinity-controlled at temperatures close to the freezing point (Bryan, 1986), the density variability caused by the melting and formation of sea ice has a direct affect on Deep Water Formation in the North Atlantic and hence in the global thermohaline circulation. This is due to the fact that the thermohaline circulation is density-driven, and that both the rejection of salinity when water freezes and the freshening of the ocean when ice melts contribute to salinity anomalies there.

1.1 The low frequency signal in sea-ice concentration (SIC)

During the past two decades numerous observational and statistical studies have been carried out to describe the interannual and interdecadal variability of Arctic SIC (e.g. Walsh and Johnson, 1979a; Manak and Mysak, 1987; Mysak and Manak,

1989; Mysak et al., 1990; Agnew, 1993; and Slonosky et al., 1997). One of the most persistent and extreme variations in ocean climate observed in this century that is related to decadal-scale SIC change is the so-called "Great Salinity Anomaly"(GSA) in the northern North Atlantic Ocean (Dickson *et al.*, 1988). The anomaly consisted of a cool, relatively fresh water mass that was first observed north of Iceland during the late 1960s and was then traced cyclonically around the sub-polar Gyre during 1968–1982.

It eventually returned, although in a weakened state, close to the area of its origin in the Greenland Sea 13 or 14 years after its first appearance. It was found that accompanying the GSA were large positive anomalies of SIC in the Greenland Sea and then in the Labrador Sea (Malmberg, 1969: Mysak and Manak, 1989; Mysak et al., 1990). Mysak and Manak (1989) have illustrated the advective propagation of the SIC anomaly, in phase with the salinity anomaly, from the Greenland Sea in 1968–1969 to the Labrador Sea in 1971–1972. Mysak et al. (1990) showed that the timescale of propagation of the SIC anomaly from the Greenland Sea to the Labrador Sea is about 3–4 years. Further details of the GSA can be found in Slonosky et al. (1997). Due to this anomalous ice cover accompanying the GSA, such an ocean climate freshening event was also referred to as the "Great Ice and Salinity Anomaly" or GISA (Mysak and Power, 1992). However, because recurring ice and salinity anomalies were observed in the Greenland and/or Labrador Sea in the late 1970s/early 1980s and late 1980s/early 1990s (Belkin *et al.*, 1998), Mysak (1998) suggested that the collection of all such anomalies be called "ISAs", which is short for "Ice and Salinity Anomalies".

Observations and models have shown that the 1960s/70s GISA is not likely to be unique although its magnitude, perhaps, was exceptional. When additional repeat observations along standard sections and at standard stations allowed time series to be extended into the 1990s, another large temperature-ice-salinity-anomaly become evident (Belkin et al., 1997) in the late 1970s and early 1980s (the "1970s/80s ISA"). The 1970s/80s ISA may have started in the Greenland-Iceland Sea around 1979–80

and propagated around the North Atlantic in a similar fashion to that of 1960s/70s GISA but more quickly (Belkin *et al.*, 1998). This second anomaly was successively observed in the West Greenland Current (1982), the Labrador Current (1983), the Flemish Pass (1984), near the Charlie Gibbs Fracture Zone (1984–85), in the Rockall Channel (1985), south of Iceland (1985–88), in the North Sea (1986–87), Norwegian Sea (1987–1988), Barents Sea (1988–89) and Iceland Sea (1989–90). Thus the advection speed of the 1970s/80s ISA seems to be greater than that for the 1960s/70s GISA: the 1970s/80s anomaly reached the Barents Sea 6–7 years after peaking in the West Greenland Current, while the 1960s/70s anomaly traveled the same route in 8 to 10 years. However, there is still debate over the location of the very first signature of the 1970s/80s ISA; that is, "did it actually appear first in the late 1970s in North Icelandic waters and was then advected to the west Greenland Current as happened for the 1960s/70s GISA (Malmberg and Kristmannsson, 1992; Malmberg and Blindheim, 1993; Malmberg et al., 1994 and 1996) or was it first locally formed at the Fylla Bank, off the west coast of Greenland (Belkin *et al.*, 1998)" ?

Recent results from an analysis of the most complete data base compiled by Yashayaev (1995) for the Labrador Sea and Newfoundland Basin show *three* distinct low-salinity anomalies in these regions during the past *three* decades, all of which were associated with low-temperature anomalies in the early 1970s, 1980s, and 1990s. Deser and Timlin (1996) also found *three* positive SIC anomalies east of Newfoundland in the early 1970s, 1980s, and 1990s which resulted in low-temperature anomalies in the sub-polar North Atlantic one-to-two years latter (Fig. 1). The 1980s/90s ISA is also evident in the most recent data from the inshore Labrador Current (see Figures 22–23 in Drinkwater, 1994), and elsewhere on the Newfoundland Shelf (Colborune et al., 1997).

1.2 The possible interactions between sea ice and the overlying atmospheric circulation

It is widely believed that patterns (area and thickness) of SIC are determined by atmospheric wind forcing, because sea ice drift and upper ocean currents are mainly wind driven. Thorndike and Colony (1982), for example, show that large fractions ($\geq$ 80%) of the variance of sea ice drift in the central Arctic can be explained by the sea-level-pressure (SLP) field. Dickson et al. (1988) used the anomalous atmospheric circulation to explain the origin of the 1960s/70s GISA. They argued that an intense, persistent high pressure anomaly cell was established over Greenland in the 1960s (as documented by Dickson et al., 1975), resulting in abnormally strong northerly winds over the Greenland Sea that brought an increased amount of cold, fresh, polar water and exceptional sea ice outflow to the Iceland Seas. Fang and Wallace (1994) through a singular value decomposition (SVD) analysis of weekly Arctic sea ice and atmospheric circulation data, found that at short timescales the atmosphere drives the sea ice through the effects of pressure gradients and surface winds directing the motion of sea ice drift. Using the recently developed sea ice model of Tremblay and Mysak (1997), Tremblay and Mysak (1998) found that anomalous wind patterns in the western Arctic are the principal cause of sea ice interannual variability in the Beaufort-Chukchi Seas, while anomalous atmospheric temperature plays an important role on longer timescale fluctuations (longer than two years) of sea ice. It seems that fluctuations of fresh water input into Arctic are not important in creating large interannual variations in SIC (Tremblay and Mysak, 1998), contrary to what had been earlier hypothesized (Mysak *et al.*, 1990).

The variability of SIC, on the other hand, can influence the atmospheric circulation mainly through its effect on air-sea heat exchange, moisture exchange and momentum exchange. Herman and Johnson (1978), using an atmospheric general circulation model (GCM) to study the response of a model atmosphere to prescribed extremes of Arctic SIC, found that a general advance of the ice edge by $\sim$1000 km (corresponding

to two times the size of 1960s/70s GISA) would have a significant impact on the atmosphere over large portions of the Northern Hemisphere, increasing SLP up to 8mb, 700-mb geopotential height up to 100 gpm, and tropospheric temperature up to 8^0C at low levels. When investigating the influence of Sea of Okhotsk ice cover variations on large-scale atmospheric circulation by using a GCM, Honda et al., (1996) found significant differences in the model responses between heavy and light ice cover, not only around the Sea of Okhotsk but also downstream towards North America in the form of a stationary wave-train in the troposphere. The model results also indicate that a cold anticyclone is likely to develop over the Sea of Okhotsk in the heavy ice case.

Glowienka-Hense and Hense (1992), using an ECMWF T21 GCM model to investigate the response of the model to the absence of large area sea ice over the Kara Sea (a polynya), found the sensible and latent heat fluxes increased above the polynya, resulting in a warming of the lower troposphere above and near the polynya. But no statistically significant local or global SLP changes are associated with this heating. Later, Glowienka-Hense and Hense (1995) used a GCM to simulate the atmosphere response to a large polynya (1000 x 300 km) in the Weddell Sea, similar to that observed there in the 1970s. They found that the response of the atmosphere to this large polynya in the Antarctic is much stronger than the response to a polynya in the Arctic. The lower layer of the atmosphere above the polynya is warmed and the upper layer is cooled (the cooling of the upper levels extends to the surface further north to the equator). The pole-to-equator geopotential gradient is diminished. The Hense et al. results suggest that the response of the atmosphere to SIC anomalies is regionally dependent.

Having noticed that several large ice cover anomalies in the Greenland Sea (i.e., those observed during 1902–1920, during the late 1940s and the greatest one during the late 1960s and early 1970s, the 1960s/70s GISA) occurred 2–3 years after large runoffs from northern Canada into the western Arctic Ocean, Mysak et al. (1990) hypothesized a negative feedback loop connecting the ice anomalies in the Green-

land Sea with the anomalous river runoff from North America into the Arctic Basin. Later Mysak and Power (1992) simplified the previous ten-component feedback loop to a 6-component one: anomalously heavier sea-ice conditions in the western Arctic Ocean, which resulted from high amounts of precipitation and runoff in northern Canada, would advect to the Greenland and Iceland Seas 3–4 years later, causing reduced upper-layer salinity in the Iceland Sea when the ice melted. The freshening would reduce the convective overturning in the Iceland Sea during winter, cause reduced cyclogenesis over Iceland Sea and Irminger Basin, and then result in reduced precipitation and runoff in northern Canada, which closes the feedback loop. This self-sustained climatic oscillation has a period of about 15–20 years. Based on this feedback loop, Mysak et al. (1990) predicted that another large positive sea ice concentration (SIC) anomaly in the Greenland sea would have occurred in the late 1980s. This prediction was partly substantiated by later sea-ice measurements (Mysak and Power, 1991; 1992). Mysak and Power (1991) also found a high correlation between the runoff from North America into the Arctic Basin and the Koch Ice Index. However, Agnew (1993) shows only a moderate positive SIC anomaly of 8.4×10^4 km^2 existed in the Greenland Sea in 1988.

In a 1996 McGill M.Sc. thesis by Victoria Slonosky (1996) (also published as Slonosky et al., 1997), the relationship between Arctic sea ice concentration anomalies and atmospheric circulation anomalies was investigated using an Empirical Orthogonal Function (EOF) analysis and by constructing anomaly maps. Slonosky et al. described the spatial and temporal variability of winter and summer SLP, 850-hPa T, 500-hPa Z, and SIC by presenting the 4-year anomaly maps and their evolutions. The EOF analysis compressed the many scales of variability associated with the data into mode form and only the most important mode, EOF1, for all the atmospheric climate variables and SIC were further investigated. From the EOF1 of winter SIC, she found the existence of a dipole structure of SIC anomaly between the Barents Sea, Norwegian Sea, Greenland Sea areas with one sign and Baffin Bay, Labrador Sea and east of Newfoundland areas with an opposite sign; this see-saw variability

has a decadal period. While some interesting interaction processes were uncovered in Slonosky' study, it is believed that the full extent of these interactions will only be revealed by an Singular Value Decomposition (SVD) analysis, which is designed to extract the maximum *covariability* between two sets of climate variables (Bretherton *et al.*, 1992). In this thesis, the SVD method will be used to explore this variability. Besides the application of a different method, the present study involves an extension in the time domain in that all the monthly data are used instead of winter or summer season data only, as used in Slonosky et al. (1997). Another important factor motivating this research is that now there is new evidence which suggests the existence of a 1970s/80s ISA and a 1980s/90s ISA. At the time of Slonosky's (1996) study, only the existence of the 1960s/70s GISA was confirmed. In this thesis, the second and third modes of the coupled atmosphere and SIC will also be presented. These have a strong signal in SIC over the Pacific sector, in contrast to the case of the first SVD mode.

The SVD method was successfully applied by Venegas et al. (1996, 1997) to study the relationship between monthly SST and SLP anomalies in the South Atlantic. As mentioned above, Fang and Wallace (1994) also used the SVD method to investigate the relationship between weekly SIC anomalies and the overlying atmospheric circulation for the relatively short record 1972–1989; in particular they examined the Pacific and Atlantic sectors separately. The present study is in some ways an extension of the work by Fang and Wallace to include a more general space-time framework, and to use a longer data base (38 years). All the regions north of 45^0N are considered and the Atlantic, Pacific and Arctic sectors are studied simultaneously, unlike in Fang and Wallace. A monthly sea-ice data set, ranging from 1954 to 1991 with a spatial resolution of 5 degrees in longitude and 5 degrees in latitude is used. Also in this study, we include SLP and geostrophic winds calculated from the SLP. The choice of SLP and geostrophic winds to represent the atmospheric circulation is motivated by previous results which demonstrate that the ice motion is mainly wind driven. However, this decision puts more weight on the role of atmospheric forcing, and less weight on the

atmospheric response to sea ice. As mentioned earlier with regard to the Glowienka-Hense and Hense (1992) study, the warming of the lower troposphere above and near the Kara Sea polynya is significant; however, the SLP showed no significant change. Fang and Wallace (1994) found that the correlation between SVD_1(SIC) and 1000-500-hPa thickness is stronger than the correlations between SVD_1(SIC) and SLP and 500-hPa Z, although the correlations are quite comparable.

The main goal of this thesis is to get a deeper understanding of the relationship between SIC anomalies and the atmospheric circulation anomalies on interannual to interdecadal time-scales by using the SVD method over the entire Arctic region. Emphasis is placed on explaining the observed large-scale variability of the high-latitude ice-atmosphere system and the interregional relationship of this variability, which has received little attention in the earlier studies.

The structure of this thesis is as follows. The data used in this study are described in Chapter 2, where the climatology of SIC and SLP together with the geostrophic wind are also presented. In Chapter 3, the methods used are introduced. EOF results are presented in chapter 4. Chapter 5 mainly describes the interactions between SIC and atmospheric circulation in separate mode form, i.e., SVD_1, SVD_2, SVD_3. A brief summary is given in Chapter 6.

Chapter 2

The data and their preparation for analysis

2.1 The SIC data and preparation

The monthly SIC data used are derived from the Global Sea-Ice and Sea-Surface Temperature data set (GISST2.2), which was provided by Robert Hackett from the Hadley Centre for Climate Prediction and Research, UK. The majority of the sea-ice data before 1990 are also contained in Walsh (1994). Ice cover maps (see below) are available from Jan. 1903 to Dec. 1994. The data set contains monthly values representing the coverage at the middle of a given month on each 1^0 latitude x 1^0 longitude grid box. Each grid box has a different area, which decreases poleward. SIC is defined as the fraction of a grid area covered by ice. Concentration values are reported in tenths, ranging from 0/10 (no sea ice was reported in the grid area at the particular month) to 10/10 (the grid area was completely covered by ice at that month).

A fairly long record is necessary to identify fluctuations of up to interdecadal timescales (if any such fluctuations exist). However, imprecise cover classifications, the variety of observational techniques used, and missing data contribute to some non-uniformity in the earlier data, especially those during the world war periods.

Thus, the data before 1954 are discarded as their reliability is questionable and their inclusion produced irregularities in the early stages of the data analysis. The data officially ends at Dec. 1994; however, due to the inconsistent format of the data after Nov. 1992, the actual data used in this thesis extend from January 1954 to December 1991, a 38-year period. Spatially, the data covers the northern Hemisphere, north of 45^0N.

The first step of the data preparation is to extract the oceanic grid values north of 45^0N for the period Jan. 1954–Dec. 1991 from the GISST2.2 SIC data set. The GISST2.2 data set is a global data set, with land grids assigned with special flags. It was found that the total number of land grids changed from month to month. As the total number of land grids and the total number of ocean grids cannot change with time, we believe this inconsistency may be due to mistaking some coastal land ice for sea ice. Accordingly this inconsistency is removed by discarding every ocean-like ice-covered grid if at any time this grid was once assigned with a land flag. It was found that the results are not sensitive to the presence of continent grids in the SIC data set provided these grids are assigned with zero values. Afterwards the area weighting of SIC at each grid is performed by multiplying the concentration value by the square root of the cosine of latitude, as suggested by North et al. (1982). The reason for doing this is to reduce the effect caused by different grid box area size.

The second step of the data preparation is to obtain the monthly anomalies. The climatological monthly means are calculated for the whole 38-year period Jan. 1954–Dec. 1991, which contains 456 months in total. These mean values are then subtracted from the original time series of SIC at each 1^0 latitude x 1^0 longitude grid point to form the monthly anomalies. In order to reduce the noise inherent in the monthly anomalies, the time series at each grid are then smoothed by performing a three-month-running mean. The first month (Jan. 1954) and the last month (Dec. 1991) of the data are only two month running means.

To save storage of space and to focus on large spatial scales (Slonosky et al., 1997), the data with a 1^0 by 1^0 latitude/longitude grid fine resolution were then uniformly

averaged to a coarser 5^0 by 5^0 latitude/longitude data set. After these three steps, the resulting data for SIC consists of: three-month-running mean monthly anomaly data for period Jan. 1954–Dec. 1991, for all the oceanic grids north of 45^0N with 5^0 by 5^0 latitude/longitude resolution. This anomaly SIC data set together with the corresponding SLP monthly anomaly data (see below) were then used to perform the EOF and SVD analyses.

2.2 The atmospheric data and preparation

The SLP data used were supplied by Tracy Basnett from the Hadley Centre for Climate Prediction and Research, UK. This data set is called the GMSLP2.lf data set, archived on a 5^0 by 5^0 latitude/longitude grid, covering the latitudes 90^0N to 90^0S and the longitudes 180^0W to 175^0E. The GMSLP2.lf data set is a monthly data set, giving the SLP values (in hPa) for each grid at the middle of a given month, from January 1871 to December 1994. To be consistent with the SIC data set as required by the SVD method, the period used for the SLP field is from Jan. 1954 to Dec. 1991, which is the same period as used for the SIC field. The procedure used to prepare the SLP anomaly data is exactly the same as that used to prepare the SIC data set except there is no need to remove the land grids from the SLP data nor is it necessary to extrapolate the SLP data onto a coarser grid.

The monthly mean geostrophic wind component (u,v) are calculated from the SLP data set, using the following formulas:

$$u = \frac{-1}{f\rho}\frac{\partial p}{\partial y}, \tag{2.1}$$

$$v = \frac{1}{f\rho}\frac{\partial p}{\partial x}, \tag{2.2}$$

where p is the SLP, u and v are the meridional and longitude components of the wind, ρ is the air density, f is the Coriolis constant. After the monthly geostrophic wind field is obtained, the same procedure as applied in the SIC and the SLP cases is used to calculate the climatology and the monthly anomalies of the geostrophic

wind. The monthly geostrophic wind stress is estimated by rotating the monthly geostrophic wind to its left by 20^0 (J. Walsh, private communication; also see Tremblay and Mysak, 1997). This is an empirical approximation. Using this approach, the geostrophic wind stress anomalies are under-estimated, as the geostrophic wind stress is not linearly related to the wind and SLP. The more accurate way (Tremblay and Mysak, 1998) to obtain the geostrophic wind stress is to use the daily SLP data to calculate the daily geostrophic wind and then the geostrophic wind stress (quadratically related to the wind). One then averages the daily wind stress values to obtain the monthly wind stress values and hence the monthly anomalies.

2.3 The annual cycle inherent in the data

The SVD expansion time coefficients of SIC as well as their power-spectra, show annual peaks even though the annual cycle has been supposedly removed from the anomaly data by subtracting the climatology of each calendar month from the original monthly data. The annual peaks in the anomaly time series might result from the strong annual cycle and the relatively narrow range of SIC values, from 0 to 10. These annual peaks were also noticed by Tang et al. (1994). To eliminate the annual cycle in the SIC anomaly data, several methods, which can be categorized into two groups, were tried separately. In one group, one uses the annual data instead of the monthly data. In this group, three kinds of data sets are prepared based on the 3-month-running mean monthly anomaly data, i.e, the long-winter season data, the short-winter season data and the spring season data. The long-winter season data are the time averages of 6-month values from November of the previous year($i-1$ th year) to April of the present year(i th year). This average is then assigned to the year the winter ends, the "i th year". The short-winter season data are the average values of only three winter months, from December of the previous year through to February of the present year and the value is assigned to the year the winter ends, "the present year"; the spring data set is the three month average of : April, May

and June, and this average is regarded as the annual value of the corresponding year.

The other group of methods for removing the annual cycle are the filtering methods. Two methods in this group were tried, one is the standard Fourier Transform (FT), the other is the Kolmogorov-Zurbenko (KZ) filter. The Fourier Transform method first translates the recorded data from a time domain into a frequency domain, and then eliminates the higher than one cycle per year frequency oscillation. Next, one sums up only the oscillations with frequencies lower than the cut off value. Finally, one translates the filtered data from the frequency domain back to the original time domain.

The KZ filter is based on an iterative moving average that removes high-frequency variations from the data. The moving average is computed by the formula

$$y_i = \frac{1}{2q+1} \sum_{j=-q}^{q} x_{i+j}, \tag{2.3}$$

where $2q+1$ is the length of the filter window, and y_i becomes the input for the second pass, and so on. By modifying the window length and the number of iterations, the filtering of different scales of motion can be controlled. To filter all periods of less than P days, the following criterion is used:

$$D \times N^{1/2} \leq P, \tag{2.4}$$

where D ($D = 2q + 1$) is the window size in days and N is the number of iterations. A more detailed description of how one chooses the parameters P and N is provided by S. Rao et al. (1997, manuscript submitted to *Bull. Amer. Meteor. Soc.*). For the present case, N is chosen to be 5 and D is 7 months.

The primary statistics (i.e., squared covariance fraction (SCF) for SVD, covariance fraction (CF) for EOF) of the SVD and EOF results for each prepared anomaly data set are shown in Table 2.1. By comparing the results for each data set, it is found that no method is perfect to eliminate the residual annual cycle. Each method has some advantages and also has some shortcomings. The Fourier Transform (FT) method completely removes the higher than one cycle per year frequency oscillations, resulting in high SCF for the SVD results and high CF for the EOF results.

data-type	SCFs for SVDs			CF for EOF (SIC)			CF for EOF (SLP)		
	SVD_1	SVD_2	SVD_3	EOF_i1	EOF_i2	EOF_i3	EOF_p1	EOF_p2	EOF_p3
long-winter	59.95	17.45	7.79	23.15	14.6	13.77	36.82	19.25	9.7
short-winter	60.3	20.43	6.68	22.09	19.73	12.45	37.09	18.04	8.83
spring	28.02	23.34	14.69	22.65	13.04	11.03	23.5	13.8	10.07
anomaly	53.75	15.77	7.4	13.54	7.52	6.9	27.77	12.73	11.71
KZ-filter	59.77	16.78	6.63	15.78	9.38	8.2	33.06	13.9	9.85
Fourier filter	73.51	10.23	4.3	16.28	9.37	8.02	59.32	9.31	8.06

Table 2.1: Comparison of the statistics (i.e., SCF for SVD, CF for EOF) of the leading SVDs and EOFs of data prepared with different filtering methods.

However, the spatial variability of SVD_1(SLP) is reduced too much and seems to be suspicious. The data set prepared by the Fourier Transform method may not represent well the original data, especially for the SLP case; the variance associated with the data after the FT filter may be only a very small part of the original data and may not be significant. So the FT method was discarded. The results of the KZ filtered data are even worse. The moving average and the iteration smoothed the data so much that there is no significant lag-correlation between the SVD1(ice) expansion time coefficient and the SLP anomaly time series at each grid. The spring data set is discarded because the first mode of SVD explains too little SCF. This is consistent with Slonosky et al. (1997) who found that most of the variance for SIC and atmospheric fluctuations are concentrated in the winter season. The results of the long-winter and short-winter data set are similar. However, as no power spectrum of the SVD expansion coefficient time series for the short-winter data set pass the 95% significance level, the short-winter method was discarded. For the long-winter data set, the lag-correlation between the time series of the SVD and EOF and the SLP grid value are not significant except for the zero-lag case, so this method was not adopted either.

Thus the final data used is the monthly anomaly 3-month smoothed data set, prepared in the way as discussed in section 2.1 and 2.2 even though there exist some residual annual peaks in those data. In a related study (Venegas, 1997, private communication), Venegas found that the main results are not affected by the annual peaks.

2.4 The climatology of SLP, geostrophic winds and SIC

All the results in chapters 4 and 5 will be presented in the form of anomalies. To set the background, the climatological fields for SLP, geostrophic wind vector, and SIC are presented in Fig. 2. The climatologies are the annual mean from 1954 to 1991, and these represent a 38-year average.

From the climatology of SLP, one can see three main climatological centres: the Aleutian Low, the Siberian High, and the Icelandic Low. The relatively small Arctic high cell in the vicinity of 75^0–80^0N, 150^0–170^0W produces the winds that drive the "Beaufort Gyre" circulation in the western Arctic. The variability of this high can cause noticeable changes in the ice motion in this region. The geostrophic component of wind associated with the generally decreasing pressure across the pole towards the European sub-Arctic (the Norwegian Sea, Barents Sea and Kara Sea), where the cyclonic systems frequently move from the North Atlantic into the Arctic (Serreze and Barry, 1988), drive the sea ice motion from the Asian coastal waters towards Fram Strait and the Greenland-Iceland Seas. This movement of sea ice as well as the fresh surface Arctic sea water is called the "Transpolar Drift Stream (TDS)" (cf. Serreze et al., 1989, , Fig.1). Most of the Arctic sea ice and fresh water export to the North Atlantic Ocean is caused by this TDS. There is far less Arctic sea ice and fresh water output through the Canadian Arctic Archipelago (CAA) into Baffin Bay, and virtually none of these reaches the North Atlantic.

The climatology of ice-edge (sea-ice extent) is confined to a narrow zone of about

5—10^0 of latitude, the so-called transition zone. Poleward of this transition zone, the Arctic Ocean is completely ice covered; equatorward of this zone, the surface of the earth is, on average, ice free. It is found that most of the temporal variability of SIC tends to be confined within this transition zone.

Chapter 3

The Singular Value Decomposition (SVD) Method

Although the EOF method is used in this thesis, it is not described here, as it is now a well known method (e.g., Peixoto and Oort, 1992). The interested reader can also consult Slonosky (1996) or Bjornsson and Venegas (1997) for a detailed discussion of the EOF method.

3.1 Introduction to the SVD

Singular Value Decomposition (SVD) is a fundamental matrix operation that can be thought of as an extension to rectangular matrices of the diagonalization of a square symmetric matrix. The SVD method is mainly applied to two (geophysically) coupled fields. For example, in the present case, the SIC field is denoted as the $\boldsymbol{s}$ field and the SLP field is denoted as the $\boldsymbol{p}$ field. Its main purpose is to extract from the cross-covariance matrix between the two coupled fields, pairs of spatial patterns that explain as much as possible of the mean-squared temporal covariance between these two fields. One spatial pattern multiplied by one expansion time coefficient for each field defines a SVD mode. The modes are ordered according to the fraction of squared covariance they explain. The first mode explains the maximum amount of

squared covariance (SC) of the two fields, the second mode explains the maximum amount of squared covariance of the two fields that was unexplained by the previous mode, and so on. For each mode the correlation coefficient, r, between the expansion time coefficients of each field is used to describe the strength of the coupling between the two fields identified by the particular mode.

3.2 The properties of the SVD

Some important properties (Strang, 1988) of the SVD method are summarized below, in a notation that applies to the data sets used in this thesis.

(1) Any m_s x m_p matrix R can be decomposed uniquely as follows:

$$R = \sum_{k=1}^{N} \sigma_k \boldsymbol{l}_k \boldsymbol{r}_k^T, \qquad N \leq (m_s, m_p), \tag{3.1}$$

where the $\boldsymbol{l}_k$ are an orthonormal set of N vectors of length m_s, called the *left singular vectors*: $\boldsymbol{r}_k$ are an orthonormal set of N vectors of length m_p, called the *right singular vectors*: the σ_k are positive numbers, called the *singular values*, ordered such that $\sigma_1 \geq \sigma_2 \geq \cdots \geq \sigma_N$, and N is the rank of R.

(2) $R^T \boldsymbol{l}_k = \sigma_k \boldsymbol{r}_k, R\boldsymbol{r}_k = \sigma_k \boldsymbol{l}_k$.

(3) The σ_k^2, k=1,2,$\cdots$,N, are the N nonzero eigenvalues of $R^T R$ and RR^T. The remaining eigenvalues of these two matrices are zero.

(4) The $\boldsymbol{l}_k$ are the eigenvectors of RR^T with non-zero eigenvalues, σ_k^2, and the $\boldsymbol{r}_k$ are the eigenvectors of $R^T R$ with the same nonzero eigenvalues, σ_k^2.

(5) For a square symmetric matrix, the left and right singular vectors are both equal to the eigenvectors, and the singular values σ_k^2 are the absolute values of the corresponding eigenvalues.

(6) The square of the Frobenius matrix norm of R is the sum of the squares of its singular values:

$$\| C \|_F^2 = \sum_{k=1}^{N} \sigma_k^2. \tag{3.2}$$

3.3 The SVD method applied to geophysical fields

As mentioned above, the SVD method was introduced into the geophysical sciences to study the covariability of two fields. For a comparison of the SVD method with some other methods, such as the EOF and the CCA (Canonical Correlation Analysis), see Bretherton et al., (1992) and Bjornsson and Venegas (1997).

Suppose there are measurements of one variable, for example in the present case, SIC denoted as the $\boldsymbol{s}$ field, at locations $x_1, x_2, \cdots, x_{m_s}$, taken at times t_1, t_2, $\cdots$, t_n. The expression $s_k(t_j)$ thus means the measurements made at location x_k at time t_j. Also, suppose there are measurements of another variable, say, SLP, denoted as the $\boldsymbol{p}$ field at locations $y_1, y_2, \cdots, y_{m_p}$, taken at times t'_1, t'_2, ... t'_n. Next, the SIC values are arranged in the following way:

$$\boldsymbol{S} = \begin{vmatrix} s_1(t_1) & s_2(t_1) & \cdots & s_{m_s}(t_1) \\ s_1(t_2) & s_2(t_2) & \cdots & s_{m_s}(t_2) \\ \cdots & \cdots & \cdots & \cdots \\ s_1(t_n) & s_2(t_n) & \cdots & s_{m_s}(t_n) \end{vmatrix}, \tag{3.3}$$

where the k-th column, $k = 1, 2, ...m_s$, represents the SIC observation time series at a particular location x_k, and the j-th row represents the map of the SIC configuration at a particular time t_j. Similarly, the other variable, $\boldsymbol{p}$, is also arranged in the form

$$\boldsymbol{P} = \begin{vmatrix} p_1(t'_1) & p_2(t'_1) & \cdots & p_{m_p}(t'_1) \\ p_1(t'_2) & p_2(t'_2) & \cdots & p_{m_p}(t'_2) \\ \cdots & \cdots & \cdots & \cdots \\ p_1(t'_n) & p_2(t'_n) & \cdots & p_{m_p}(t'_n) \end{vmatrix}, \tag{3.4}$$

where the k-th column represents the SLP observation times series at a particular location y_k, and the j-th row represents the SLP map at a particular time t'_j. The observation times t_j and t'_j of these two fields can be different (with some lag); however, the length of the observation time series, t_n, should be the same for these two fields. On the other hand, there is no constraint on the spatial domains for the two

fields. The SIC field can have less (or more) grid points than the SLP field.

Next, we will show the way in which singular value decomposition of the cross-covariance matrix between the two fields identifies pairs of patterns that explain as much as possible of the mean-squared temporal covariance between the two fields (see also Bretherton et al., 1992). From now on, the $\boldsymbol{s}$ field will be called the left field, and the $\boldsymbol{p}$ field will be called the right field, according to the convention in a SVD analysis.

Generally, the two time series (the spatial dependence, i.e., the dependence on grid points, is reflected by the **vector** forms of s and p), $\boldsymbol{s}$(t) and $\boldsymbol{p}$(t), can each be expanded in terms of a set of N vectors $\boldsymbol{u}_k$ and $\boldsymbol{v}_k$ respectively (it will be shown that N is the rank of the cross-covariance matrix between $\boldsymbol{s}$ and $\boldsymbol{p}$ field), called *patterns*, which are spatially dependent functions, via.,

$$\boldsymbol{s}\ (t) = \sum_{k=1}^{N} a_k(t)\boldsymbol{u}_k, \tag{3.5}$$

$$\boldsymbol{p}\ (t) = \sum_{k=1}^{N} b_k(t)\boldsymbol{v}_k. \tag{3.6}$$

The vectors $\boldsymbol{u}_k$ and $\boldsymbol{v}_k$ are called *weight vectors*. The time dependent factors, $a_k(t)$ and $b_k(t)$, are called expansion time coefficients and are calculated as weighted linear combinations of the grid point data:

$$a_k(t) = \sum_{i=1}^{m_s} u_{ik}s_i(t) = \boldsymbol{s}(t)\boldsymbol{u}, \tag{3.7}$$

$$b_k(t) = \sum_{j=1}^{m_p} v_{jk}p_j(t) = \boldsymbol{p}(t)\boldsymbol{v}. \tag{3.8}$$

Because the patterns are spatially orthonormal, the left expansion coefficients can be thought of as the projections of the vectors $\boldsymbol{s}$(t) on the left patterns, and similarly for the right field.

The "leading" patterns $\boldsymbol{u}_1$ and $\boldsymbol{v}_1$ are chosen as follows: the projection $a_1(t)$ of $\boldsymbol{s}$(t) on $\boldsymbol{u}_1$ has the maximum covariance with the projection $b_1(t)$ of $\boldsymbol{p}$(t) on $\boldsymbol{v}_1$. Successive pairs ($\boldsymbol{u}_k$, $\boldsymbol{v}_k$) are chosen in exactly the same way with the added condition that $\boldsymbol{u}_k$

is orthogonal to $\boldsymbol{u}_1, \cdots, \boldsymbol{u}_{k-1}$, and $\boldsymbol{v}_k$ is orthogonal to $\boldsymbol{v}_1, \cdots, \boldsymbol{v}_{k-1}$. The unknown spatially dependent patterns $\boldsymbol{u}_1$ and $\boldsymbol{v}_1$ can be expanded in the bases of the left and right singular vectors of the cross-covariance matrix R between fields **S** and **P**, viz.,

$$R = \mathbf{S}^{\mathbf{T}}\mathbf{P}. \tag{3.9}$$

Thus we have

$$\boldsymbol{u}_1 = \sum_{m=1}^{m_s} \mu_m \boldsymbol{l}_m, \tag{3.10}$$

$$\boldsymbol{v}_1 = \sum_{n=1}^{m_p} \eta_n \boldsymbol{r}_n, \tag{3.11}$$

where $\boldsymbol{l}_m$ is the left singular vector and $\boldsymbol{r}_n$ is the right singular vector of the cross-covariance matrix R between the left and right fields. Taking the inner product of Eqn. 3.10 with itself, using the orthonormality of the $\boldsymbol{l}$ and noting that $|\boldsymbol{u}_1| = 1$, we deduce that $|\boldsymbol{\mu}| = 1$. Similarly $|\boldsymbol{\eta}| = 1$.

Hence, the covariance of the projections $a_1(t)$ and $b_1(t)$ takes the form

$$\begin{aligned}
covariance\{a_1(t), b_1(t)\} &= covriance\{\boldsymbol{s}(t)\boldsymbol{u}_1, \boldsymbol{p}(t)\boldsymbol{v}_1\} \\
&= \boldsymbol{u}_1^T \boldsymbol{s}^T \boldsymbol{p} \boldsymbol{v}_1 \\
&= \sum_{m=1}^{m_s} \mu_m \boldsymbol{l}_m^T R \sum_{n=1}^{m_p} \eta_n \boldsymbol{r}_n \\
&= \sum_{m=1}^{m_s} \sum_{n=1}^{m_p} \sum_{k=1}^{N} \mu_m \eta_n \sigma_k \boldsymbol{l}_m^T \boldsymbol{l}_k \boldsymbol{r}_k^T \boldsymbol{r}_n \\
&= \sum_{k=1}^{N} \mu_k \eta_k \sigma_k \\
&\leq \sigma_1 |\sum_{k=1}^{N} \mu_k \eta_k| \\
&\leq \sigma_1 |\boldsymbol{\mu}||\boldsymbol{\eta}| \\
&= \sigma_1.
\end{aligned} \tag{3.12}$$

This relationship becomes an equality only when $\mu_1 = \eta_1 = 1$ and all other coefficients μ_p, η_p are zero, that is, when $\boldsymbol{u}_1 = \boldsymbol{l}_1$, $\boldsymbol{v}_1 = \boldsymbol{r}_1$. Hence, the unknown first spatial pattern for the left (right) field is just the first left (right) singular vector

of the cross-covariance matrix between the left and right field. The largest singular value σ_1 obtained through the SVD of the cross-covariance matrix between the two fields is just the maximum covariance of the two fields. The corresponding expansion coefficient can be obtained by projecting the left field $\boldsymbol{s}$(t) onto the first left singular vector and the right field $\boldsymbol{p}$(t) onto the first right singular vector. This means that the first SVD mode of the cross-covariance matrix maximizes the covariance between the left field and the right field, and also maximizes the squared covariance between the two fields. Because the square of the Frobenius matrix norm of R is the sum of the square of its singular values, the fraction of the squared covariance is used to order the modes, and not the fraction of the covariance itself.

Similarly, the subsequent pairs of patterns that explain the maximum amount of covariance that is unexplained by the previous modes of the two fields, subject to the constraint that they be orthogonal to the previous patterns, are the pairs of left and right singular vectors:

$$\boldsymbol{v}_k = \boldsymbol{l}_k, \qquad \boldsymbol{u}_k = \boldsymbol{r}_k. \tag{3.13}$$

It can be shown similarly that this choice can maximize the covariance between the expansion coefficients $a_k(t)$ and $b_k(t)$. The covariance is just the k-th singular value. The k-th expansion coefficients $a_k(t)$ or $b_k(t)$ can be obtained by projecting the left or right field on to the corresponding k-th left or right singular vector.

There are three basic quantities associated with each SVD mode: 1) the correlation time coefficient $r[a_k(t), b_k(t)]$ between the expansion coefficients of the left and right fields, obtained by correlating the expansion coefficients $a_k(t)$ and $b_k(t)$; 2) the squared covariance SC = ${\sigma_k}^2$, which is the square of the corresponding singular value σ_k; and 3) the fraction of squared covariance, SCF, or the percentage of the squared covariance explained by a pair of patterns, obtained by dividing the square of the singular value, ${\sigma_k}^2$, by the sum of the squares of all the singular values. From Eqn. 3.2 we find

$$SCF_k \equiv \frac{covariance\{a_k(t), b_k(t)\}^2}{\| R_{sp} \|_F^2} = \frac{\sigma_k^2}{\sum_{l=1}^{N} \sigma_l^2}. \tag{3.14}$$

Similarly, the cumulative squared covariance fraction (CSCF) of R explained by the leading m modes is

$$CSCF_r = \frac{\sum_{k=1}^{m} \sigma_k^2}{\sum_{k=1}^{N} \sigma_k^2}. \tag{3.15}$$

The correlation coefficient $r[a_k(t), b_k(t)]$ is a measure of the strength of the coupling between the left pattern and the right pattern inside a particular SVD mode. The SC gives the information of how much square covariance is explained by a particular mode. At the same time, the SCF informs the relative importance of a particular mode with respect to the other modes. The CSCF is a measure of which percentage of the covariance associated with the two fields is explained by the leading SVD modes. It can be shown (Stewart, 1973) that the SVD method is an "optimal" method in that it explains the maximum possible CSCF with the first several leading modes. The CSCF is an analog for a covariance matrix of the "cumulative variance fraction (CVF)" explained by the leading modes in EOF analysis. If the left and right fields $\boldsymbol{s}$ and $\boldsymbol{p}$ are identical, item 5 of section 3.2 implies that EOF and SVD will yield equivalent results with the square of the singular values σ_k^2 equal to the mode variances λ_k (the eigenvalues of the variance matrix) (Bretherton et al., 1992). Note that in this case, CSCF, as obtained from Eqn. 3.15, approaches unity more rapidly with the incorporation of additional modes than the cumulative variance fraction $CVF_N = \frac{\sum_{k=1}^{r} \lambda_k}{\sum_{k=1}^{N} \lambda_k}$, because the variances are *squared* in the CSCF, emphasizing the leading modes with larger mode variances. Thus, a large CSCF is less significant than a large CVF (Bretherton et al., 1992).

The statistical significance of the results can be assessed by comparing any of the above quantities: $r[a_k(t), b_k(t)]$, SC, SCF, CSCF, with the corresponding value derived from SVD analysis performed on the same fields with the temporal order of one of the fields scrambled.

3.4 The statistical significance for the squared covariance (SC)

So far, it is not clear whether the squared covariance, SC, and the correlation coefficient, $r_k[a_k(t),\ b_k(t)]$ of a particular mode are significant or not. There is not a formal significance test method known for the results of the SVD. The Monte Carlo method is widely used for the SC (Bjornsson and Venegas, 1997; Venegas et al., 1997; Peng and Fyfe, 1996; Wallace et al., 1992). This method will be used in this thesis for assessing the statistical significance of the SC. The significance of the temporal correlation is assessed by another method described by Sciremammano (1979).

3.4.1 The statistical test for the SC

In general, the number of spatial grid points for the left field and right field might be different. In order to remove the effect of the difference in the spatial size, the squared covariance SC= σ_k^2 is, in general, normalized by dividing the product of the spatial sizes of the $\boldsymbol{s}$ and $\boldsymbol{p}$ fields. The significance of the normalized SC can be assessed by comparing the SC of the original fields with the corresponding values derived from SVD analyses performed on the same fields with the temporal order of one of the fields scrambled. The field chosen to be scrambled should be the one with comparatively smaller month-to-month autocorrelation ("memory") of the two fields, in order to minimize the increase of degrees of freedom inherent in the scrambling procedure. In our case, the field chosen to be scrambled is the sea level pressure (SLP). The scrambling should be done on the years and not on the months. After scrambling, the 12 maps of SIC of a given year will be paired with the 12 maps of sea level pressure (SLP) of another randomly chosen year, but the order of the months inside the year is maintained. In such a way, we link the January map of a given year of the SIC with the map of January of another randomly chosen year of the SLP field; the map of February of the SIC field with the map of February of another randomly chosen year of SLP field, and so on. In this way we do not deteriorate the

intra-seasonal variability inherent in the coupling, which would lower the significance levels and make the results appear more significant than they really are. We then perform an SVD analysis on the new data sets with one of them being scrambled and the other being the original data set. The same procedure of scrambling one of the data sets and performing the SVD analysis is repeated 100 times, each time keeping the values of the total squared covariance (TSC) and SC of each mode. The SC value from the original data set will be statistically significant at the 95% level if it is not exceeded by more than five values of the corresponding SC obtained using the scrambled data sets. The same holds for the TSC.

3.4.2 Significance level for the correlation coefficient, $r_k[a_k(t), b_k(t)]$

The correlation coefficient itself means nothing if the interplay between the timescale of the fields and the length of the time series is not considered. Normally, only the correlation coefficient which passes its corresponding 95% significance level can have more real physical meaning concerning the strength of the coupling of the two fields.

The significance level of a temporal correlation varies according to the integral timescale as determined by the autocorrelation function, even when the nominal number of degrees of freedom (given by the length of the series) does not change. Therefore, although the SLP and SIC fields have the same duration of observations, the SLP field has more real degrees of freedom since it has a shorter timescale and thus its significance levels are lower than those of the SIC field. The SIC field has fewer real degrees of freedom due to the "longer memory" of sea ice.

The method for calculating the significance level we use has been suggested by Sciremammano (1979). This method takes into consideration the autocorrelation ('memory') inherent in the two series involved. The large-lag standard error σ between the two time series $X(t)$ and $Y(t)$ is computed as follows:

$$\sigma^2 = n^{-1} \sum_{i=-M}^{M} C_{xx}(it) C_{yy}(it), \tag{3.16}$$

where C_{xx} and C_{yy} are the autocorrelation functions of $X(t)$ and $Y(t)$ respectively, n is the length of both time series, and M is large compared with the lag number at which both C_{xx} and C_{yy} are statistically zero. Thus, to a good approximation, for time series involving at least 10 degrees of freedom, the 90%, 95% and 99% significance levels are equivalent to: C_{90}=1.7*σ, C_{95}=2.0*σ, C_{99}=2.6*σ.

The method described here is valid only under the assumption that the distribution of the input time series are normal. Anomaly time series of SLP field can be regarded as a normal distribution. For example, Venegas et al. (1997) treated SLP anomaly time series as normal distributions and used the above method to test the significance of the correlation coefficients. However, a time series of the SIC field might not be close to a normal distribution. Suppose the climatology of SIC is 8; since the maximum of SIC is 10, the maximum positive anomaly will never be more than 2, while the maximum magnitude of a negative anomaly might be -8. If this kind of case occurs frequently, the distribution of a time series of the SIC field might be non-normal and asymmetric about the zero axis. Table 3.1 shows the distribution of SIC anomalies. The two numbers in the "range" column, for example, [-0.1, 0.1], indicate that the range of the SIC anomalies is from -0.1 to 0.1, and the value in "number" column indicates the point-times [1] number. In most cases, the anomalies are concentrated around the zero axis. The number of point-times with positive anomaly and the number of point-times with negative anomaly of the same magnitude are almost symmetrical about zero. That implies that the distribution of the time series of the SIC field is close to normal. So the above method for the significance test is approximately valid even for the SIC field.

[1] For one observation time, there are 458 ocean grid points; there are a total of 456 observation times. Taking the spatial and temporal domain into consideration simultaneously, there are 458 * 456 = 208848 point-times.

range	number	range	number
		[-0.1, 0.1]	162267
[0.1, 1.0]	20647	[-0.1, -1.0]	20485
[1.0, 2.0]	2364	[-1.0, -2.0]	2478
[2.0, 3.0]	326	[-2.0, -3.0]	260
[3.0, 4.0]	26	[-3.0, -4.0]	20
[4.0, 5.0]	1	[-4.0, -5.0]	5
[5.0, 10.0]	0	[-5.0, -10.0]	0

Table 3.1: The distribution of the SIC anomalies. The two numbers in the "range" column, for example, [-0.1, 0.1], indicate that the range of the SIC anomalies is from -0.1 to 0.1, and the value in "number" column indicates the point-times.

3.5 The presentation of SVD spatial patterns

For each SVD mode, there are two spatial patterns, the left pattern for the left field and the right pattern for the right field. Taking the k-th mode of the left field as an example, there are four ways to plot the k-th left spatial pattern: 1) We plot the left singular vector itself for the k-th left pattern. However, due to the difficulty of understanding the meaning it represents, this method is seldom chosen. 2) The k-th left pattern can be plotted as the left *homogeneous correlation map* which is defined to be the vectors $\boldsymbol{r}[\boldsymbol{s}(t),a_k(t)]$ of correlations between the grid-point values of the left field $\boldsymbol{s}$ and the k-th expansion coefficient of the left pattern, $a_k(t)$. This is a useful indicator of the geographic localization of the covarying part of the $\boldsymbol{s}$ field. 3) The k-th left pattern can be plotted as the k-th left *heterogeneous correlation map*, which is defined to be the vector of correlation coefficients between the grid point values of the left field and the k-th expansion coefficient of the *right* field and indicates how well the grid points in the left field can be predicted from the k-th mode of the right field or from the right field itself. 4) To plot the left *homogeneous regression*

map, which is generated as the left homogeneous correlation map multiplied by the temporal standard deviations of the original left data field at each grid point. The homogeneous regression maps not only illustrate the anomaly polarity but also the typical amplitude represented by the SVD modes. All these methods hold for the right field. The homogeneous regression map is chosen in this thesis to represent the spatial patterns of the SVD results.

3.6 The computer tools

The data analysis work is processed in the UNIX controlling system in the IBM work station. The main programs used are MATLAB codes.

The main commands for the the SVD analyses are: using the *"svd"* command to calculate the left singular vectors u, right singular vectors v, and the singular value matrix, l. The correlation coefficients are calculated using the *"corrcoef"* command. at the same time, the significance levels of the correlation coefficients are obtained mainly by calculating the large-lag error, σ, during which process, the *"xcov"* command is used to obtain the auto-correlation function of a time series. The power spectrum of the expansion time coefficients are calculated using the program provided to us by Drs. Mann and Park (1993). The main command used in the Monte Carlo significance test is the one used to create the random numbers, *"randperm"*. The very useful command dealing with the change of dimensions of a matrix is *"reshape"*.

The plotting tool used to plot the contours in various maps are the NCAR Graphic, which are available in the ECHO work station in our department.

Chapter 4

The variability of SIC and SLP: EOF analyses

The purpose of this chapter is to analyze independently the variability of the sea-ice concentration and the sea-level pressure using the EOF analysis method. By doing this, we will compare the two sets of independent EOFs with the coupled SVD mode obtained for the atmosphere-sea ice system in chapter 5. Only a brief discussion of the EOF (independent) modes of variability is given here, since this study concentrates on the SVD (coupled) modes.

4.1 The SIC variability

An EOF analysis is performed on the unnormalized monthly SIC anomalies north of 45^0N for the period 1954—91. The three leading EOF modes together account for 28.8% of the total monthly SIC variance. Individually, they explain 14%, 7.5%, and 6.9% of the variance (Table 4.1).

The low percentage of variance explained by the leading EOF modes of GISST2.2 SIC monthly anomaly data may be due to two reasons. First, the inclusion of small spatial scale features due to the different grid coordinates used for the GISST2.2 data reduces the variance explained by the leading EOFs. This was already observed by

mode	variance explained (%) of SIC
EOF_1	14
EOF_2	7.5
EOF_3	6.9

Table 4.1: The variance explained by the leading EOFs of the monthly anomaly SIC data.

Koide and Motoi (1998) and Tang et al. (1994). In their study, Koide and Motoi used two different data sets, the NSIDC (NOAA supported National Snow and Ice Data Centre's sea-ice concentration data set) and GISST2.2, to perform the EOF analyses separately. Although the spatial patterns of their first EOF modes of the two data sets are almost identical, the EOF_1 of the NSIDC SIC data explains 41.4% of the variance, while the EOF_1 of the GISST2.2 SIC data explains only 23.2% of the variance. The second reason is that monthly data are used in this study instead of winter averaged data (February–April mean). Despite the filtering we used to eliminate the annual signal, it still remains in the monthly anomaly data, which can account for the reduction in the percentage of variance explained by the EOF modes. Besides, most of the variability of SIC is concentrated in the winter season and is flat in the non-winter seasons. The inclusion of the non-winter season into the present study hence also reduces the variance explained (Tang et al., 1994). However, it is shown that the main results are not affected by the annual cycle and the low percentage of the variance explained (S. Venegas, 1997, personal communication).

4.1.1 EOF_1(SIC)

The EOF_1(SIC) spatial map (Fig. 3, top left) shows a dipole structure of SIC anomalies in both the Atlantic and Pacific sectors: the anomalies to the east and west of Greenland are of opposite sign, as are those in the Bering Sea and the Sea of Okhotsk. These seesaw-like features are in accordance with the sea-ice variability for individual

ocean basins noted by Mysak and Manak, (1989); Slonosky et al., (1997); and Tang et al., (1994). The spatial variability has larger amplitude in the Atlantic side, with anomalies of one sign in the Barents Sea, Norwegian Sea and Greenland-Iceland Sea (hereafter called the "BNGI" region) and anomalies of opposite sign in the Baffin Bay, Davis Strait, Labrador Sea and off the Newfoundland area (hereafter called the "BDLN" region). A similar dipole structure is found in the Pacific sector between the Bering Sea and the Sea of Okhotsk. We note that the variability in the BNGI region is in phase with that of the Sea of Okhotsk, and out of phase with the signals in the BDLN region and the Bering Sea. The dipole structures in the Atlantic and the Pacific sectors suggest that part of the sea-ice variability in the Pacific sector is concurrent with the Atlantic sea-ice variability, although the sea-ice variability in the Pacific sector is much weaker.

The EOF_1s of Koide and Motoi (1998) from two different winter average data sets are very similar to EOF_1 (Fig. 3, top left) for both the Pacific and the Atlantic side. This similarity suggests that most of the variability of SIC is concentrated in the winter season (February–April, as defined in Koide and Motoi's study). EOF_1(SIC) is also basically similar to the corresponding EOF of Slonosky et al. (1997). However, the dipole structure in the Pacific sector is very weak in Slonosky et al. This difference might be due to the fact that Slonosky et al.'s winter season (December, January and February) is two months ahead of Koide and Motoi's winter season. If this explanation holds, then the SIC anomalies in the Pacific area associated with the first EOF mode are more concentrated in the late winter than in the middle of winter. In the Atlantic sector, on the other hand, the SIC variability shows no obvious difference between the middle and late winter season.

In Fig. 3 bottom left, we note that the annual cycle is still partly present in the expansion coefficient of EOF_1(SIC) even though the climatological seasonal cycle has been removed. These peaks result from the relatively strong memory of the SIC from one year to the next and the strong amplitude of the annual cycle. They may also be due to the narrow range of the SIC values (from 0 to 10). The 25-month-running

mean of the expansion coefficient time series can cleanly remove these high frequency signal.

The smoothed expansion time coefficient of EOF_1(SIC) in Fig. 3 bottom left, shows large positive values for the period 1964–1970 and negative values for the period 1971–1975. These values together with the positive spatial anomalies in the BNGI region imply large (small) persistent sea-ice extent in the late 1960s (early 1970s) in the BNGI region. In the BDLN region, on the other hand, we find large negative (positive) sea-ice extent during the period 1964–1970 (1971–1975). These results are consistent with previous observations (e.g., Dickson et al., 1988; Agnew, 1993) and correspond to the 1960s/70s Great Ice and Salinity Anomaly (GISA) event in the northern North Atlantic. The positive SIC anomalies in the BDLN region reached their maximum around 1972, several years after the maximum in the BNGI region which occurred around 1968–69. This pattern is consistent with the advection hypothesis of sea-ice anomalies (Mysak et al., 1990).

From 1977 to 1981 the expansion time coefficient of EOF_1(SIC) shows a secondary large positive peak, which is followed by a narrow negative peak around 1983–84. This pattern suggests the existence of a 1970s/80s Ice and Salinity Anomaly (ISA) event, a decade or so after the GISA. However the sea-ice extent in the BNGI region during 1977–81 is not as large as that in the late 1960's. The fact that the negative trough associated with the 1970s/80s ISA is deeper than that of the 1960s/70s GISA event suggests that the ice extent in the early 1980's in the BDLN area was even larger than that in the GISA event. This is consistent with the observations at the east of Newfoundland area by Deser and Blackmon (1993), and by Deser and Timlin (1996). Fig. 1 shows the observations by Deser and Timlin (1996) modified by Belkin et al., 1998. Agnew (1993) also found that the maximum ice extent in Davis Strait and the Labrador Sea associated with the 1970s/80s ISA event occurred in 1984, with an anomaly of 407,000 km^2 ice cover, 85,000 km^2 more than that in 1972. The relatively heavy ice conditions in the BDLN region during the 1970s/80s ISA event was preceded by relatively light ice conditions about four years earlier in the upstream areas (the

BNGI region). This suggests that the anomalously heavy ice conditions in the BDLN region during the 1970s/80s ISA event were unlikely due to advection of ice from the upstream region as was the case during the 1960s/70s GISA event. Belkin et al. (1998) also found a similar result in their analysis of salinity and temperature data in these two regions.

The third peak in the expansion coefficient of EOF_1(SIC) is centered near 1987–1988, while the third trough spans the period 1989–1991. The third peak and trough together with the spatial pattern suggest the existence of an 1980s/90s ISA event. However, the peak in the expansion coefficient associated with this event is very weak, suggesting that the ice conditions were not very heavy in the BNGI region. Mysak and Power (1991,1992) have also noticed anomalously positive SIC anomalies in the Greenland Sea in the late 1980s. This is also consistent with the observations by Agnew (1993), who showed that there existed a moderate positive sea-ice cover anomaly of 88,000 km^2 in the Greenland Sea during 1988.

In addition to the distinct peaks and troughs shown in the expansion coefficient of EOF_1(SIC), there exists since the late 1960s an obvious decreasing trend of SIC in the BNGI region and the Sea of Okhotsk. This decreasing trend in the past three decades coincides with a surface temperature increase over this time period, described by Chapman and Walsh (1993).

4.1.2 EOF_2(SIC)

The spatial pattern of EOF_2(SIC) (Fig. 4, top left) shows mainly a one-signed structure in the Pacific Sector. Thus the anomalies of SIC in the Sea of Okhotsk and the East Siberian Sea have the same sign as those in the Bering Sea, which show a relatively larger amplitude. In the Atlantic sector, the SIC anomalies in the Gulf of St. Lawrence, Greenland Sea and Norwegian Sea have the same sign as those in the Pacific Sector. However the fluctuations of SIC in the Barents Sea are of opposite sign.

The smoothed expansion time coefficient of EOF_2(SIC) (Fig. 4, bottom left)

shows interannual variability superimposed on the annual cycles. The big positive peaks around the years 1980–82 and 1985–87 together with the large negative spatial variability in the Gulf of St. Lawrence, Baffin Bay, and the Bering sea suggest that during these periods, those regions had abnormally light SIC conditions. This mode of SIC picks up some anomalies of the 1970s/80s ISA event in the BDLN region.

4.1.3 EOF_3(SIC)

The spatial pattern of EOF_3(SIC) (Fig. 5, top left) shows mainly a one-signed structure in the Pacific Sector, thus the anomalies of SIC in the Sea of Okhotsk, East Siberian Sea, Chukchi Sea and Beaufort Sea have all the same sign. The amplitude of the SIC anomalies in the Bering Sea is very small. The larger SIC anomalies associated with EOF_3(SIC) are concentrated around the Sea of Okhotsk. The spatial variability of SIC in the Atlantic sector has the opposite sign of that in the Pacific sector, except a small area around 50^0E, 70^0N.

The expansion time coefficient (Fig. 5, bottom left) clearly shows that this mode is dominated by interannual SIC variability.

4.2 The atmospheric Variability

An EOF analysis is performed on the unnormalized monthly SLP anomalies north of 45^0N for the period 1954–91. The three leading EOF modes together account for 52.4% of the total monthly SLP variance. Individually, they explain 28%, 12.7%, and 11.8% of the variance (Table 4.2).

4.2.1 EOF_1(SLP)

The spatial pattern of EOF_1(SLP) (Fig. 3, top right) has a sandwich structure, with a large area of negative anomalies over the Arctic and N. Atlantic, surrounded by positive anomalies at lower latitudes.

mode	variance explained (%) of SLP
EOF_1	28
EOF_2	12.7
EOF_3	11.8

Table 4.2: The variance explained by the leading EOFs of the monthly anomaly SLP data.

This dominant negative anomaly cell has two centres of action of equal amplitude (-3.0 hPa): one over southeastern Greenland, the other over the Kara Sea and northern Russia. This negative anomaly area is flanked by weaker centres of opposite sign over the Bering Sea (1.5 hPa) and Western Europe (2.5 hPa). The fact that the spatial part of EOF_1(SLP) has the largest amplitudes over the northern and subtropical North Atlantic suggests that this mode is closely related to the North Atlantic Oscillation (NAO) pattern. Table 4.3 shows that EOF_1(SLP) and the NAO index are significantly correlated, with correlation coefficient **0.75**[0.44]. The NAO index is defined as the average SLP difference between Azores and Iceland from December to March. When doing the correlations between the NAO and the EOF expansion time series, only the winter averaged data (December to March) are used.

The sandwich structure of the spatial variability of SLP closely resembles the EOF_1 of winter SLP obtained by Slonosky et al. (1997), although they used only winter averaged data. This similarity indicates that most of the variability of the SLP field occurs during the Northern Hemisphere winter season.

The expansion time coefficient of EOF_1(SLP) (Fig. 3, bottom right) is characterized by a mixture of interannual and higher frequency fluctuations. The large negative peak around year 1968 together with the negative anomalies over southeastern Greenland and the Kara Sea suggest that the SLP was abnormally high over those regions around 1968. The large positive peak around 1990 suggests abnormally low SLP conditions in those regions.

4.2.2 EOF_2(SLP)

Unlike EOF_1(SLP), most of the spatial variability of EOF_2(SLP) (Fig. 4, top right) is concentrated in the Pacific Sector, and centered over the Bering Sea; the amplitude of the anomalies is up to 5.5 hPa. This positive anomaly cell of SLP reflects the fluctuations of the Aleutian Low. Over the Atlantic sector, there is a weak dipole structure of SLP anomalies, with a positive anomaly cell of 1.0 hPa over Greenland and a negative anomaly cell of -1.5 hPa over N Atlantic.

The peaks on the smoothed expansion time coefficient of EOF_2(SLP) (Fig. 4, bottom right) during the periods 1960–67 and 1971–72 together with the positive spatial variability over the Bering Sea suggest that the Aleutian low is weak during these periods, and slightly shifted towards the northwest. The troughs around 1970, 1976 etc., suggest that the Aleutian Low is strong and slightly southeastwards shifted during these periods. The short time intervals between the peaks and troughs suggests that this EOF_2(SLP) mode is associated with strong interannual variability. Superimposed upon the interannual signals, there is a decreasing trend.

modes	$EOF_1(SLP)$	EOF_2(SLP)	EOF_3(SLP)	NAO
EOF_1(SIC)	**-0.21**[0.20]	**0.27**[0.23]	**-0.15**[0.11]	**-0.56**[0.47]
EOF_2(SIC)	**-0.22**[0.20]	-0.03[0.22]	-0.09[0.13]	-0.04[0.41]
EOF_3(SIC)	-0.08[0.17]	0.19[0.21]	0.05[0.12]	0.09[0.36]
NAO	**0.75**[0.44]	-0.38[0.46]	-0.02[0.23]	1[0.56]

Table 4.3: Correlation coefficients between the first three EOF modes of SIC and SLP, and between these modes and the NAO Index. Numbers in brackets are the 95% significance levels calculated for each correlation (Sciremammano, 1979). Significant correlations are in bold face.

4.2.3 EOF_3(SLP)

The EOF_3(SLP) spatial pattern (Fig. 5, top right) reveals large SLP anomalies mainly over northern Russia, with a positive anomaly cell of 3.0 hPa sitting over 40^0E, 60^0N. Another positive anomaly cell is located over the northeast Pacific, with an amplitude of up to 1.5 hPa. The main negative anomaly cell is over southeast Greenland, with an amplitude of -2.0 hPa.

The smoothed expansion time coefficient of EOF_3(SLP) (Fig. 5, bottom right) is characterized by interannual and higher frequency oscillations.

4.3 Relating the SIC and SLP behaviours

To look for possible links between SIC and atmospheric fluctuations, the correlation coefficients between the time series of the three discussed SIC and SLP modes are calculated and displayed in Table 4.3. Correlations with the time series of the North Atlantic Oscillation (NAO) Index are also included to test for possible links with the NAO pattern. The table shows that EOF_1(SIC) is significantly correlated with all of the three leading modes of SLP and with the NAO index.

In view of the significant correlation between EOF_1(SIC) and EOF_1(SLP), lagged

correlations between the expansion time coefficient of EOF_1(SIC) and EOF_1(SLP) were also computed (Fig. 6, top left). This figure indicates that the two modes are best correlated (r=-0.29) when the atmosphere leads the sea ice by 1–5 months. This suggests that atmosphere-to-ocean forcing links these two modes of variability. Besides the EOF_1(SLP), EOF_1(SIC) is also significantly correlated with EOF_2(SLP) and EOF_3(SLP) (Table 4.3), which is confirmed by the lagged correlations (Fig. 6, top right and bottom left). At the 99% level, the EOF_3(SLP) leads SIC by 1 month, whereas EOF_2(SLP) leads SIC by 37 months. This suggests that the SIC fluctuations over the Atlantic sector are significantly correlated not only with the SLP anomalies over the Central Arctic (Fig. 3, top right) but also with the prior SLP anomalies over the Aleutian Low indicated by EOF_2(SLP) (Fig. 4, top right), and over northern Russia, indicated by EOF_3(SLP) (Fig. 5, top right). However, the mechanisms that explain those teleconnections need to be determined. EOF_1(SIC) is also significantly correlated with the NAO index at the 95% level (Table 4.3, Fig. 7, top), which is understandable as EOF_1(SLP) is similar to the NAO pattern and EOF_1(SLP) is correlated with EOF_1(SIC).

EOF_2(SIC) is significantly correlated with EOF_1(SLP) (Table 4.3). Lagged correlations between the expansion time coefficients of EOF_2(SIC) and EOF_1(SLP) (Fig. 6, bottom right) show that the maximum correlation takes place when the atmosphere is leading the SIC anomalies by one month. Unlike with EOF_1(SIC), the correlation between the second mode of SIC anomalies and the NAO index is very weak.

Chapter 5

The results of SVD analyses

To better assess and confirm the relationships between SIC and SLP variations obtained in Chapter 4, a singular value decomposition (SVD) is performed on the cross-covariance matrix between the two fields. In contrast to the EOF analysis performed on the individual fields in the previous chapter, the SVD analysis on the two fields together will identify *only* those modes of behavior in which the SIC and SLP variations are strongly coupled.

Table 5.1 shows the statistics, i.e., the squared covariance fraction (SCF) and the variance of the SIC and SLP anomalies explained by each mode. From Table 5.1, one can see that the three leading SVD modes of the coupled SIC and SLP fields account for 54%, 16% and 7% of the total squared covariance, respectively. The first three SVD(SIC) modes explain 12%, 9%, and 6% of the variance associated with the SIC monthly anomaly data. The first three SVD(SLP) modes explain 26%, 18%, and 12% of the variance associated with the SLP monthly anomaly data.

Table 5.2 shows the lag-correlation coefficients between the expansion time coefficients of SVD_k(SIC) and SVD_k(SLP). The 0-lag correlation coefficients are 0.50 [0.23] for SVD_1, 0.45 [0.23] for SVD_2, and 0.47 [0.19] for SVD_3; the number in square brackets is the corresponding 95% significance level. These correlations indicate that the SLP and SIC seem to be slightly more strongly coupled in the first and third modes than in the second mode. The correlations are generally higher with SLP leading SIC

mode	SCF (%)	variance of SIC(%)	variance of SLP(%)
SVD_1	54	12	26
SVD_2	16	9	18
SVD_3	7	6	12

Table 5.1: The statistics of the leading SVD modes of the monthly anomaly data.

SLP leads	r[SVD_1(SIC) ,SVD_1(SLP)]	r[SVD_2(SIC) ,SVD_2(SLP)]	r[SVD_3(SIC) ,SVD_3(SLP)]
2 months	0.56	0.40	0.46
1 month	0.57	0.448	0.53
0 month	0.50	0.45	0.34
-1 month	0.38	0.39	0.34
-2 months	0.27	0.30	0.21

Table 5.2: Lagged correlations between SIC and SLP within the same SVD mode, for different short lags. Positive lags mean SLP leading SIC.

than with SLP lagging SIC.

5.1 The first mode: the decadal-scale mode

In this section, the relationship between SVD_1(SIC) and SVD_1(SLP) is investigated first by comparing the spatial and temporal variability of SVD_1(SIC), SVD_1(SLP), and the associated anomalous wind stress, and then by performing composite and correlation analyses.

5.1.1 SVD_1(SIC)

From Table 5.1, we note that SVD_1(SIC) explains 12% of the variance of the monthly anomaly SIC data. This is comparable to the 14% of the variance explained by EOF_1(SIC).

The spatial pattern and the expansion time coefficient of SVD_1(SIC) (Fig. 8, top left and bottom left) are basically similar to those of EOF_1(SIC) (Fig. 3, top left). The highly significant (at 95% level) correlation between the expansion coefficients of EOF_1(SIC) and SVD_1(SIC), (r = 0.88[0.35], see Table 5.3), confirms this similarity.

The three distinct peaks and troughs shown in the smoothed expansion coefficient time series of SVD_1(SIC) indicate that this mode depicts a decadal oscillation (Fig. 8, bottom left). The power spectrum (Fig. 9, top left) of the unsmoothed expansion time coefficient indicates that besides a broad annual peak, there is a large, wide peak at periods of about 8–12 years. The power spectrum of the smoothed SVD_1(SIC) time series (Fig. 10, top right) shows a very broad peak of energy centered around 10 years. Therefore, we can think of SVD_1(SIC) as having a quasi-decadal periodicity.

5.1.2 SVD_1(SLP)

In the way that SVD_1(SIC) mimics EOF_1(SIC), SVD_1(SLP) (Fig. 8, top) is basically similar to the corresponding EOF_1(SLP) mode (Fig. 3, top right), but with the sign reversed. The strong negative correlation between the expansion time coefficients

correlation coefficient	SIC	SLP
r[SVD_1, EOF_1]	0.88 [0.35]	-0.93[0.23]
r[SVD_2, EOF_2]	-0.51[-0.38]	0.79[0.19]
r[SVD_3, EOF_3]	0.06 [0.3]	-0.57[-0.15]
r[SVD_2(SIC), EOF_3(SIC)] = 0.39[0.37]		
r[SVD_3(SIC), EOF_2(SIC)] = 0.65[0.32]		

Table 5.3: The temporal lag-correlation coefficients between the expansion time coefficients of the leading EOFs and SVDs. r[SVD_1, EOF_1] represents the correlation between the time coefficient of SVD_1(SIC)/SVD_1(SLP) and EOF_1 of SIC/or SLP.

of SVD_1(SLP) and that of EOF_1(SLP), -0.93[-0.23], and the opposite signs of their spatial variability imply that SVD_1(SLP) and EOF_1(SLP) are almost identical. The similarities between SVD_1 and EOF_1 for both ice and atmosphere suggest that SVD_1 not only explains the maximum covariability between the coupled fields, but also the maximum variance of each climatic variable.

The power spectrum of the unsmoothed SVD_1(SLP) expansion time coefficient (Fig. 9, bottom left) shows a significant peak at a period of 2–3 years, suggesting that SVD_1(SLP) is associated with strong interannual variability. The fact that the two distinctive peaks with periods of about 8 years and 20 years are below the 95% significance level suggests that the long timescale oscillations of SVD_1(SLP) are much weaker than the interannual variability. However, after smoothing with the 25-month-running mean, these two peaks stand out significantly (Fig. 9, bottom right). The power spectrum of the smoothed expansion time coefficients suggests that SVD_1(SLP) is also in part a quasi-decadal mode.

5.1.3 The relationship between SVD_1(SIC) and SVD_1(SLP)

From the smoothed expansion coefficients of both SVD_1(SLP) and SVD_1(SIC) (drawn together in Fig. 10, top) , one can see that, in general, the SIC and SLP fluctuations appear to be almost in phase; however, the lagged correlations in Fig. 11, bottom show SLP leading SIC by one or two months. Thus this mode represents mainly an atmosphere-to-sea ice forcing. The maximum correlation, r=0.58[0.22], between the unsmoothed expansion time coefficients of SVD_1(SIC) and SVD_1(SLP) occurs with SLP leading SIC by 1 to 2 months; this indicates quite a strong coupling at this lag.

However, there is one exception to the case of SLP generally leading SIC in this mode, and it occurs during 1965—70 (Fig. 10, top). Shortly after 1965, one can see clearly that SLP is leading SIC by several months. But in the late 1960s, the opposite is true. This exception with SLP lagging SIC might indicate that the already built up heavy ice conditions in the BNGI region might result in positive SLP anomalies over the central Arctic, European sub-Arctic, and the northern North Atlantic, although it is also possible that both the heavy ice conditions and the high SLP might be caused by some other unknown processes.

Besides the analysis of the expansion time coefficients, a comparison between the spatial structure of SVD_1(SLP) (Fig. 8, top right) and SVD_1(SIC) (Fig. 8, top left) can also give us information about the relationship between these two climatic variables, provided we recall that the time coefficients imply that SVD_1(SLP) leads SVD_1(SIC) by 1 to 2 months.

From the spatial map of SVD_1(SIC) and the anomalous wind pattern one month earlier (Fig. 11, top) that can be deduced from SVD_1(SLP) (Fig. 8, top right), one can see that generally 1 to 2 months before the positive SIC anomalies occur in the Sea of Okhotsk, there is a moderate negative SLP anomaly cell over Kamchatka (Fig. 8, top right). The SLP gradient at the polar edge of this moderate negative anomaly will result in an anomalous northeasterly wind, almost in the same direction as the climatological wind over this area (Fig. 2, top). This results in strengthening of the climatological northeasterly wind. This strengthened northeasterly wind helps the

relatively warm Sea of Okhotsk to lose more sensible and latent heat to the cooler atmosphere, which results in heavier-than-normal ice conditions in the Sea of Okhotsk. Similarly, this negative SLP anomaly cell contributes to the light ice conditions in the Bering Sea (Fig. 8, top left).

A strong positive anomaly cell of SLP centered over south-eastern Greenland and a strong negative anomaly cell over western Europe exist two months before the negative SIC anomalies in the BDLN region (Fig. 8, top). These positive and negative SLP anomaly cells result in anomalous easterly or south-easterly winds over the BDLN region, which in turn reduce (or even change the direction of) the climatological westerly winds. The weaker-than-normal westerly winds over the BDLN region reduce the heat loss from the ocean to the atmosphere, allowing the ice edge to retreat towards the coast and hence reducing the ice formation in this region. The same reasoning is true with the signs reversed. Hence, the structure of the SIC anomalies in the BDLN region can also be explained as the result of the overlying SLP anomaly structure.

Over the European Sub-Arctic, 1 to 2 months before the heavy ice conditions in the BNGI region, the centre of the Central Arctic positive SLP anomaly cell sits over the Barents Sea (Fig. 8, top right). This suggests that the SIC anomalies in the Barents Sea might not be explained by a local relationship with the atmospheric circulation. However, they might be due to the shift of the TDS towards the Eurasian-coastline, which in turn resulted from the weak SLP gradient associated with the higher-than-normal SLP over the Eurasian coastline of Arctic.

The positive SIC anomalies in the Norwegian Sea and the Greenland-Iceland Seas can be described as the result of the positive SLP anomaly cell over Greenland 1 to 2 months earlier. The strong gradient over the north-eastern side of this positive SLP cell results in anomalous north-easterly winds in the Norwegian Sea which are in the same direction as the climatological north-easterly winds and hence help export more Arctic sea ice and fresh water to these seas. At the same time, the strong gradient associated with this positive SLP anomaly cell over eastern Greenland results in

anomalous westerly winds blowing off shore near the east of Belgica bank, which blows the ice towards the centre of the sea and lets the shallow coast areas be open where the ice formation process is much quicker than in the deep ocean region. Besides, these anomalous westerly winds bring cold continental air from Greenland towards the ocean and hence help produce sea ice off the coast. Additionally, the offshore anomalous westerly winds along the Greenland coastline of the Arctic reduce the amount of Arctic sea ice and fresh water driven westwards into the Arctic and hence increase the amount of sea ice and fresh water flowing towards Fram Strait, which will subsequently enter the Norwegian Sea and Greenland-Iceland Seas.

An alternate way to explain the SIC anomalies in the BNGI region is related to the difference of sea level between the origin of the TDS (the East Siberian Sea) and the head of the TDS (Fram Strait), which in turn resulted from the SLP anomalies. If the SLP is higher than normal over the Beaufort Gyre, Chukchi Sea and Eastern Siberian Sea, then the associated convergence winds will make the sea level slightly higher than normal (Proshutinsky and Johnson, 1997). If there is a positive SLP anomaly cell over south-eastern of Greenland and a negative anomaly cell over the western Europe, then the associated anomalous winds will help the water and ice to be advected downstream and hence reduce the sea level over eastern and southern Greenland. So if there are positive SLP anomalies over the Beaufort Sea, Chukchi Sea, East Siberian Sea, and southeast of Greenland and the negative anomalies over the western Europe concurrently exist, the difference of sea levels between the origin and head of the TDS will be enlarged and hence more ice and fresh water will flow from Arctic through Fram Strait into the BNGI region. The same reasoning is true reversing the signs.

To obtain a deeper understanding of the relationships between the SIC anomalies and the overlying atmospheric circulation fluctuations, SVD_1(SIC) is redrawn in Fig. 11 with the inclusion of wind stress field associated with this mode, with wind stress leading or lagging SIC by one month. The associated wind field is estimated as the spatial vector correlations between SVD_1(SIC) expansion time coefficient and the

time series of u- and v-components of the wind anomalies at each grid point. The wind stress is estimated from the vector wind correlations in the way described in section 2.2 of chapter 2. As mentioned in section 2.2, the wind stress field is an underestimate of the true value. The larger the wind stress anomalies, the more they are underestimated. The lag time of one month is chosen because it is found that the interactions between air and ice are strongest with atmosphere leading ice by 1 to 2 months.

The maximum correlation between SVD_1(SIC) and the wind stress anomalies is 0.65[0.23] in the case of wind stress leading ice by one month (Fig. 11, top). The corresponding maximum correlation is 0.45[0.24] in the case of wind stress lagging ice by one month (Fig. 11, bottom), which reaffirms the hypothesis of an atmospheric-driven mode. However, the wind stress anomalous pattern for SIC anomalies leading atmosphere by one month is quite similar to the corresponding pattern for wind leading the SIC by one month. This similarity suggests that the ice is not passively affected by the atmospheric forcing, but the latter is in turn also affected by the anomalies of sea ice. The already built-up sea ice might have some positive feedback on the atmosphere. Heavy sea-ice conditions in the BNGI region are caused by higher-than-normal SLP over the central Arctic, European sub-Arctic, and especially over the Greenland-Iceland area. Once the heavy sea-ice conditions have set up, they may lead to cooler air temperature and thus higher SLP over these areas by reducing the sensible and latent heat fluxes from the ocean to the overlying atmosphere. The possible SLP anomalies will then increase the sea-ice extension further, and so on. In this way, a positive feedback on the short timescale (several months) might be created between the sea ice and the overlying SLP. This positive feedback may be one of the reasons why the positive sea-ice anomalies in the BNGI region can persist for several years. However, further study would be necessary for a better understanding of this mechanism.. The response of SLP to sea ice will be further investigated in sections 5.1.4 and 5.1.5.

5.1.4 Composite analysis based on SVD_1(SIC)

To further study the relationship between SIC anomalies and the overlying atmospheric circulation fluctuations, the composite analysis method is used. The SLP and wind composites are based on the unsmoothed SVD_1(SIC) expansion time coefficient (Fig. 9, bottom left). The SLP composite anomaly maps corresponding to heavy (light) ice conditions are calculated as the time averages of SLP anomalies two months before/after each of the key months associated with heavy (light) ice conditions in the BNGI region. Similarly, the wind composite anomaly maps are obtained. The key months with heavy or light ice conditions in the BNGI region during each ISA event are shown in Table 5.4. Due to the dipole structure of SVD_1(SIC), it should be kept in mind that the " peak (trough)" sea-ice conditions here refer to the ice conditions in BNGI region, and could also be refer to as the "trough (peak)" ice conditions in the BDLN region. The threshold values for choosing heavy or light ice conditions for each ISA event are given in Table 5.5. The difference between threshold values is due to the existence of an obvious decreasing trend associated with the SVD_1(SIC) expansion time coefficient. It would be more objective if one first detrend the SVD_1(SIC) expansion coefficient before perform the composite analysis (personal communication, 1998, S. Venegas).

The 1960s/70s GISA event

From Fig. 12, one can see clearly that the SLP anomalies are much stronger when they are leading than when they are lagging the peak (trough) ice conditions by 2 months in the BNGI region. This is another indication of the atmospheric forcing the ice hypothesis. The spatial patterns of the SLP composites two months before the heavy (light) ice conditions in the BNGI region closely resemble (are opposite of) the SVD_1(SLP) spatial pattern, shown in Fig. 8.

As mentioned in the previous section, there is a short timescale positive feedback between the SIC anomalies and the overlying atmospheric circulation. However, this positive feedback cannot go on forever. The positive SLP anomaly cell off the eastern

months	*1960s/70s GISA*		*1970s/80s ISA*		*1980s/90s ISA*	
	peak	trough	peak	trough	peak	trough
	Feb.66	Apr.72	Jan.79	Jan.83	Feb.87	Feb.90
	Mar.66	Apr.73	Feb 79	Feb.83	Mar.87	Mar.90
	Apr.66	Mar.74	Mar.79	Jan.83	Jan.88	Apr.90
	May 66	Apr.74	Apr.79	Feb.83	Nov.88	May 90
	Nov.68	Jan.75	May 79	Mar.83		Jan.91
	Dec.68	Feb.75	May 81	Jan.84		Feb.91
	Jan.69	Mar.75		Feb.84		Mar.91
	Feb.69	Apr.75		Mar.84		Apr.91
	Mar.69	Mar.76		Apr.84		May 91
	Apr.69	Apr.76		May 84		Jun.91
	May 69	May 76		Jun.84		
	Jun,69					
total	12 months	11 months	6 months	11 months	5 months	10 months

Table 5.4: The key months with heavy or light ice conditions in the Barents Sea, Norwegian Sea, Greenland Sea, and Iceland Sea (BNGI) region during the 1960s/70s GISA, 1970s/80s ISA and 1980s/90s ISA events, based on the expansion time coefficient of SVD_1(SIC), shown in Fig. 8, bottom left.

Threshold	*1960s/70s GISA*	*1970s/80s ISA*	*1980s/90s ISA*
peak	1.88	1.65	0.4
trough	-1.65	-1.65	-1.65

Table 5.5: Thresholds for the peak and trough ice conditions for each of the ISA events. The unit is the standard deviation of the time series of SVD_1(SIC) for the whole period: 1954—91.

coast of Greenland two months before the heavy ice conditions in the BNGI region (Fig. 12, top right) becomes more compact and well separated from the positive SLP anomaly cell over central Greenland two months after the heavy ice conditions of the 1960s/70s GISA (Fig. 12, bottom right). The western edge of this separated positive anomaly cell results in anomalous southerly winds, which weaken the climatological north-easterly winds there, and hence reduce the ice export from the Arctic through the Fram Strait into the Greenland-Iceland Seas. The cessation of this short timescale feedback might be supported by the fact that there is no significant lag correlation between SVD_1(SIC) and the time series of SLP anomalies at each grid point when SLP lags SIC by 6 months (Fig. 16, bottom right).

The 1970s/80s ISA event

The SLP composite maps two months before the 1970s/80s ISA peak ice conditions in the BNGI region (Fig. 13, top right) are generally similar to the corresponding ones of the 1960s/70s GISA (Fig.12, top right). There are, however, two differences in the pattern. Firstly, the anomalous southerly winds over the Norwegian Sea reduce the ice extent there; secondly, the atmospheric circulation fluctuations are weaker for the 1970s/80s ISA event than for the 1960s/70s GISA event in the central Arctic, Eurasian sub-Arctic, and especially the northern North Atlantic. These two exceptions help to explain why the positive SIC anomaly in the BNGI region in the late 1970s is much weaker than that in the late 1960s. In the Pacific sector, a closed strong low system centered at about 53^0N,170^0W exists two months before the heavy (light) ice conditions in the Sea of Okhotsk (the Bering Sea), which helps the ice formation in the Sea of Okhotsk, and reduces the ice formation in the Bering Sea area. The SIC extent in the Pacific sector is consistent with the local atmospheric circulation anomalies. The anomalous low SLP system centered about 53^0N,170^0W and the positive anomaly cell over the south of the Bering Sea are much stronger than the corresponding ones in the late 1960s. This suggests that the portion of SIC anomalies in the Pacific sector which are in phase with the ISA events are much stronger in the

case of the 1970s/80s ISA than in the case of the 1960s/70s GISA.

The differences between the SLP composite two months before the heavy ice conditions in the BDLN region during the 1970s/80s ISA (Fig. 13, top left) and that of the 1960s/70s GISA (Fig. 12, top left) are very obvious in the west side of Greenland, Baffin Bay and Labrador Sea. The 1970s/80s ISA event is associated with a stronger positive NAO pattern and stronger anomalously northerly or north-westerly winds. These northerly winds which blow along the west coast of Greenland and north-westerly winds which blow along the coast of Labrador carry cold air to the BDLN region from the north, or from Greenland and northern North America. Besides the cold air, the anomalous winds also carry more than normal cold sea water to the Baffin Bay, and the Labrador Sea and strengthen the local ice conditions in these areas. This stronger ice formation process in the 1970s/80s ISA compared to that in the 1960s/70s GISA might cause the heavier ice conditions observed in the Labrador Sea during the early 1980s compared to that in the early 1970s (Table 1 of Agnew, 1993), although the upstream ice conditions several years earlier is not as heavy in the late 1970s as in the late 1960s.

However, in the region east of Newfoundland, the heavy SIC conditions in the early 1980s can't be explained by the SLP anomaly at all. They might be controlled by cold air temperatures (Prinsenberg *et al.*, 1996) or by advection of sea ice from the Labrador Sea.

The 1980s/90s ISA event

For the case of the 1980s/90s ISA event (Fig. 14, top), there exist prevalent negative SLP anomalies over the central Arctic with SLP leading by two months the heavy ice conditions in the BNGI region. The combined effects of the negative SLP anomaly cell over Greenland and the positive one over the Kara Sea (Fig. 14, top right) prevent the export of Arctic sea ice and fresh water through Fram Strait to the Norwegian Sea and the Greenland-Iceland Seas. Mysak and Power (1990) suggest that the positive SIC anomalies in 1988 in the Greenland Sea might be due to the large amount of

precipitation over North America and the large amount of river runoff in the Western Arctic two to three years earlier.

The heavy ice conditions in the BDLN region during the 1980s/90s ISA event are mainly due to the strengthened local ice formation process there caused by the anomalously northerly or north-easterly winds and the ice and fresh water export through the CAA and Nares Strait from the Arctic. The negative SLP anomalies in the central Arctic cause the TDS to shift towards the CAA and increase the amount of ice exported out of Arctic through the CAA and the Nares Strait into Baffin Bay.

Over the Pacific sector, two months before the heavy ice conditions in the Sea of Okhotsk during the late 1980s, a negative SLP anomaly cell is centered over the south of the Bering Sea. This negative anomaly is much bigger in size and magnitude than the corresponding ones that occurred during the late 1960s and 1970s. The anomalous north-easterly winds at the north-west edge of this negative anomaly help the ice formation in the Sea of Okhotsk. The south-easterly winds at the south-east edge of this cell prevents the ice formation in the Bering Sea area. So the heavy sea-ice conditions in the Sea of Okhotsk and the light sea-ice conditions in the Bering Sea derived from SVD_1(SIC) are in harmony with the results of the local atmospheric circulation fluctuations. The stronger negative anomaly cell over the south of the Bering Sea suggests that the portion of sea-ice variability in the Pacific which is in phase with the ISA event is stronger in the case of the 1980s/90s ISA event than in the case of the 1960s/70s GISA and the 1970s/80s ISA events.

Summary

In summary, the composite SLP anomalies based on the SVD_1(SIC) expansion time coefficient suggest that the severe ice conditions in the BNGI region in the case of the 1960s/70s GISA are mainly due to the anomalous sea ice and fresh water export from Arctic through Fram Strait to the Greenland-Iceland seas and partially due to local formation processes. The large sea-ice anomalies are then advected to the BDLN region about 4 years later and result in heavy ice conditions in this region. In the case

of the 1970s/80s ISA, the relatively weaker SIC anomalies in the BNGI region is due to a similar but relatively weaker pattern of the overlying SLP anomalies compared with that of the 1960/1970s GISA. The heavy ice conditions in the BDLN region in the early 1980s are partially due to the advection of sea ice from upstream (the Greenland-Iceland Seas), and partially due to the local ice formation process which is enforced by the anomalous atmospheric circulation. In the case of the 1980s/90s ISA, the atmospheric circulation fluctuations seem to prevent the ice extension in the Norwegian Sea and the Greenland-Iceland Seas. The anomalous positive ice extension in 1988 in the Greenland Sea may be due to other processes. The severe ice conditions in the early 1990s in the BDLN region is mainly due to local ice formation processes strengthened by the local atmospheric circulation fluctuations. The shift of the TDS towards the Canadian coastline of Arctic resulting from the negative SLP anomalies in the central Arctic may also contribute to the heavy ice conditions in the BDLN region in the early 1990s by exporting ice and fresh water through the CAA and Nares strait.

5.1.5 Lagged-correlation analyses based on SVD_1(SIC)

Lagged-correlation analysis gives an alternate way to understand the relationship between SIC anomalies and atmospheric circulation fluctuations. The lagged-correlation coefficient is calculated between the time series of the atmospheric monthly anomaly field at each grid point and the expansion time coefficient of SVD_1(SIC). Depending on the region of interest, there are various possible interpretations for a given correlation. A positive correlation implies that when the time series of SVD_1(SIC) is positive (i.e., when there are positive SIC anomalies in the BNGI region and the Sea of Okhotsk), the sign of the corresponding atmospheric anomaly also tends to be positive. Opposite arguments hold for negative correlations. Although it is possible that the correlations are not causal, that is, that both the sea-ice and the atmospheric circulation are responding to some third factor, this possibility becomes less likely when a reasonable physical mechanism can be proposed to explain the correlation.

Given that the pattern of SVD_1(SIC) has stronger spatial variability in the Atlantic sector than in the Pacific sector, it is probably best to assume that the atmospheric fluctuations correlate mainly with the SIC anomalies in the Atlantic sector.

In this section, the correlation maps with various atmospheric lag times will be shown. The lags considered vary from several months to up to 12 years.

With SLP leading ice by 1 year, we find positive significant correlations over the east Greenland and Norwegian Sea, part of the northern North Atlantic and north of the climatological location of the Siberian High (Fig. 15). Fig. 15 also shows some significant negative correlations east of Newfoundland and over western Europe. This suggests that the positive SLP anomalies over the northern North Atlantic and the Siberian climatological high and the negative SLP anomalies over east of Newfoundland and western Europe are consistent with the prediction of large (small) ice extents in the BNGI (BDLN) region one year later. This suggest that the SIC in the BNGI region and the BDLN region has a long memory of the atmospheric circulation fluctuations.

The spatial correlation maps with atmosphere leading ice by 2 months, 0 months, minus 2 months (negative lag means ice leading), minus 6 months, are shown in Fig. 16. From Fig. 16, one can see that the correlation with SLP leading SIC by 1 to 2 months is the strongest. This is another indication that this first SVD mode depicts an atmosphere-to-sea ice forcing. The correlation pattern with atmosphere leading sea-ice by 2 months closely resembles the SVD_1(SLP) spatial pattern (Fig. 8, top right). The significant positive correlations over Greenland and the European sub-Arctic and the significant negative correlations in the Sea of Okhotsk with sea-ice *leading* atmosphere by 2 months is similar to the corresponding one with sea-ice *lagging* ice by two months, though much weaker (Fig. 16, top left and bottom left). This suggests that at short timescales (no longer than six months), there exists a slightly significant atmospheric response to the heavy sea-ice conditions in the BNGI region. However, the correlation coefficients are only around 0.15—0.20, which implies that the atmospheric response to the SIC fluctuations is rather weak.

Although the atmosphere has no significant response to the SIC fluctuations with sea ice leading up to 6 months (Fig. 16, bottom right), the effect of the SIC anomalies on the atmosphere does not linearly decrease with longer time lags. Fig. 17 shows that maximum correlations occur when the atmosphere leads by 1 to 2 months, lags by 10 months and 22 months. Even though the 12-month interval between the maximum correlations might be due to a residual of the strong annual cycle, it shows some interesting physics. The heavy ice conditions in one year may lead to another year of heavy ice conditions in the same region mainly through the cooling (and hence freshening) of the water caused by the melting of the ice. This cooling process is supported by the observation that the heavy ice conditions east of Newfoundland are normally followed 1 to 2 years later by negative SST anomalies (Deser and Timlin, 1996). The freshening and cooling reduce the overturning of deep warm water and stabilize the sea water in the BNGI region and hence strengthens the ice formation there. In addition, after the heavy ice is formed, the short-timescale positive feedback between SLP and sea ice will cause more sea ice to form locally and blow more sea ice and fresh water from Arctic through Fram Strait to Norwegian Sea and the Greenland-Iceland Seas. Mainly due to these two mechanisms, the positive SIC anomalies can be persistent for up to several years. The heavy sea-ice conditions in a given year may be due to the heavy sea-ice conditions in the previous year. The significant long-term lagged-correlations are mainly due to the long-term memory of the sea ice, and not because the same ice directly affects SLP for up to several years.

On long timescales, significant correlations (although not high) exist between the SVD_1(SIC) expansion coefficient and the time series of SLP anomalies at each grid point with SLP lagging SIC by 1 year, 2 years, 3 years, 5 years, 6 years and even up to 12 years (Figs. 18, 19 and 20).

When SIC leads SLP by 1 year (Fig. 18, top left), the significant positive correlations are over Greenland and central North America, to the west of the heavy ice conditions in the BNGI region. One year later, when sea ice leads SLP by 2 years (Fig. 18, top right), the significant positive correlation pattern moves further west-

ward, enlarges its size, and increases its magnitude. The strong, significant positive correlation area moves westward further after 3 years and arrives over Alaska and the North Pacific when sea ice leads SLP by 4 years. When sea ice leads SLP by 5 years, the positive correlation center moves to the East of Siberia (Fig. 19, top left). The determination of the mechanism which explains this westward movement of the positive correlation center is beyond the scope of this thesis.

Of all the correlation maps with long-term lags, the strongest one is that with sea ice leading the atmosphere by 6 years (Fig. 19, top right), which shows a significant positive correlation over Eastern Siberia, the central Arctic, the European sub-Arctic, the northern North Atlantic, and especially north-eastern Canada. The large size and relatively large significant positive correlations suggest that the SLP will generally increase over these areas 6 years after the positive SIC anomaly occurs in the BNGI region. The general positive correlation pattern with ice leading atmosphere by 6 years is quite similar to the SVD_1(SLP) spatial pattern, but the effect can be very different. The positive center of action located over north-eastern Canada can help the ice extension in the BDLN region. On the other hand, the positive anomaly cell over south-eastern Greenland in SVD_1(SLP) strengthens the ice formation in the BNGI region. As the ice-cover anomalies in the BDLN and BNGI region are just of opposite signs, the SLP anomalies 6 years after the heavy sea-ice extension in the BNGI region serve to reduce the ice extension in the BNGI region, and strengthen the ice extensions in the BDLN region.

The negative correlations over North America and the Norwegian Sea start to be present when ice leads the atmosphere by 9 years. These negative correlations continue to exist with longer lag time and become significant when ice leads SLP by 12 years (Fig. 20, bottom left). This suggests that 12 years after the heavy ice conditions in the BNGI region, the SLP will be significantly lower than normal over the European sub-Arctic and a small part of northern North America. The negative correlations over the European sub-Arctic are favorable to the ice formation in the Norwegian Sea and the Barents Sea, and hence start another cycle of the SIC

anomalies.

5.2 The second mode: a long-term trend mode

The analysis procedures for the second SVD mode are similar to those of the first SVD mode. For brevity, only the differences between SVD_2 and SVD_1 will be discussed in this section. From Table 5.1, one can see that the second SVD mode explains 16% of the squared covariance. Table 5.2 shows that the maximum correlation between SVD_2(SIC) and SVD_2(SLP) is 0.45[0.23]. SVD_2(SIC) explains 9% of the variance associated with the SIC monthly anomaly data, while SVD_2(SLP) explains 18% of the SLP variance. The spatial patterns and expansion time coefficients associated with the second coupled SVD mode between SIC and SLP are shown in Fig. 21.

5.2.1 SVD_2(SIC)

Like SVD_1(SIC), SVD_2(SIC) also shows a dipole structure in both the Atlantic side and the Pacific side, but the dipoles are somewhat weaker. The anomalies in the BNGI region and the Sea of Okhotsk are of the same positive sign. The negative anomalies are very weak and occur mainly in the Bering Sea and the Labrador Sea (Fig. 21, top left). The see-saw variability is present both in SVD_2(SIC) and in SVD_1(SIC) in the Pacific sector, and is similar to SVD_1(SIC) obtained by Fang and Wallace (1994) for the Pacific basin. However, unlike the first mode which shows more variability in the Atlantic side than in the Pacific side, SVD_2(SIC) shows strong fluctuations in the Sea of Okhotsk. Besides, SVD_2(SIC) shows a sandwich structure in the American and Atlantic side: the weak negative anomalies in the BDLN region are surrounded by strong positive anomalies to the west and to the east. The positive anomalies to the west occur in Hudson Bay, Hudson Strait, the east side and head of Baffin Bay and the Gulf of St. Lawrence. The positive anomalies to the east occur in the BNGI region.

The spatial and temporal variability of SVD_2(SIC) (Fig. 21, top left and bottom

left) bares some similarity to EOF_2(SIC) (Fig. 4, top left). The correlation coefficient between SVD_2(SIC) and EOF_2(SIC) is -0.51[-0.38].

The expansion time coefficient of SVD_2(SIC) (Fig. 21, bottom left) shows the existence of a multi-decadal (25-year) oscillation, although the record is too short to show more than one cycle. Considering the similar polarity of the SIC variation in both SVD_1(SIC) and SVD_2(SIC) in the Atlantic sector, the big positive peak during the whole 60s and the small positive peak in the end of the 80s shown by the expansion time coefficient suggest that this mode is a big contributor to the 1960s/70s GISA and a small contributor to the 1980s/90s ISA. This SVD_2(SIC) makes little contribution to the 1970s/80s ISA. Similarly, in the Pacific sector, the large and wide peak during the period of 1961–1971 suggests that there existed large positive SIC anomalies in the Sea of Okhotsk during the 1960s. From 1975 to 1985 the big negative trough suggests that there existed big negative SIC anomalies in the Sea of Okhotsk. The small and narrow peak around 1988–1989 suggests there existed a short and relatively weak positive SIC anomalies in the Sea of Okhotsk.

The mainly positive SIC anomalies in both the Pacific and the Atlantic sectors and the long-term decreasing trend of the expansion time coefficient suggest that the ice extent is decreasing in the northern regions of the Barents Sea, Norwegian Sea, the Sea of Okhotsk and Chukchi Sea. Simultaneously, there is a very weak increasing trend of sea-ice extent in the BDLN region and the Bering Sea as the spatial negative anomalies in these regions are very small. This trend is also present in SVD_1(SIC).

It is worth noting that both SVD_1(SIC) and SVD_2(SIC) have the same spatial polarity in the Pacific and Atlantic sectors. While SVD_1(SIC) represents mainly a decadal mode, SVD_2(SIC) has a multi-decadal period, or more correctly, a long-term trend. These facts suggest that in the high latitudes, the sea-ice variability is dominated by both decadal and multi-decadal fluctuations.

5.2.2 SVD_2(SLP)

The spatial pattern for SVD_2(SLP) (Fig. 21, top right) shows a sandwich pattern: the moderate negative SLP anomaly cell centered over 70^0N, 60^0E is flanked by a stronger positive center of action over the Bering Sea and a weaker one over Europe. In SVD_2(SLP), the anomalies are concentrated mostly around the Pacific sector, unlike SVD_1(SLP) which shows more fluctuations around the Atlantic sector. The positive anomaly cell over the Sea of Okhotsk, Kamchatka, and the Bering Sea is so strong that its center SLP anomaly reaches up to 8 hPa. The magnitude of the anomalies is 3 hPa over the Siberia, and 2 hPa over Europe. The spatial pattern of SVD_2(SLP) resembles the corresponding EOF_2(SLP) (Fig. 4, top right). Both patterns have strong fluctuations over the Bering Sea. The correlation coefficient between SVD_2(SLP) and EOF_2(SLP) is 0.79[0.19]. The strong variability over the Pacific sector both in SVD_2(SIC) and SVD_2(SLP) suggests that SVD_2 puts more weight on the air-ice interactions in the Pacific sector.

The expansion time coefficient of SVD_2(SLP) (Fig. 21, bottom right) shows positive peaks during the periods: 1960–67, 1970–72, and 1988–89. These peaks and the positive spatial variability over the Bering Sea suggest that the climatological Aleutian low is weaker than normal during these periods, and slightly shifted towards its north-west. The negative troughs around 1969, 1976 etc. in the expansion time coefficient of SVD_2(SLP) suggest that the Aleutian Low is stronger than normal and slightly south-eastwards shifted during these periods. The short-period oscillations between the main peaks and troughs suggests that SVD_2(SLP) is associated with strong interannual variability. The power spectrum of the expansion coefficient of SVD_2(SLP) without smoothing (Fig. 22, bottom left) verifies this; the dominant period of the interannual variability is about 4 years.

5.2.3 The relationship between SVD_2(SIC) and SVD_2(SLP)

The smoothed expansion time coefficients of SVD_2(SIC) and SVD_2(SLP) (Fig. 23, top) show that on the longer timescale these two time series are roughly in phase. SVD_2(SLP) shows a weak long-term downward trend during the period 1972—1987, in addition to the strong interannual variability. SVD_2(SIC) also shows a long-term downward trend roughly over the same time as that seen in SVD_2(SLP).

The lagged-correlation coefficients between the unsmoothed expansion coefficients of SVD_2(SIC) and SVD_2(SLP) (Fig. 23, bottom) show that the maximum correlation (0.45[0.23]) occurs at zero lag. Taking into account the quick response characteristic of SLP, one can say that this mode might have some ice forcing feature. However, the next maximum correlation coefficient, 0.448, between SVD_2(SIC) and SVD_2(SLP) with SVD_2(SLP) leading by one month is quite comparable to the maximum correlation 0.45 at zero lag. This suggests that the atmospheric forcing is quite comparable to the sea-ice forcing and that the relationship between SVD_2(SIC) and SVD_2(SLP) is quite complicated, ie., the interactions are "two-way" interactions.

The patterns of the anomalous wind-stress associated with SVD_2(SIC) (Fig. 24) confirm the two-way interactions between SVD_2(SIC) and SVD_2(SLP). The spatial patterns of the anomalous wind-stress when wind-stress leads and lags SIC by 1 month are similar, and the corresponding magnitudes are comparable, which suggests that the ice-to-atmosphere forcing is comparable to the atmosphere-to-ice forcing.

The maximum vector correlation between ice and wind stress (r=0.50) when the wind stress lags the ice by 1 month is larger than the corresponding ones in the SVD1 and SVD3 modes, suggesting that the response of the atmosphere to sea ice is strongest in the second mode.

The spatial polarity of SVD_2(SIC) (Fig. 21, top left) in the Pacific sector cannot be described as the result of the overlying SLP anomalies. Near the eastern edge of the positive SLP anomaly cell centered over the Bering Sea, the associated anomalous northerly winds will help produce the large SIC extent in the Bering Sea. The western edge of this positive anomaly cell will blow anomalous south or south-westerly winds

towards the Sea of Okhotsk, and hence reduce the ice extent there. The effects of this positive SLP anomaly cell will only cause the opposite SIC anomaly pattern rather than the pattern of SVD_2(SIC) seen in the Pacific sector (Fig. 21, top left). Although it is possible that both the SIC anomalies and the atmospheric circulation fluctuations in the Pacific side are caused by some other processes, it is tempting to think that the positive SLP anomaly cell over the Bering Sea might be partially due to the downstream atmospheric response to the severe ice conditions in the Sea of Okhotsk, and partially due to the downstream atmospheric response to the heavy ice conditions in the BNGI region and later in the BDLN region. These suggestions are supported by the large-lag-time spatial correlations between $SVD_{1,2}$(SIC) and the time series of the SLP anomalies at each grid point, although this support is not perfect. Further study is necessary to understand this before any firm conclusions can be made.

5.2.4 Composite maps of SLP anomalies associated with SVD_2(SIC)

The composite maps of the SLP fluctuations are based on the unsmoothed expansion time coefficient of SVD_2(SIC). The key months chosen to represent the heavy or light ice conditions in the Sea of Okhotsk are listed in Table 5.6. There are 52 months chosen as heavy ice conditions and 48 months as light ice conditions. The large number of key months with heavy or light ice conditions is due to the wide peak and trough in the time series of the expansion coefficient of SVD_2(SIC). Due to the opposite signs of the SIC anomalies in the Sea of Okhotsk and the Bering Sea, it should be keep in mind that the trough ice and peak ice conditions are for the ice situation in the Sea of Okhotsk.

Fig. 25 (top) shows the composite maps of SLP anomalies with SLP leading heavy or light ice conditions in the Sea of Okhotsk; similarly, Fig. 25 (bottom) shows SLP lagging heavy and light ice conditions in this sea. The spatial pattern of the SLP composite map with the atmosphere leading the severe ice conditions by 2 months

	peak	peak	peak	trough	trough	trough
	Mar.54	Apr.61	Feb.66	Apr.74	Mar.81	Nov.85
	Apr.54	Mar.61	Mar.66	May 74	Apr.81	Mar.86
	May.54	May 62	Jan.67	Jan.75	Dec.81	Jan.86
	Jun.54	Apr.63	Feb.67	Feb.75	Jan.82	Feb.86
	Apr.55	May 63	Mar.67	Mar.76	Feb.82	Mar.86
	May 55	Jan.64	Apr.67	Apr.76	Jan.83	Apr.86
	Jun.55	Feb.64	May.67	May 76	Feb.83	May 86
	Jul.55	Mar.64	Oct.67	Dec.76	mar.83	Apr.88
	Apr.56	Apr.64	Nov.67	Jan.77	Apr.83	May 88
	May 56	May.64	Dec.67	Feb.77	Jan.84	Oct.91
	Jun.56	Feb.65	Jan.68	Mar.77	Feb.84	Nov.91
	Jul.56	Mar.65	Dec.68	Apr.78	Mar.84	Dec.91
	Jan.58	Apr.65	Dec.71	May.78	Apr.84	
	Jan.59	May 65	Jan.72	Apr.79	May 84	
	Feb.59	Oct.65	Feb.72	May.79	Dec.84	
	Mar.59	Nov.65	Jan.90	Jun.79	Jan.85	
	Apr.59	Dec.65		Jan.81	Feb.85	
	May 59	Jan.66		Feb.81	Mar.85	
total	52 months for peak ice			48 months for light ice		

Table 5.6: The key months with heavy or light ice conditions in the Sea of Okhotsk and the BNGI region based on the unsmoothed expansion coefficient of SVD_2(SIC).

(25, top left) is quite similar to the spatial structure of SVD_2(SLP), with each having a strong positive anomaly cell over the Bering Sea. The composite anomaly map with SLP leading the light ice conditions by 2 months (Fig. 25, top right) is just the same as the SVD_2(SLP) spatial anomalies but with opposite signs.

The amplitude of the atmospheric fluctuations over the Bering Sea 2 months before heavy ice conditions in the Sea of Okhotsk is about 5 hPa. The corresponding amplitude with the atmosphere lagging the heavy ice conditions by 2 months in the Sea of Okhotsk is still 5 hPa. However, in the case of light ice conditions in the Sea of Okhotsk, the amplitude of the atmospheric fluctuation changes considerably, from -8 hPa at 2 months before the light ice to -2 hPa at 2 months after the light ice. This suggests that the response of the atmosphere to heavy ice conditions in the Sea of Okhotsk is much stronger than in the case of light ice conditions.

5.2.5 Correlation analyses based on SVD_2(SIC)

Similar to the correlation analysis based on SVD_1(SIC), the spatial maps of correlations are calculated between the time series of the SLP monthly anomalies at each grid point and the time series of expansion coefficient SVD_2(SIC). A positive correlation implies that when the time series of SVD_2(SIC) is positive, i.e., there are large ice-concentrations in the Sea of Okhotsk and the BNGI region, the sign of the corresponding SLP anomalies also tends to be positive.

The spatial correlations with SLP leading the heavy ice conditions by 1 year in the Sea of Okhotsk and BNGI region (Fig. 26, top left) shows that significant positive centres of action exist in the Bering Sea and over Greenland. This suggests that the positive SIC anomalies in the Sea of Okhotsk (the Greenland-Iceland Seas) might be related to the weakening of the Aleutian Low (Iceland Low) one year earlier.

The spatial maps of the lagged-correlations with long-term lags are shown in Fig. 26 and Fig. 27. With sea-ice leading atmosphere up to several years, significant positive correlations still exist, suggesting that the heavy ice conditions in the Sea of Okhotsk and in the BNGI region can affect the atmosphere for several years. This

suggests that the severe sea-ice conditions in the Sea of Okhotsk and the BNGI region might result in higher than normal SLP over the Bering Sea and Greenland, if it is not the case that both SLP and SIC anomalies are due to some other processes. The model results by Honda *et al.* (1996) suggest that it is unlikely that both of these climate variables are driven by some other unknown process. They found that a cold anticyclone is likely to develop over the Sea of Okhotsk (but not over the Bering Sea) in the heavy ice case. It is possible that the ice can influence the atmosphere by isolating the ocean from the atmosphere, reducing the heat loss from ocean to atmosphere which results in cooler air temperatures and hence higher SLP.

The higher than normal SLP in the Bering Sea may result in less storminess and precipitation, and hence reduce the river run-off into the western Arctic. The reduced river run-off might destabilize the western Arctic sea water, resulting in an overturn of deep warm and salty water and hence a reduction in the ice formation process. Negative SIC anomalies in the western Arctic might follow from anomalous low river run-off, if the latter anomalies can last for several continuous years. The significant positive correlation (Figs. 26 and 27) with SIC leading SLP up to 7 years suggests that it is possible for the low river runoff signal to last for several years in a row.

5.3 The third mode

The third SVD mode (Fig. 28) explains only 7.4% of the squared covariance. It is not as important as the first and second modes. Besides, the third mode is not well separated from the higher modes (not shown). Thus in this section, SVD_3 will be discussed only very briefly.

5.3.1 SVD_3(SIC)

The spatial anomalies of SVD_3(SIC) (Fig. 28, top left) have mainly a one-signed structure in the Pacific Sector. Thus the anomalies of SIC in the Sea of Okhotsk have the same sign as those in the Bering Sea, with the latter having a relatively larger ampli-

tude. In the Atlantic sector, the SIC anomalies in the Gulf of St. Lawrence, the Greenland Sea and the Norwegian Sea all have the same sign as those in the Pacific Sector. The fluctuations of SIC in the Barents Sea are of opposite sign. SVD_3(SIC) shows the largest fluctuations in the Bering Sea and the Gulf of St. Lawrence. SVD_3(SIC) shows no significant similarity with EOF_3(SIC). The correlation coefficient between SVD_3(SIC) and EOF_3(SIC) is 0.06[0.3]. The spatial pattern of SVD_3(SIC) closely resembles EOF_2(SIC). The correlation coefficient between EOF_2(SIC) and SVD_3(SIC) is 0.65[0.32].

The expansion time coefficient of SVD_3(SIC) (Fig. 28, bottom left) reveals generally negative values before 1976 and in 1991, and general positive values during the period of 1976–1990. The rapid increase around 1976 is consistent with the well-documented "climatic jump" in the North Pacific (Knox, JL et al. 1988). The oscillations within the narrow troughs and within the narrow peaks suggest that this mode is dominated by interannual variability besides the long-term changes. The power spectrum (Fig. 29, top left) of the unsmoothed expansion time coefficient of SVD_3(SIC) reveals that besides the annual peaks, a significant interannual oscillation with a period of around 7 years and a long-term trend co-exist.

5.3.2 SVD_3(SLP)

The SVD_3(SLP) spatial pattern (Fig. 28, top right) reveals a negative SLP anomaly cell around 40^0E, 60^0N, with an amplitude of -5 hPa. This center of action extends far towards the east and west. The amplitude of the SLP anomalies is -2 hPa over Eastern Siberia, and -1 hPa over Greenland. The general pattern of SVD_3(SLP) is similar to the variability shown in EOF_3(SLP), but with opposite sign. The correlation between EOF_3(SLP) and SVD_3(SLP) is -0.57[-0.15].

The expansion time coefficient of SVD_3(SLP) (Fig. 28, bottom right) shows a quick alternation between peaks and troughs, suggesting that this mode has a strong interannual signal. The power spectrum of the unsmoothed SVD_3(SLP) expansion time coefficient (Fig. 29, bottom left) shows that this SVD_3(SLP) has a peak at

around 5 years.

5.3.3 The relationship between SVD_3(SIC) and SVD_3(SLP)

As was done for SVD_1 and SVD_2, the expansion time coefficients for both SVD_3(SIC) and SVD_3(SLP) are shown together in Fig. 30 for comparison. From this figure, one can see that SVD_3(SLP) generally leads SVD_3(SIC) by several months, which suggests that this mode represents an atmosphere-to-ice forcing. The lagged-correlations between the expansion time coefficients of SVD_3(SIC) and SVD_3(SLP) reach their maximum value of 0.53 [0.19] when SVD_3(SLP) leads by one month (Fig. 30, bottom). This confirms the atmospheric forcing hypothesis.

The largest SIC anomalies of SVD_3(SIC), i.e., the ones in the Bering Sea and in the Gulf of St. Lawrence, can be described as the result of the overlying SLP anomalies. The negative SLP anomaly over eastern Siberia (Fig. 28, top right) results in anomalous warm southerly or south-westerly winds towards the Bering Sea, which reduce the heat loss from the ocean to the atmosphere and hence reduce the ice extent there. Besides, this anomalous southerly or south-westerly winds help drive the ice edge towards the coastline. Hence, the negative SIC anomalies in the Bering Sea can be described as the result of the overlying atmospheric circulation fluctuations. The negative SIC anomalies at the Gulf of St. Lawrence can be explained as the result of the positive SLP anomaly cell around 60^0W, 50^0N. The wind associated with this cell will carry warm oceanic air towards the Gulf, and reduce the ice extent there.

5.4 The Monte Carlo significance test

The robustness of the SVD results is assessed by testing the significance of the square covariance (SC) associated with each mode using a Monte Carlo approach. The detailed procedure for this test is described in chapter 3, section 3.4. The results of the significance test (Fig. 31) show that all these three leading modes are significant at the 95% significance level.

Chapter 6

Discussion and conclusions

In this thesis, the SVD as well as the EOF analysis methods are used to investigate the interactions between the Arctic SIC anomalies and the overlying atmospheric circulation fluctuations. The EOF analysis method is mainly used to identify independent patterns in the SIC and SLP variability. The SVD analysis method is mainly used to study the covariability between the two fields. Based on the results of the SVD analysis, composite anomaly maps and spatial lagged-correlation maps are also used to shed more light on the relationships between the atmosphere and the sea ice.

The three leading EOF modes of variability of the individual SIC and SLP fields northwards 45^0N have been identified and briefly analyzed. The three leading modes of SIC variability account for only 28.4% of the total monthly SIC variance. A larger percentage of the total SLP variance, 52.4% is accounted for by the three leading modes of atmospheric variability. It is interesting to note that both decompositions leave a relatively large fraction of the total variance unexplained. As earlier mentioned, the relatively less variability accounted for by the leading three EOF modes of SIC may largely be due to the strong annual cycle that was not cleanly removed in this study.

The principal features which characterize the first EOF mode for both SIC and SLP are found again in the first SVD mode of the coupled fields. SVD_1(SIC) has a decadal period, which confirms the existence of the 1970s/80s ISA and the 1980s/90s

ISA events, besides the well known 1960s/70s GISA event. SVD_1(SIC), like EOF_1(SIC), reveals a strong dipole structure of SIC anomalies in the Atlantic between the BNGI region and the BDLN region and a weak dipole structure in the Pacific between the Sea of Okhotsk and the Bering Sea. This suggests that, associated with the 1960s/70s GISA, the 1970s/80s ISA, and the 1980s/90s ISA in the Atlantic sector, similar, though much weaker events occurred in the Pacific sector. These simultaneous dipole structures may affect the thermal gradient between the subpolar region, i.e., around the 60°N latitude circle, and the Arctic region through air-ice-ocean interactions and hence affect the Polar Cell circulation which is a thermally driven cell.

SVD_1(SLP), similar to EOF_1(SLP), reveals mainly interannual oscillations and a relatively weak longer-period oscillation, which corresponds well to the long period oscillation of the SIC anomalies. SVD_1(SLP) picks up a positive SLP anomaly over the central Arctic, the European sub-Arctic, especially Greenland and the northern North Atlantic areas, and a negative SLP anomaly over the western Europe. SVD_1(SLP) is similar to the NAO pattern.

The first coupled SVD mode puts more weight on the covariability of the air-ice system over the Atlantic sector than on that over the Pacific sector, so it can be said that the first mode is mainly an Atlantic mode.

By comparing the spatial patterns of SVD_1(SIC) and SVD_1(SLP), it seems that the spatial variability of SVD_1(SIC) can be described as the result of local or remote fluctuations in the atmospheric circulation 2 months earlier. This suggests that this mode is dominated by an atmospheric forcing of sea ice. The lagged correlation analyses confirm this hypothesis.

The composite analyses suggest that for the 1960s/70s GISA event, the positive SIC anomalies in the BNGI region are largely due to the abnormally large amount of sea ice and fresh water export from the Arctic to the BNGI region, which coincided with a strong negative NAO pattern. For the 1970s/80s ISA, the positive SIC anomalies in the BDLN region are largely due to local ice formation processes, which are strengthened by anomalous northerly winds over the BDLN region, and partially

by the advection of ice and fresh water from upstream (the Greenland Sea). The composite map (Fig. 12 top right) show 1970s/80s ISA is also related to a negative NAO pattern. For the 1980s/90s ISA, the positive SIC anomalies in the BDLN region are partially due to local ice formation processes, strengthened by the anomalous northerly winds over the BDLN region, and partially by the ice and fresh water export from Arctic through the Nares Strait and the CAA.

The correlation maps between SVD_1(SIC) and the atmospheric grid point anomalies show the existence of significant correlations when the atmosphere lags the SIC by up to several years. The short timescale (less than 6-months) positive feedback between SIC and SLP and the long memory of the SIC contribute to those long-lag correlations.

SVD_2(SIC) oscillates with a long period which is not well resolved due to the shortness of the data record. Like SVD_1(SIC), SVD_2(SIC) has sea-saw structures in the Atlantic and the Pacific sector, with more variability in the Sea of Okhotsk. SVD_2(SIC) also picks up signals of the 1960s/70s GISA and 1980s/90s ISA events. SVD_2(SLP) reveals a general deepening or weakening of the climatological Aleutian Low. Because both SVD_2(SIC) and SVD_2(SLP) have stronger variability in the Pacific sector, SVD_2 can be seen as a Pacific mode.

In SVD_2, the SIC and the atmosphere are mutually affected, but the SIC as a driving component is slightly stronger than the atmospheric one. The correlation maps between SVD_2(SIC) and the SLP grid anomalies suggest that the response of SLP over the Bering Sea to the positive SIC anomalies in the Sea of Okhotsk is much larger than the response of SLP to the negative SIC anomalies in the same region.

The existence of the decadal signal in the SIC monthly anomaly data might be related to the following speculative factors:

1) The short-timescale positive feedback between SIC and SLP and the long memory of the SIC anomalies. These may cause the extension of heavy ice conditions (if once this anomalies exist) resulting in high SLP for up to several years, as suggested by the spatial lagged correlations.

2). The thermal gradient affected (mainly through the heat exchange) by the dipole structure of the SIC variability in both the Atlantic and the Pacific sectors (present in both SVD_1(SIC) and SVD_2(SIC)). This may affect the Polar Cell Circulation and hence affect the net meridional transport in high latitudes.

The mechanism responsible for the decadal oscillation in the SIC anomalies is worthy of further study. The exchange of heat between the air and the ocean on the timescale of the SIC variability may be the key factor in investigating the influence of the SIC anomalies on the atmosphere. In addition, the relationship between SIC and a more realistic wind-stress field (which might be obtained from the daily SLP data) needs further investigation.

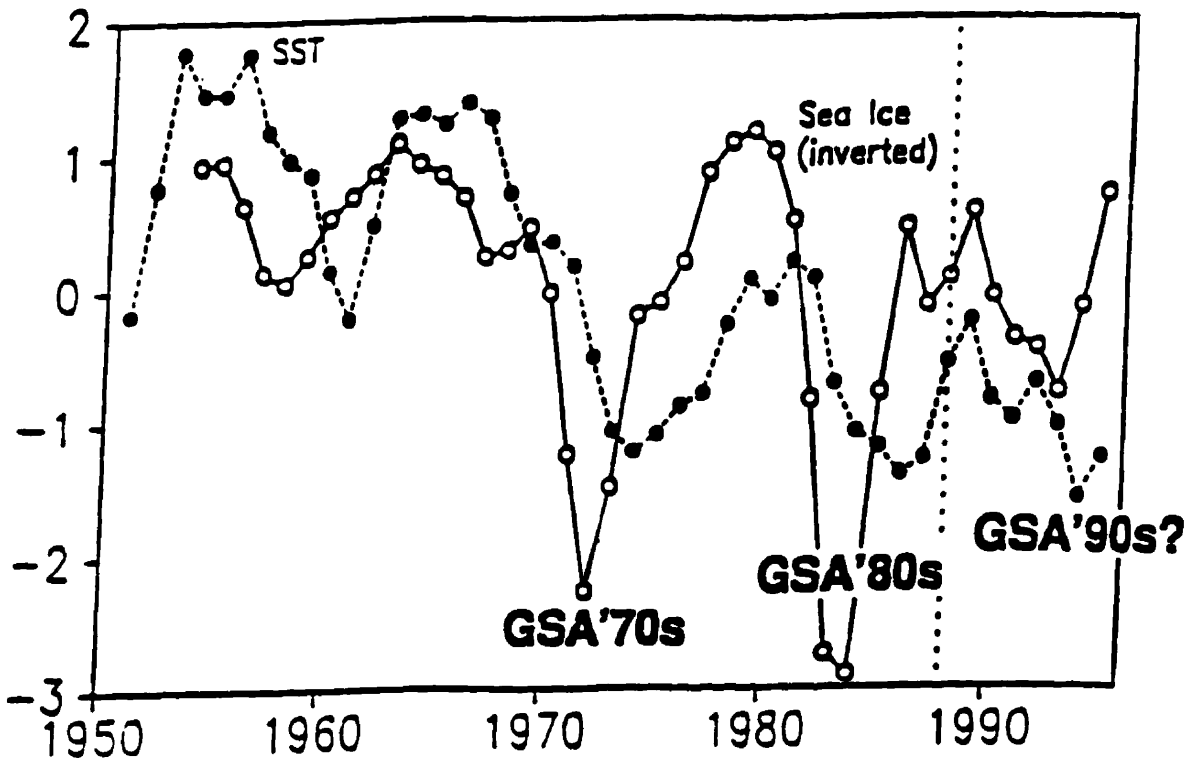

Figure 1: Standardized anomalies of winter sea ice extent east of Newfoundland (46°-54°N, 55°-45°W, open circles) and SST in the subpolar North Atlantic (50°-60°N, solid circles) (modified by Belkin et al. (1998) from Fig.3 of Deser and Timlin (1996)). The vertical dashed line shows the last year of data presented in Deser and Blackmon (1993). The ice index has been inverted to expose association between high ice extent and low SST.

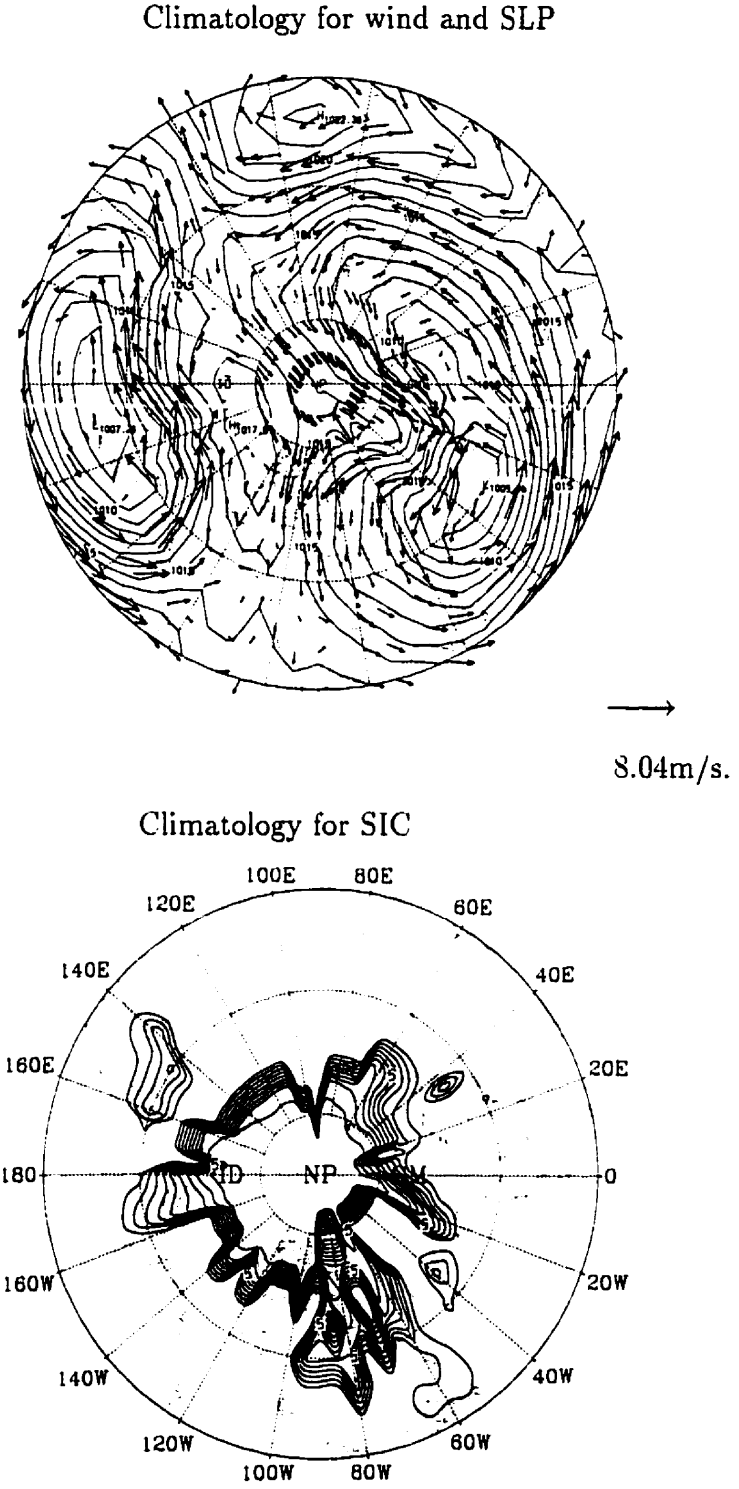

Figure 2: Top: climatology of geostrophic surface wind vector and sea-level pressure (SLP); Bottom: climatology of sea-ice concentration (SIC).

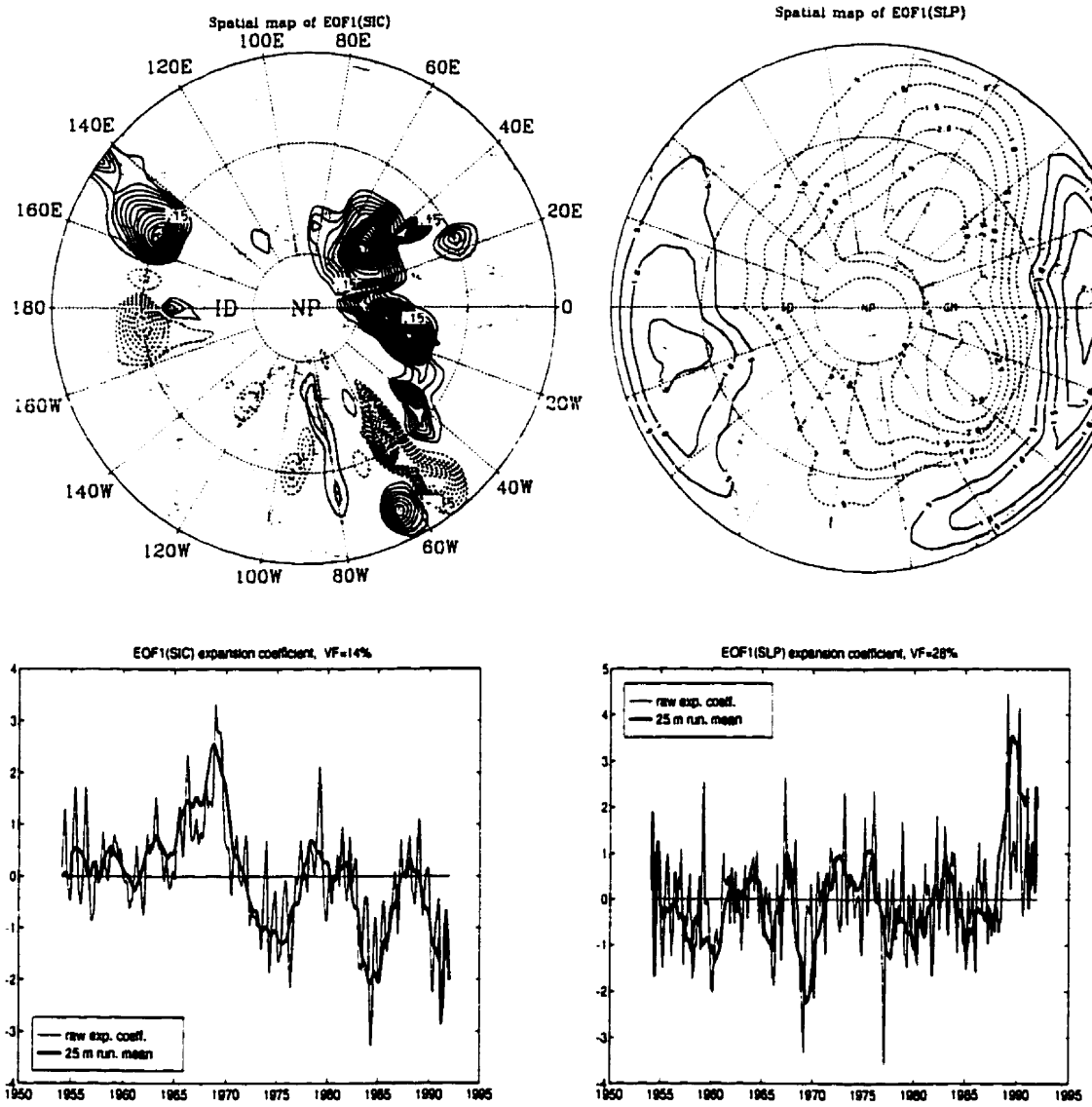

Figure 3: Spatial patterns and expansion time coefficients of EOF_1(SIC) and EOF_1(SLP). The spatial patterns are presented as homogeneous regression maps. Contour interval is 0.5 hPa for SLP, 0.03 for SIC. Positive contours are solid, negative contours are dashed. In the top two figures, the latitude circles shown are for 45^0N, 60^0N and 80^0N. The amplitudes of the expansion time coefficients are normalized by the corresponding standard deviations. The heavy lines in both expansion coefficient maps are 25-month-running means, the light lines are the unsmoothed ones.

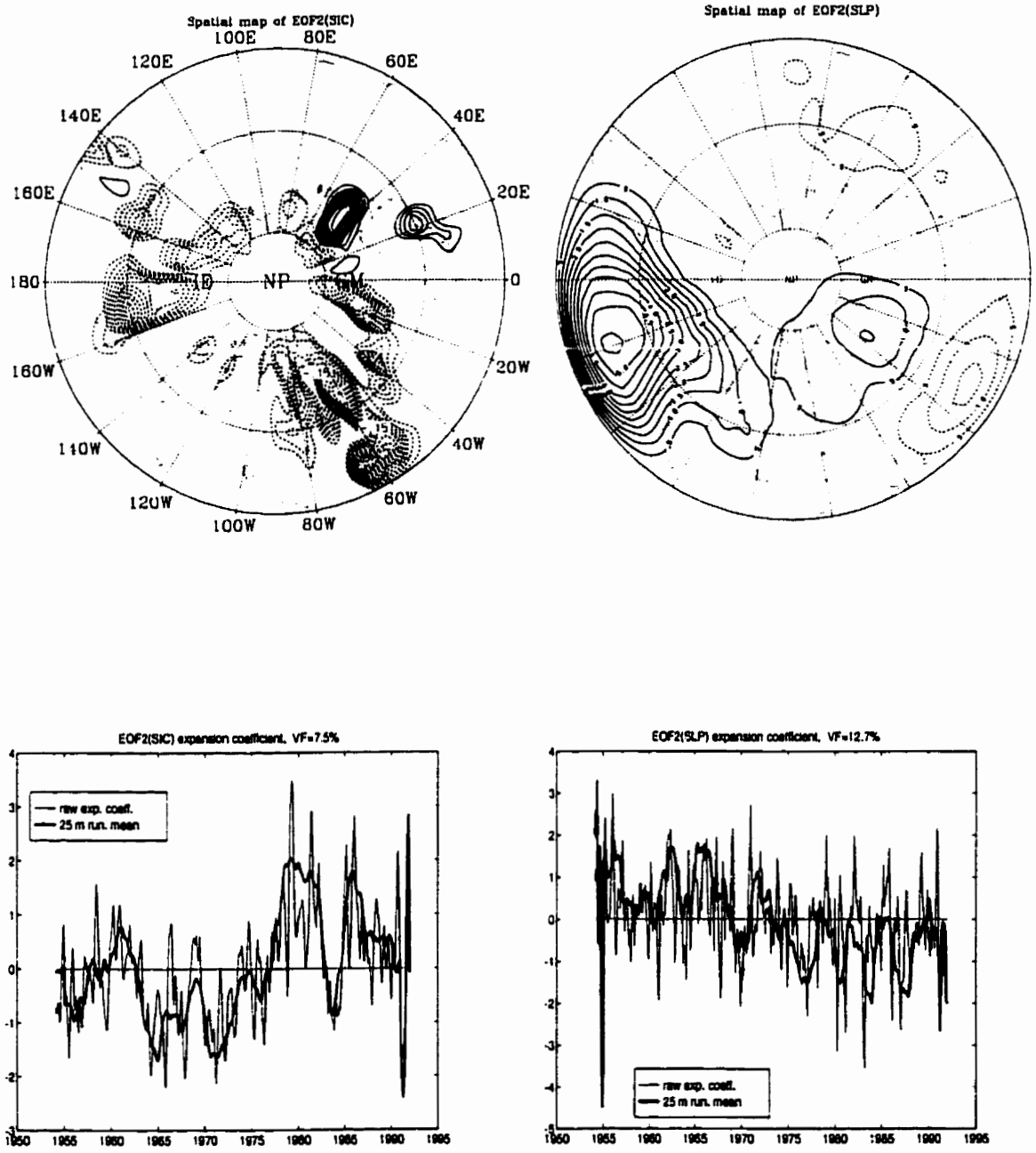

Figure 4: Spatial patterns and expansion time coefficients of EOF_2(SIC) and EOF_2(SLP). Conventions are as in Fig. 3.

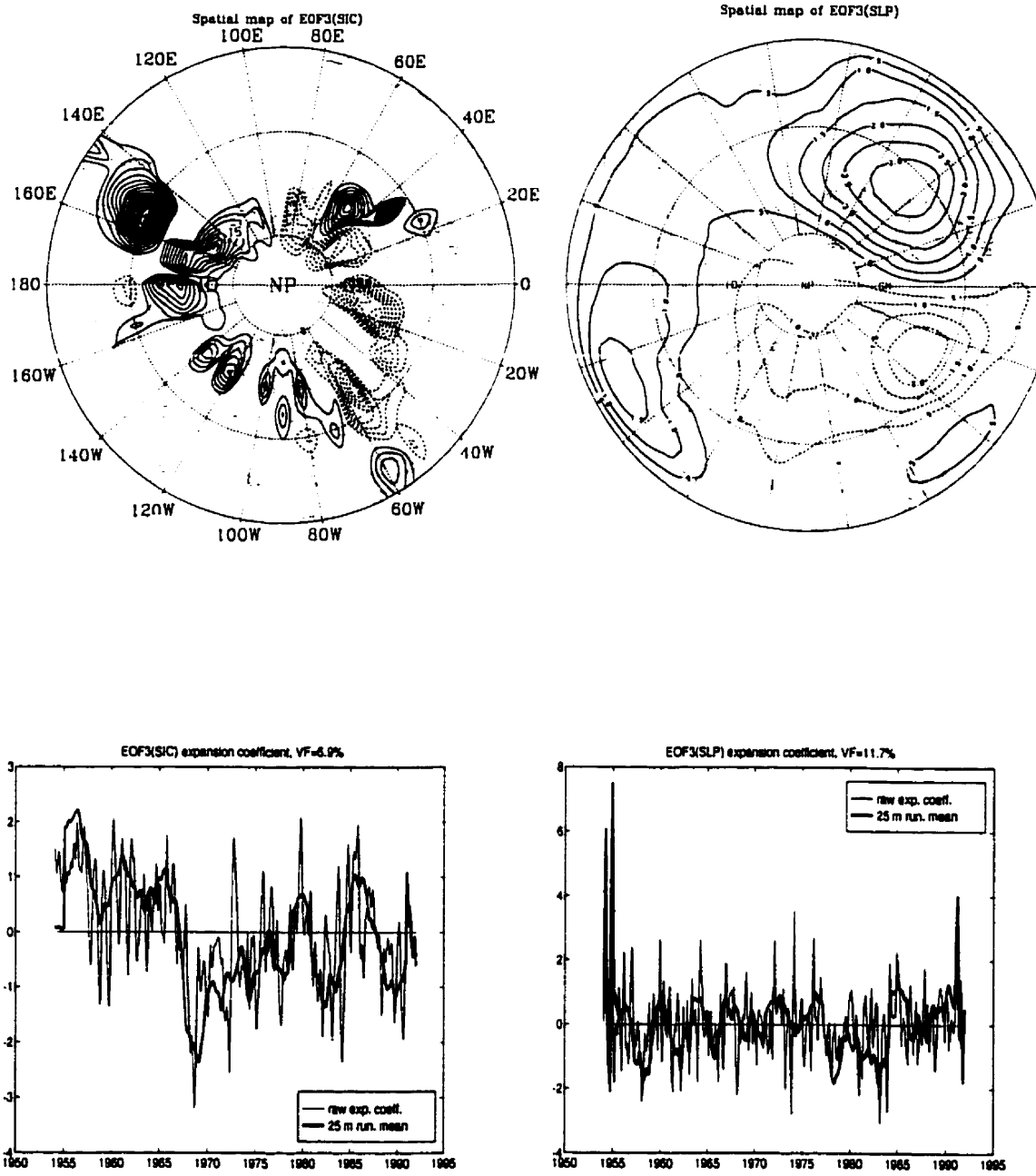

Figure 5: Spatial patterns and expansion time coefficients of EOF_3(SIC) and EOF_3(SLP). Conventions are as in Fig. 3.

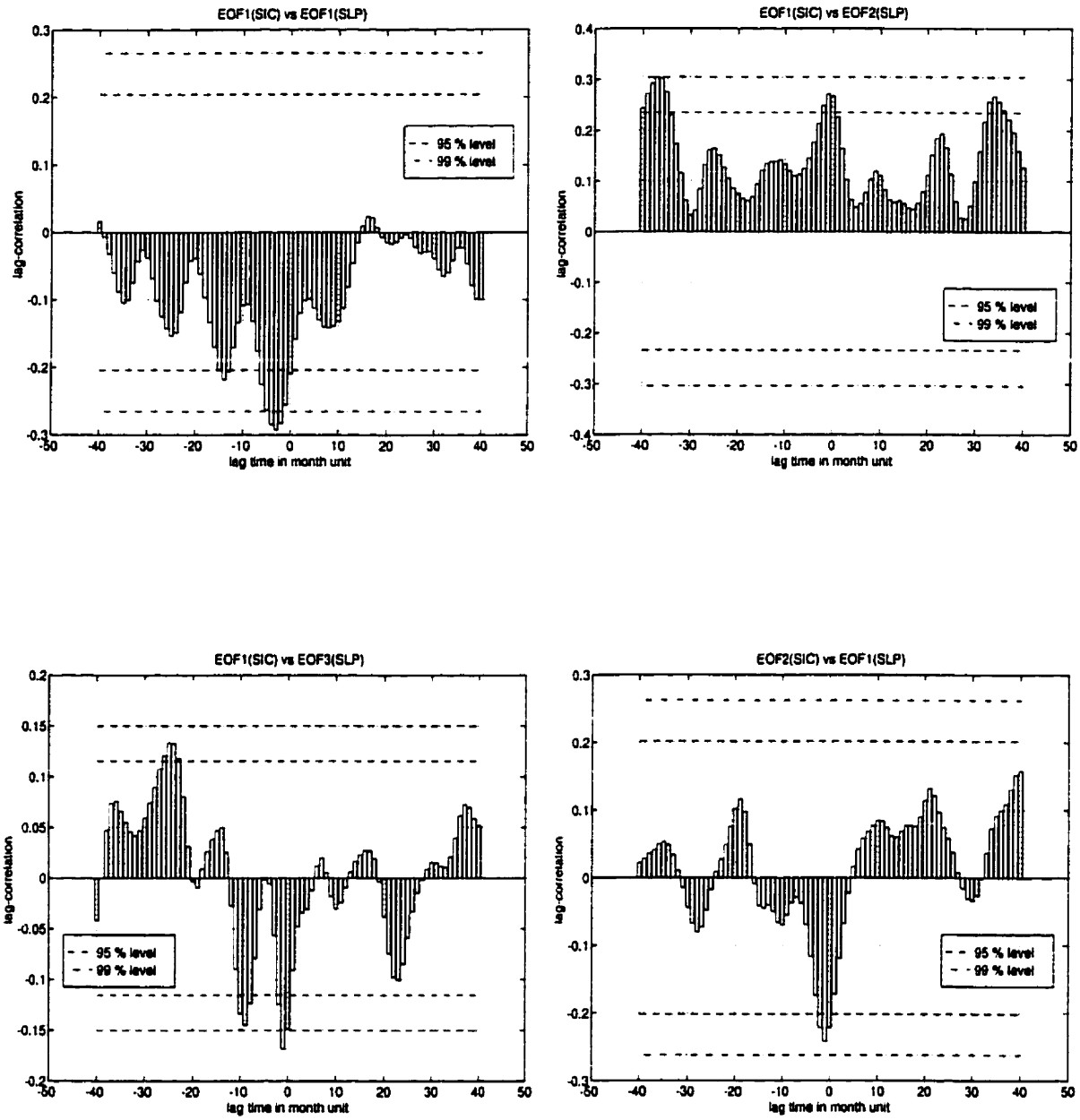

Figure 6: Lagged correlations between EOF_1(SIC) and the first three leading EOF modes of SLP, and between EOF_2(SIC) and EOF_1(SLP). SLP leads for negative lags. Lags are in months. The lagged correlations are based on the unsmoothed expansion time coefficients.

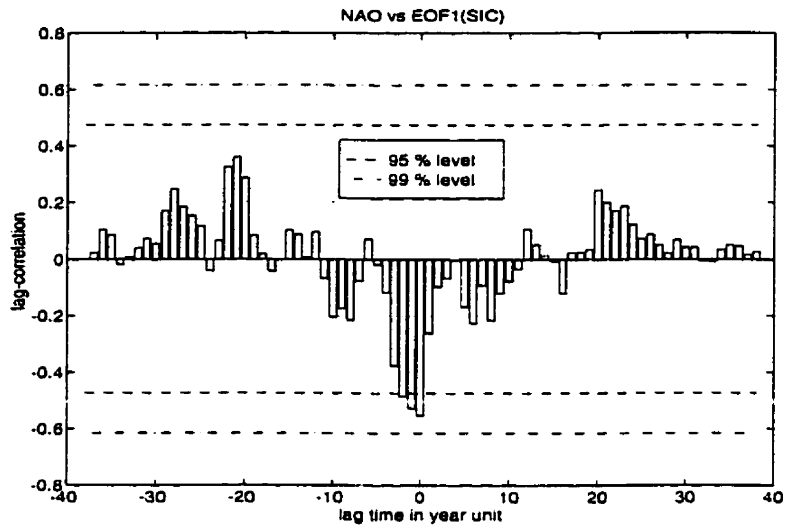

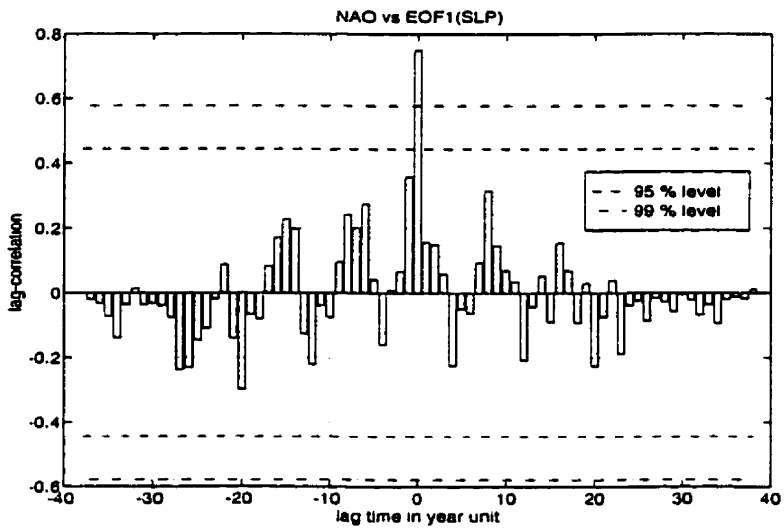

Figure 7: Lagged correlations between the NAO index and EOF_1(SIC) and EOF_1(SLP). NAO leads for negative lags. Lags are in years. The lagged correlations are based on the winter averaged values of the expansion time coefficients of the first EOF modes of SLP and SIC.

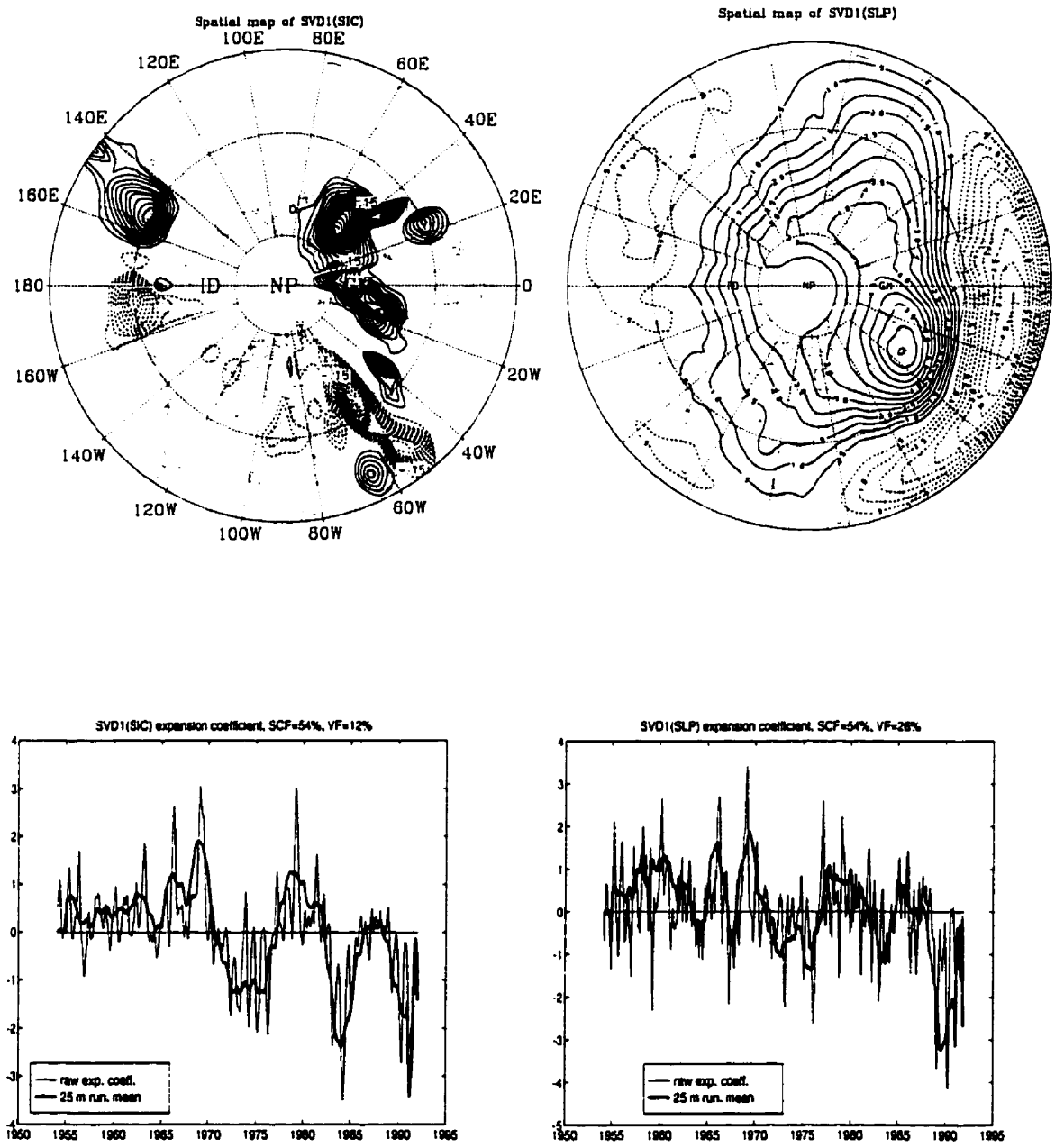

Figure 8: Spatial patterns and expansion time coefficients of the first coupled SVD modes between SIC and SLP. The left two are for SVD_1(SIC) and the right two are for SVD_1(SLP). Conventions are as in Fig. 3

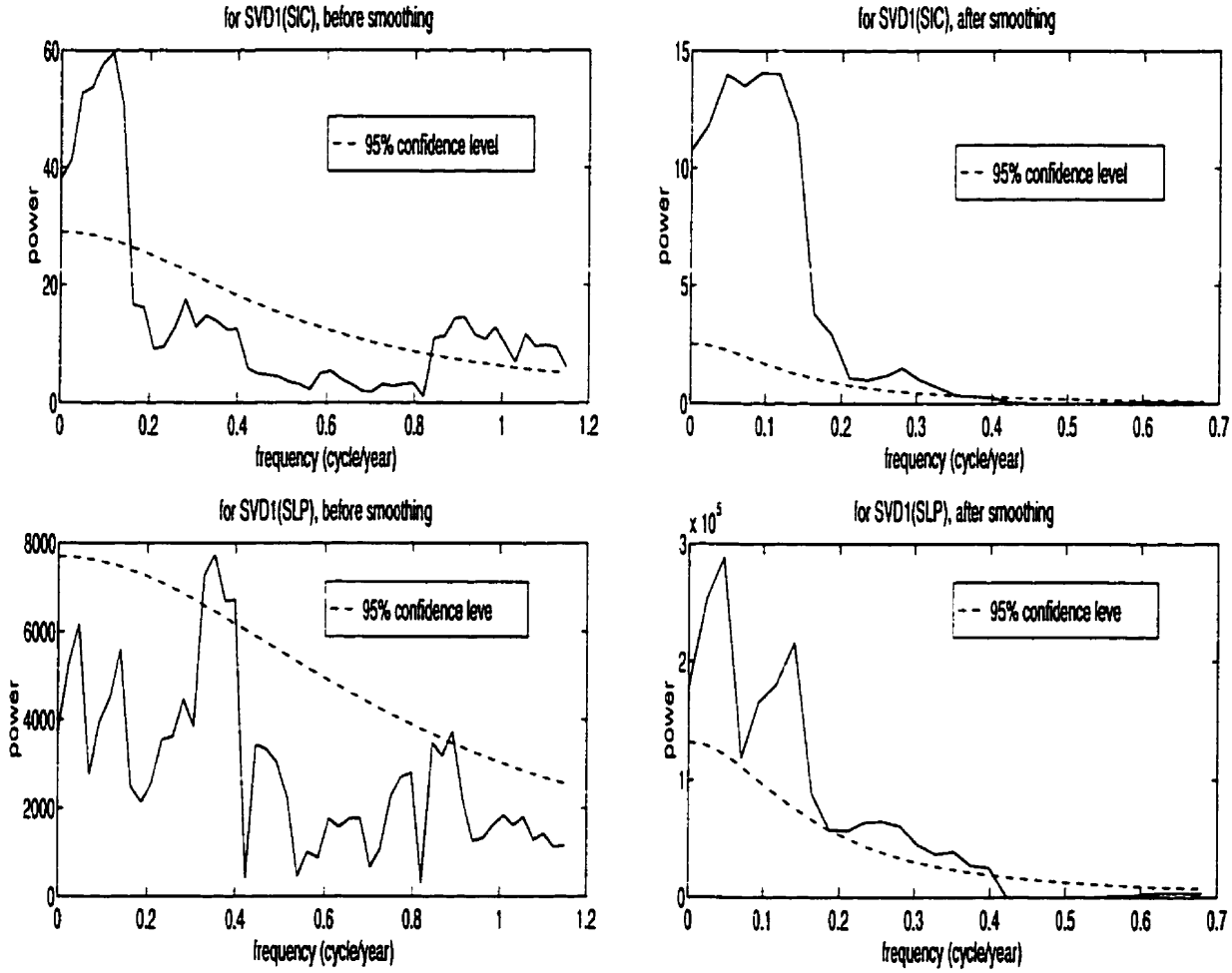

Figure 9: Power spectra of the expansion time coefficients of SVD_1(SIC) and SVD_1(SLP). Top two are for SVD_1(SIC), bottom two are for SVD_1(SLP). Left two are before smoothing, right two are after smoothing.

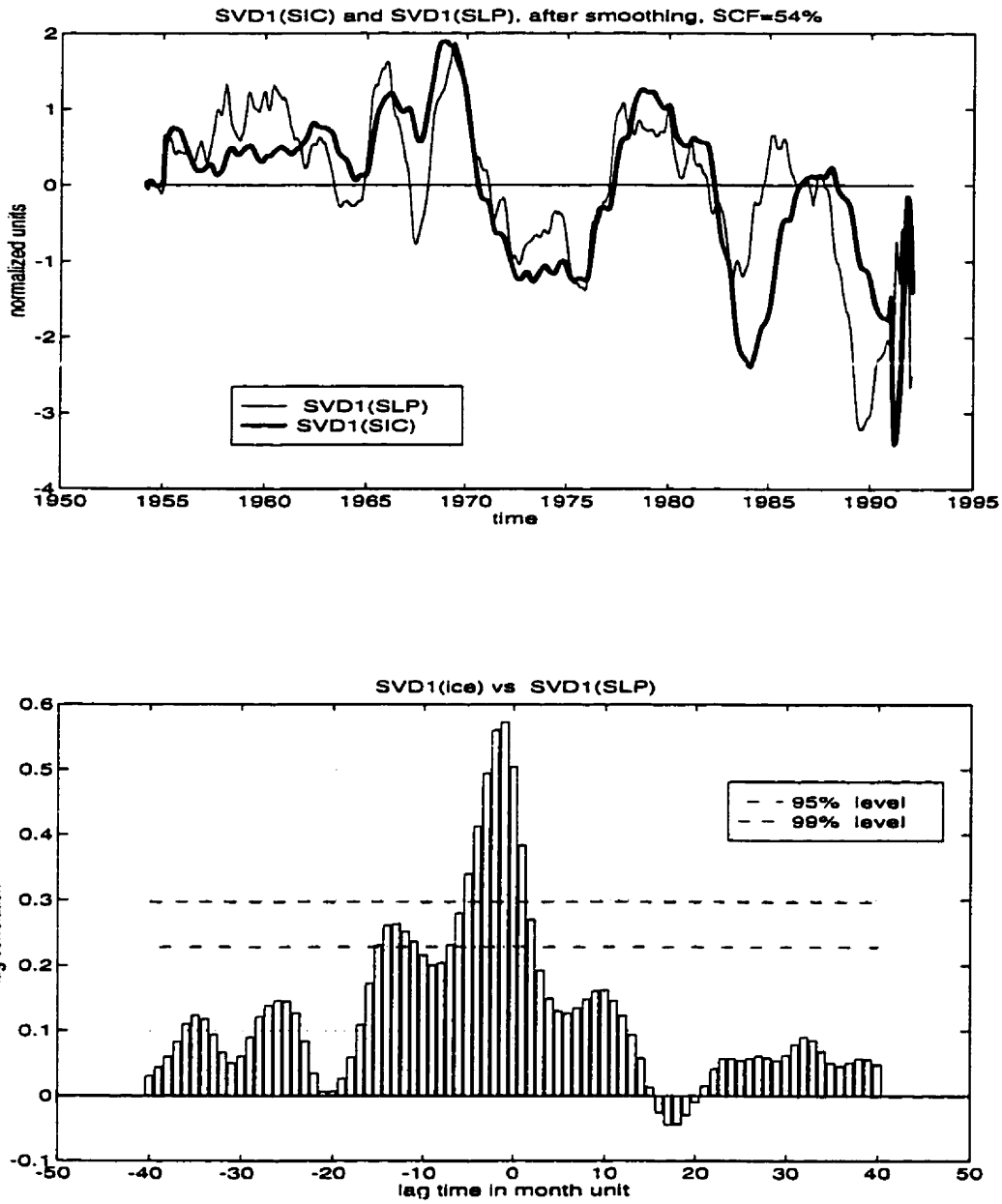

Figure 10: Top: smoothed expansion coefficients for SVD_1(SIC) and SVD_1(SLP); their amplitudes are normalized by the corresponding standard deviation. The solid line is for SVD_1(SIC), the light line is for SVD_1(SLP). Bottom: Correlation functions between the unsmoothed expansion coefficient of SVD_1(SIC) and SVD_1(SLP); positive lag means the SIC leads.

SVD1(SIC) and wind stress one month earlier

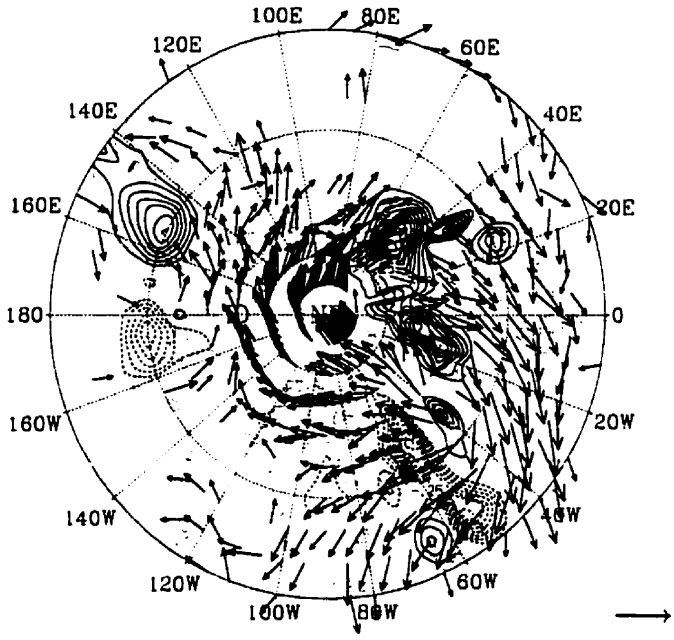

SVD1(SIC) and wind stress one month later

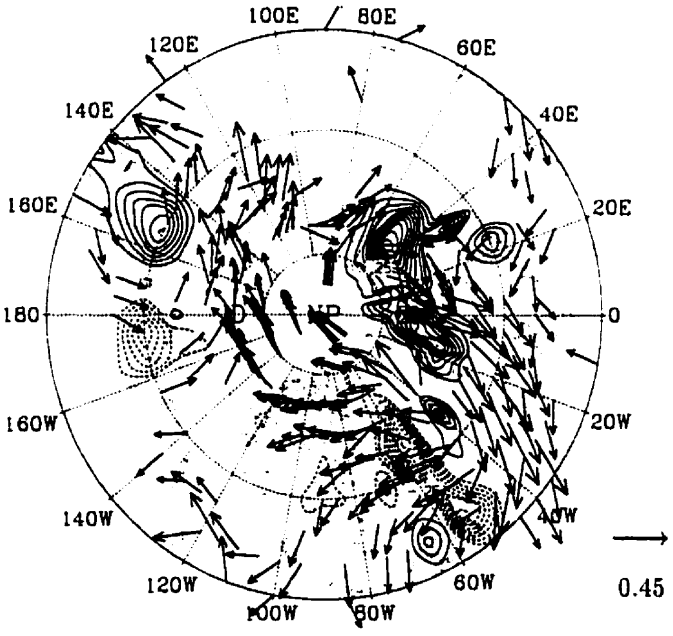

Figure 11: Estimated wind stress associated with SVD_1(SIC). The u- and v-components of the wind anomalies are correlated with SVD_1(SIC) at each grid point. Wind stress is estimated from the wind by turning vector wind to its left by 20^0. "Vector correlations" are obtained by plotting the components in vectorial form. The SVD_1(SIC) pattern is the same as in top left of Fig.8. The latitude circles shown are for 45^0N, 60^0N and 80^0N. The lag relationships between ice and wind stress are shown at the top of each map.

Composite SLP and wind 2 months earlier,
1960s/70s GISA(trough)

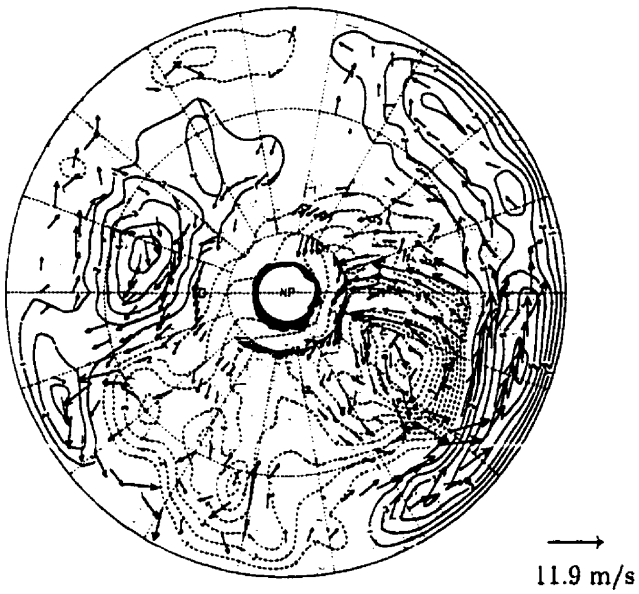

Composite SLP and wind 2 months earlier
1960s/70s GISA (peak)

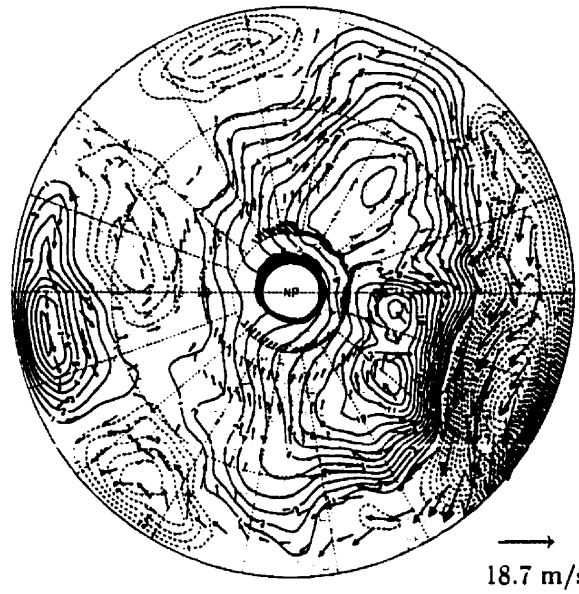

Composite SLP and wind 2 months later,
1960s/70s GISA(trough)

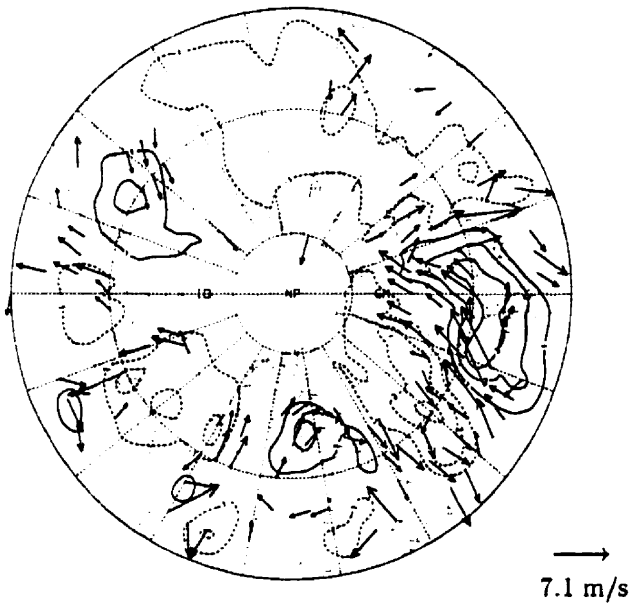

Composite SLP and wind 2 months later
1960s/70s GISA (peak)

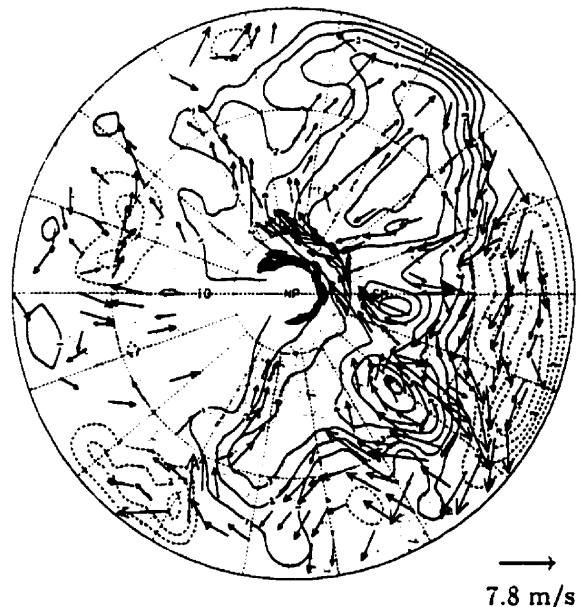

Figure 12: Composite maps of SLP and wind anomalies during the 1960s/70s GISA. Left-top: with SLP and winds leading the trough-ice conditions by 2 months in the Barents Sea, Norwegian Sea, Greenland Sea and Iceland Sea (BNGI) region. Left-bottom: with SLP and winds lagging by 2 months the trough-ice conditions in the BNGI region. Right-top: with SLP and winds leading by 2 months the heavy-ice conditions in the BNGI region. Right-bottom: with SLP and winds lagging by 2 months the light-ice conditions in the BNGI region.

Composite SLP and wind 2 months earlier,
1970s/80s ISA(trough)

Composite SLP and wind 2 months earlier
1970s/80s ISA (peak)

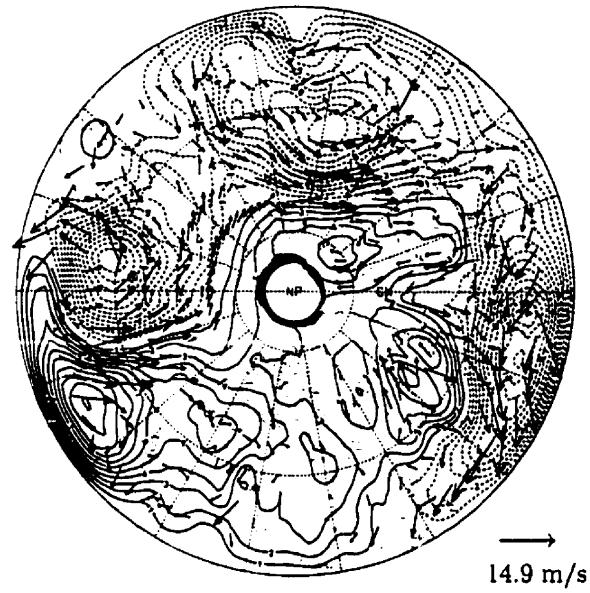

Composite SLP and wind 2 months later,
1970s/80s ISA(trough)

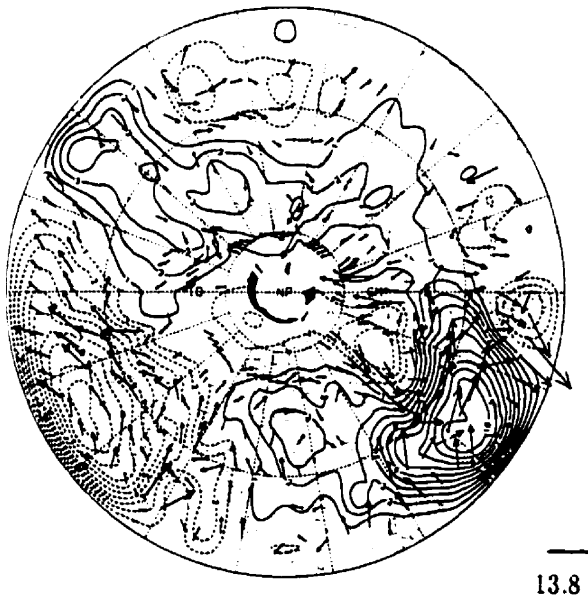

Composite SLP and wind 2 months later
1970s/80s ISA (peak)

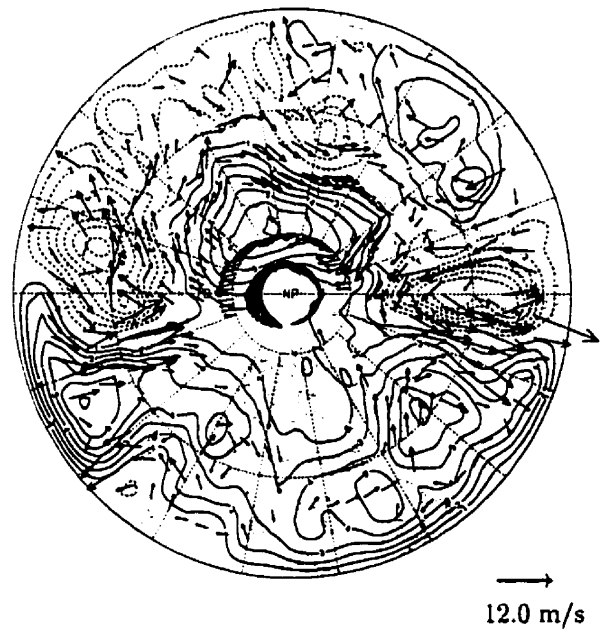

Figure 13: Composite maps of SLP and wind anomalies during the 1970s/80s ISA event. Conventions are as in Fig. 12.

Composite SLP and wind 2 months earlier,
1980s/90s ISA(trough)

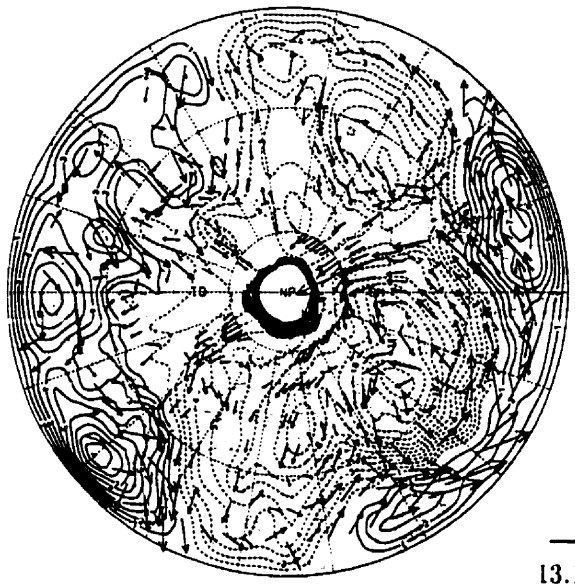

13.1 m/s

Composite SLP and wind 2 months earlier
1980s/90s ISA (peak)

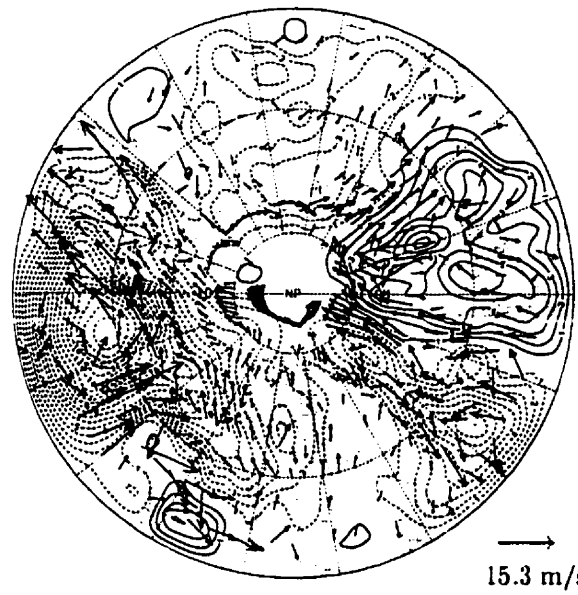

15.3 m/s

Composite SLP and wind 2 months later,
1980s/90s ISA(trough)

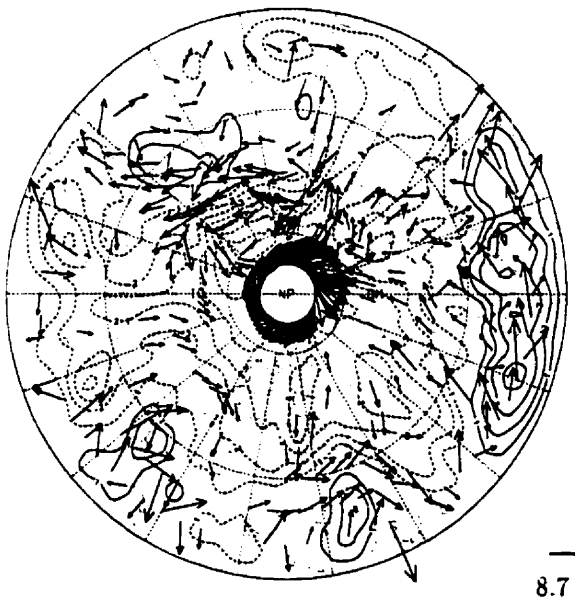

8.7 m/s

Composite SLP and wind 2 months later
1980s/90s ISA (peak)

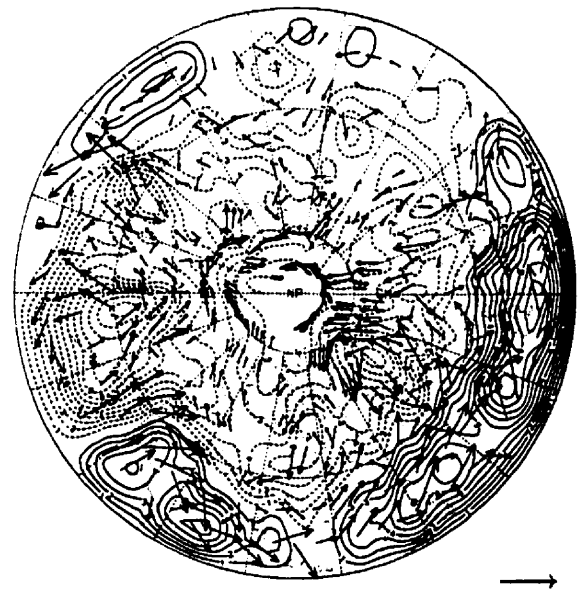

12.8 m/s

Figure 14: Composite maps of SLP and wind anomalies during the 1980s/90s ISA event. Conventions are as in Fig. 12.

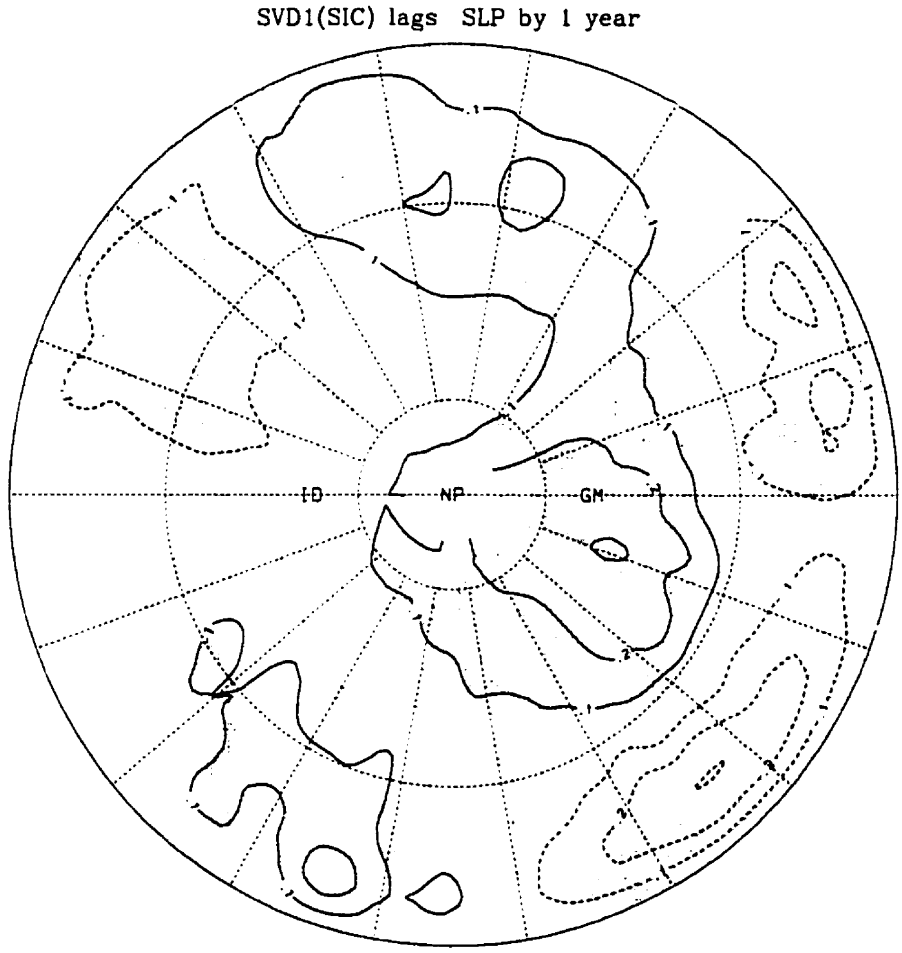

Figure 15: Spatial map of temporal lagged-correlation coefficients between the SVD_1(SIC) expansion coefficient and the time series of the SLP anomalies at each grid point, with atmosphere leading SVD_1(SIC) by 1 year. The latitude circles shown are for 45^0N, 60^0N and 80^0N, the dotted line cross the N.P is the dateline. The shaded parts represent regions where correlations are significant at 95% level.

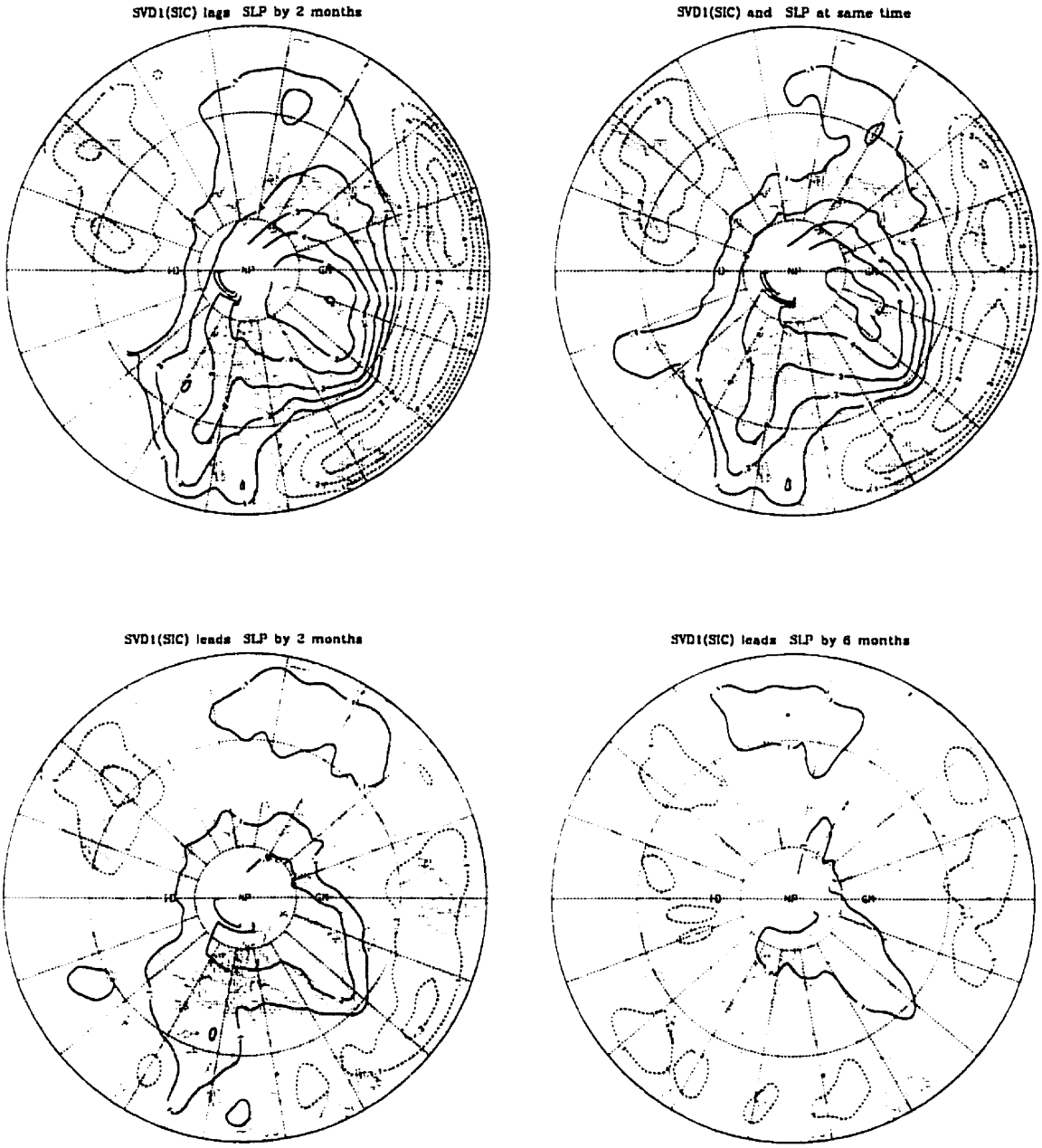

Figure 16: Spatial maps of lagged-correlations between the SVD_1(SIC) expansion coefficient and the time series of SLP anomalies at each grid point on short timescales. The lag-relationship is shown on the top of each map. Conventions are as in Fig. 15.

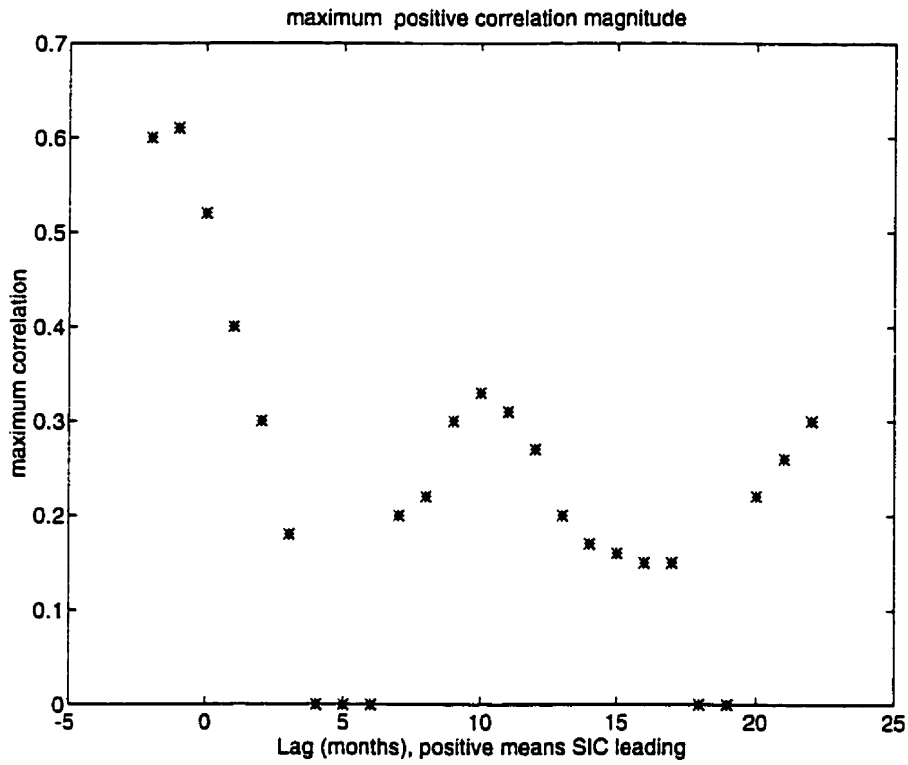

Figure 17: Relationship between the maximum positive lagged-correlation coefficient at a specific lag and the length of the lag. The maximum lagged-correlation coefficient at one specific lag is the largest one over the whole spatial domain.

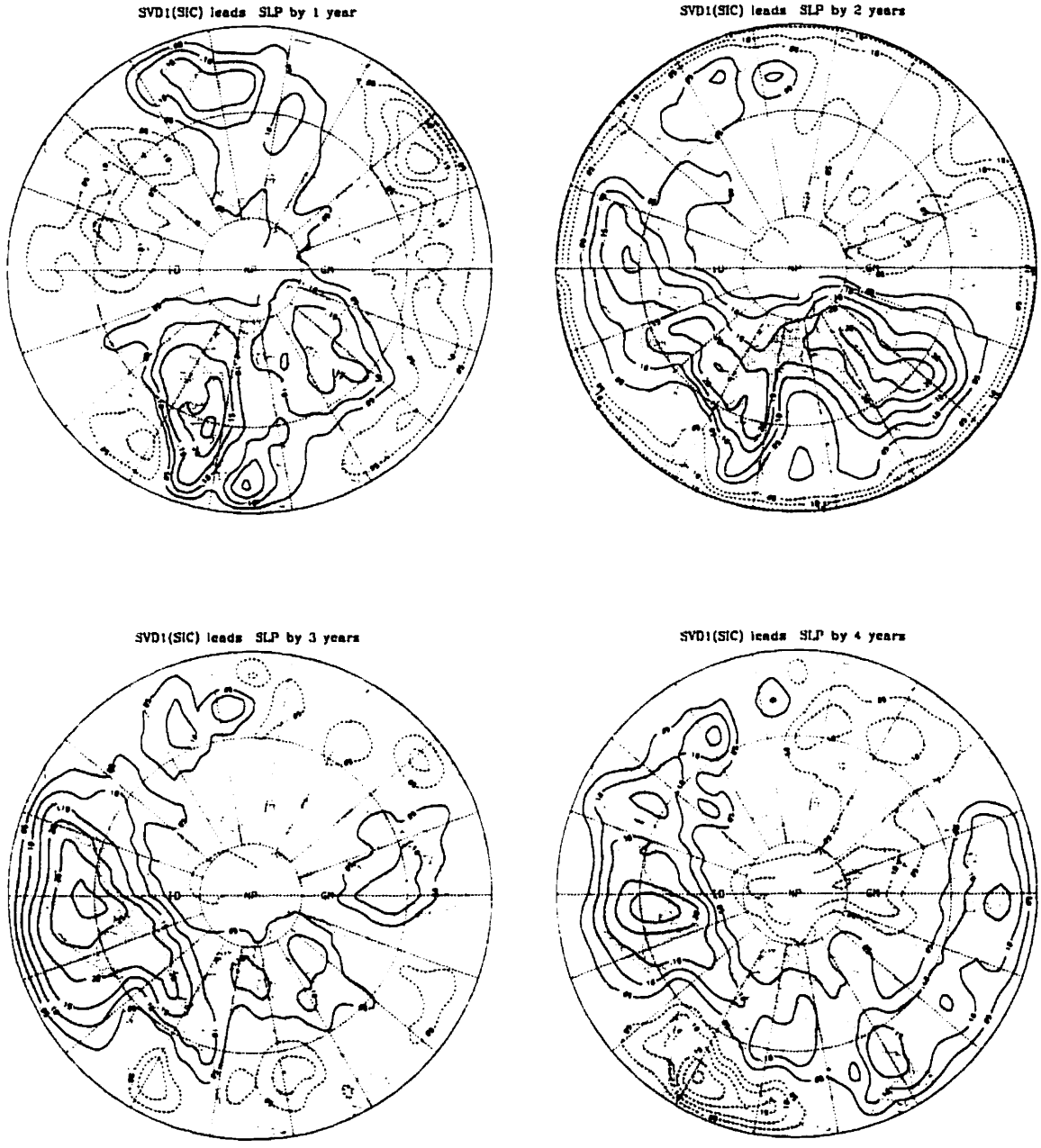

Figure 18: Same as in Fig. 16 , but with sea ice leading the atmosphere by 1 to 4 years.

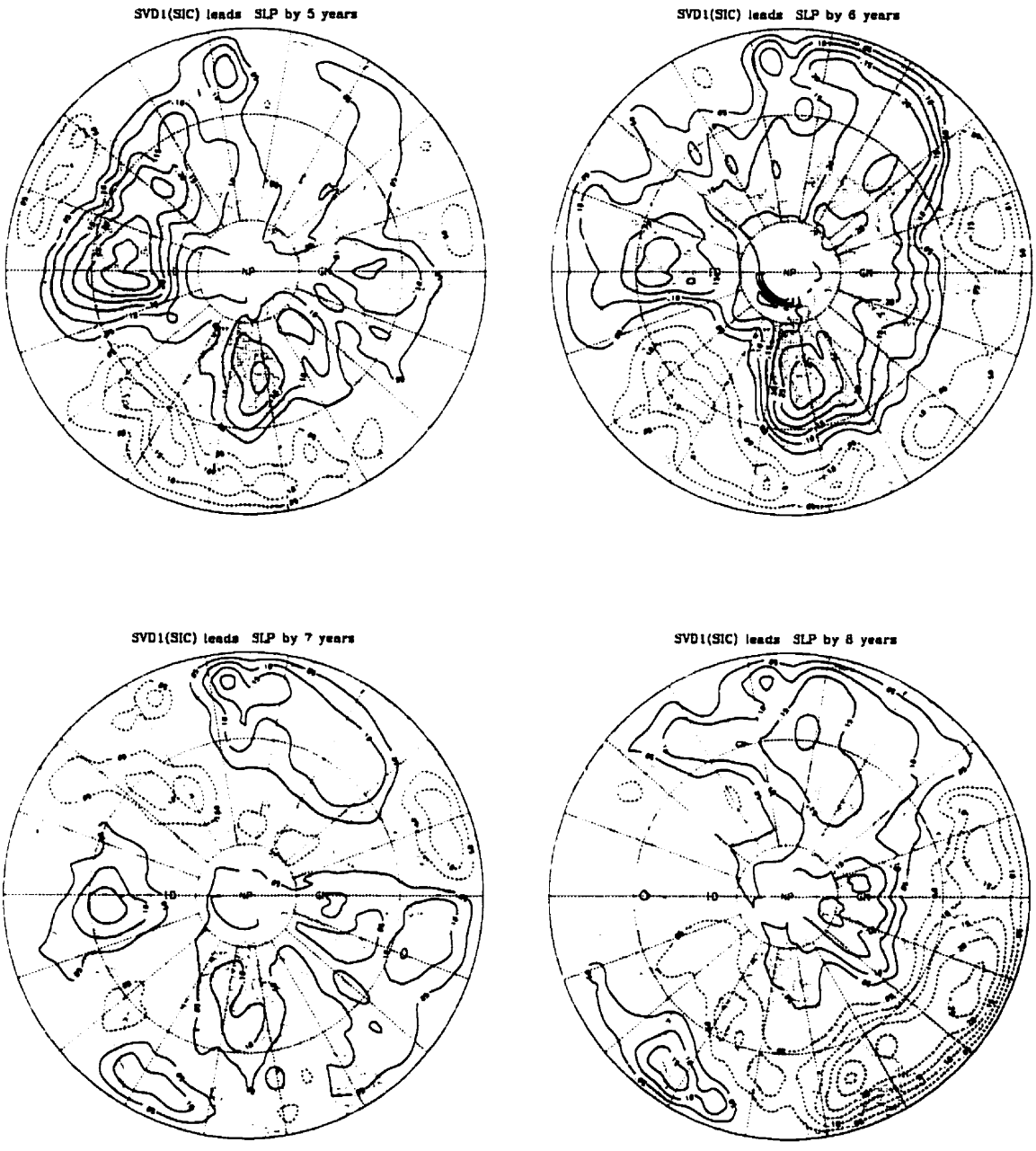

Figure 19: Same as in Fig. 16, but with ice leading the atmosphere by 5 to 8 years.

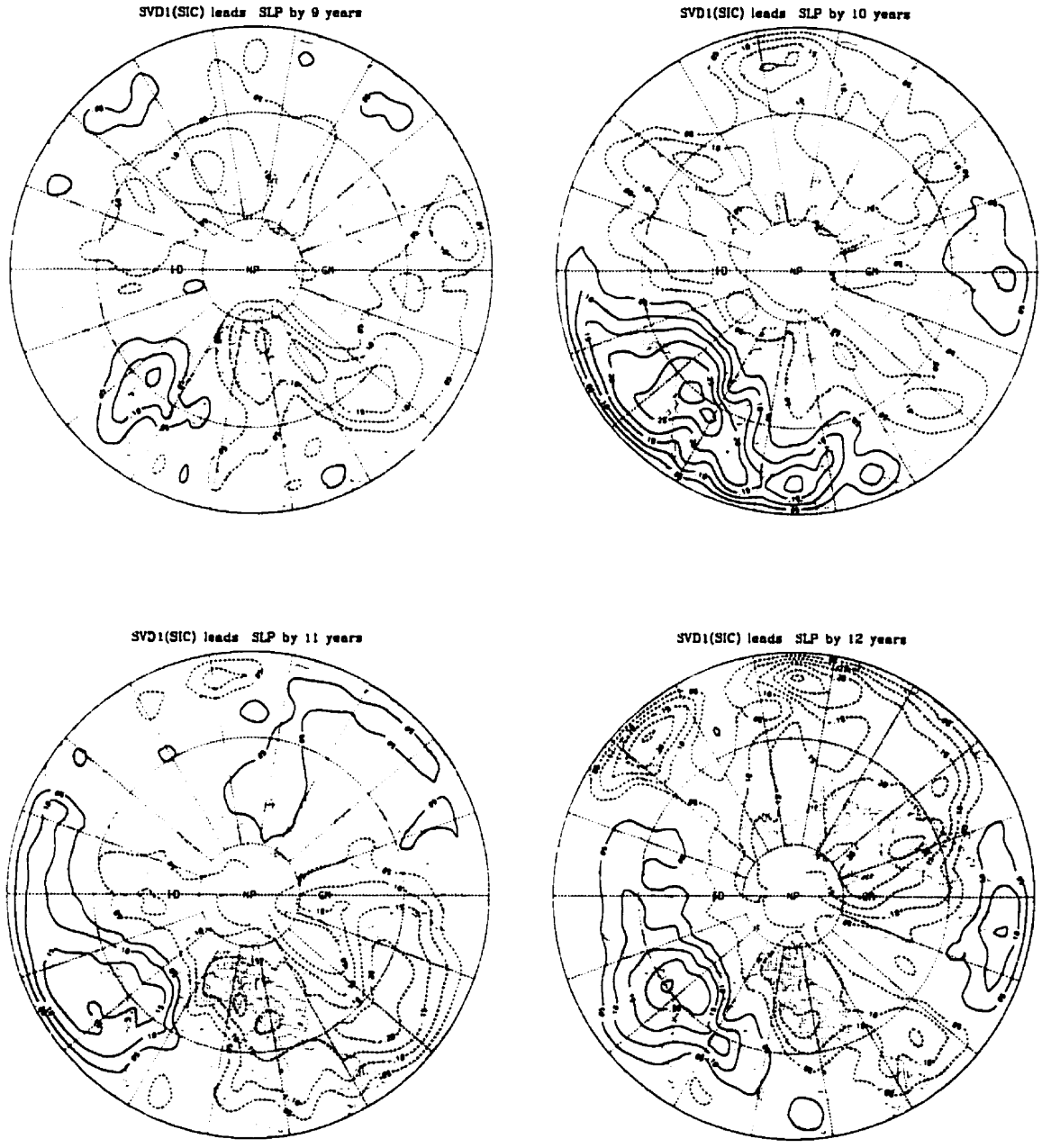

Figure 20: Same as in Fig. 16, but with ice leading the atmosphere by 9 to 12 years.

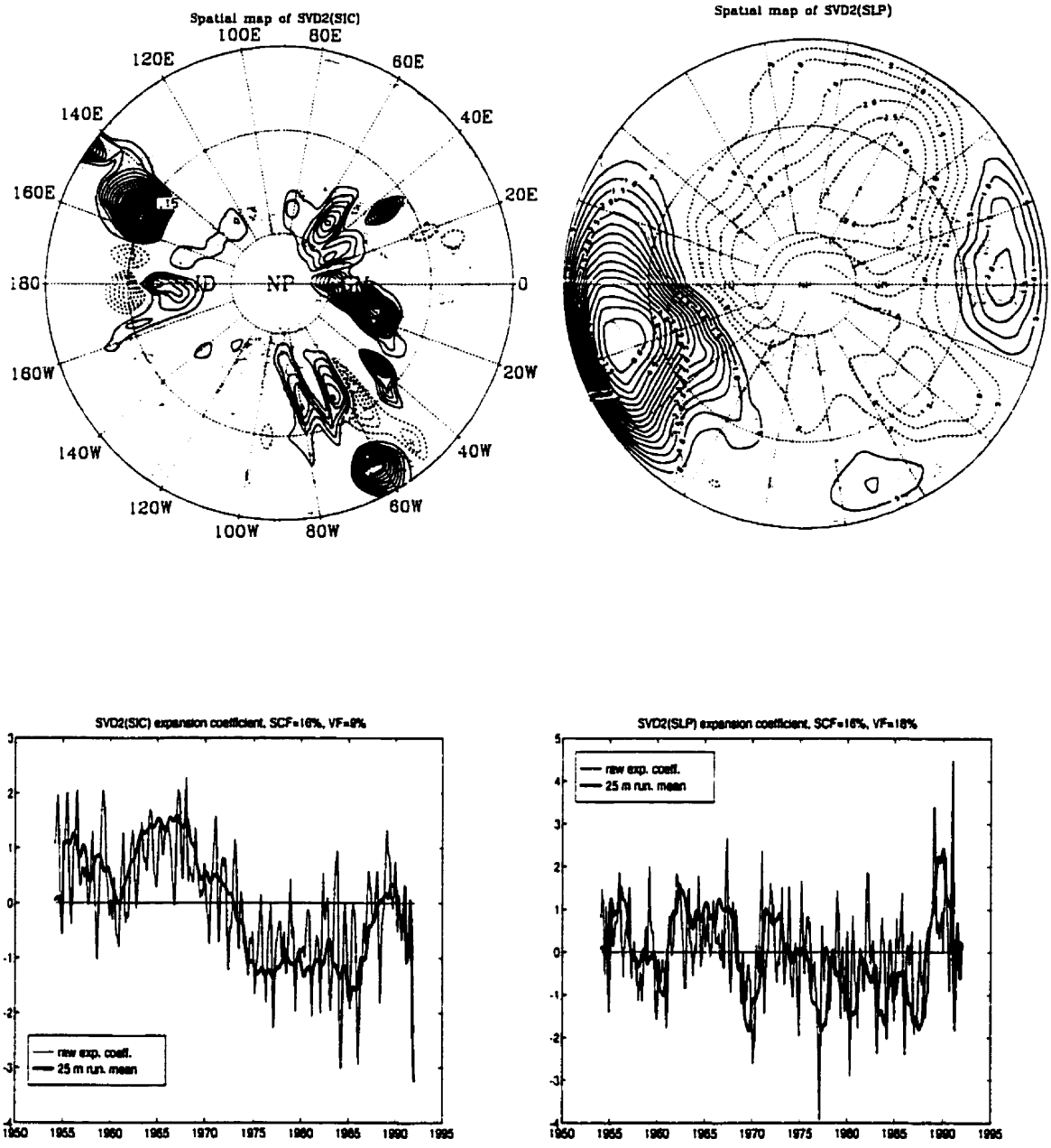

Figure 21: Spatial patterns and expansion time coefficients of SVD_2. Conventions are as in Fig. 3.

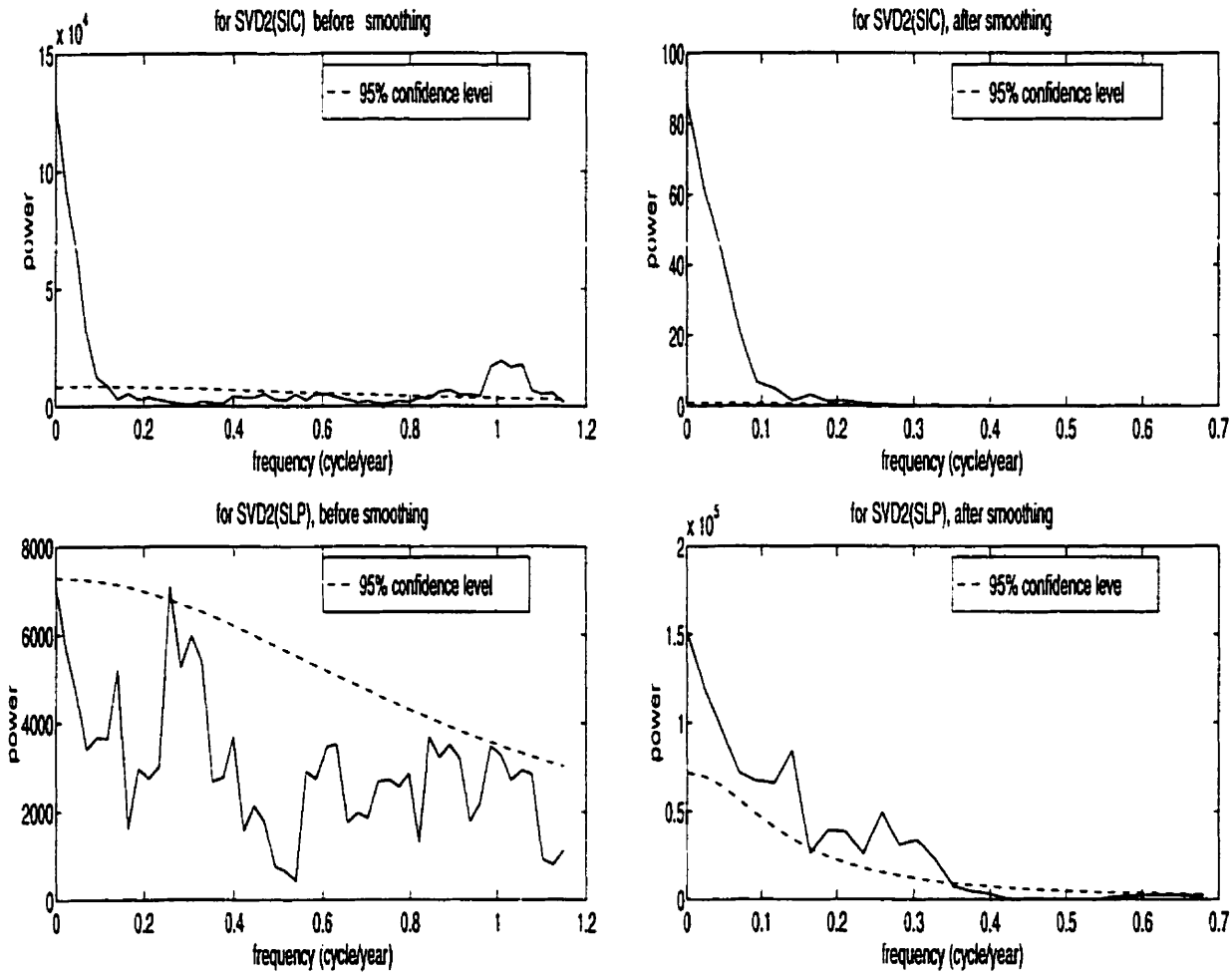

Figure 22: Power spectra of expansion time coefficients of SVD_2(SIC) (top two) and SVD_2(SLP) (bottom two). Conventions are as in Fig. 9.

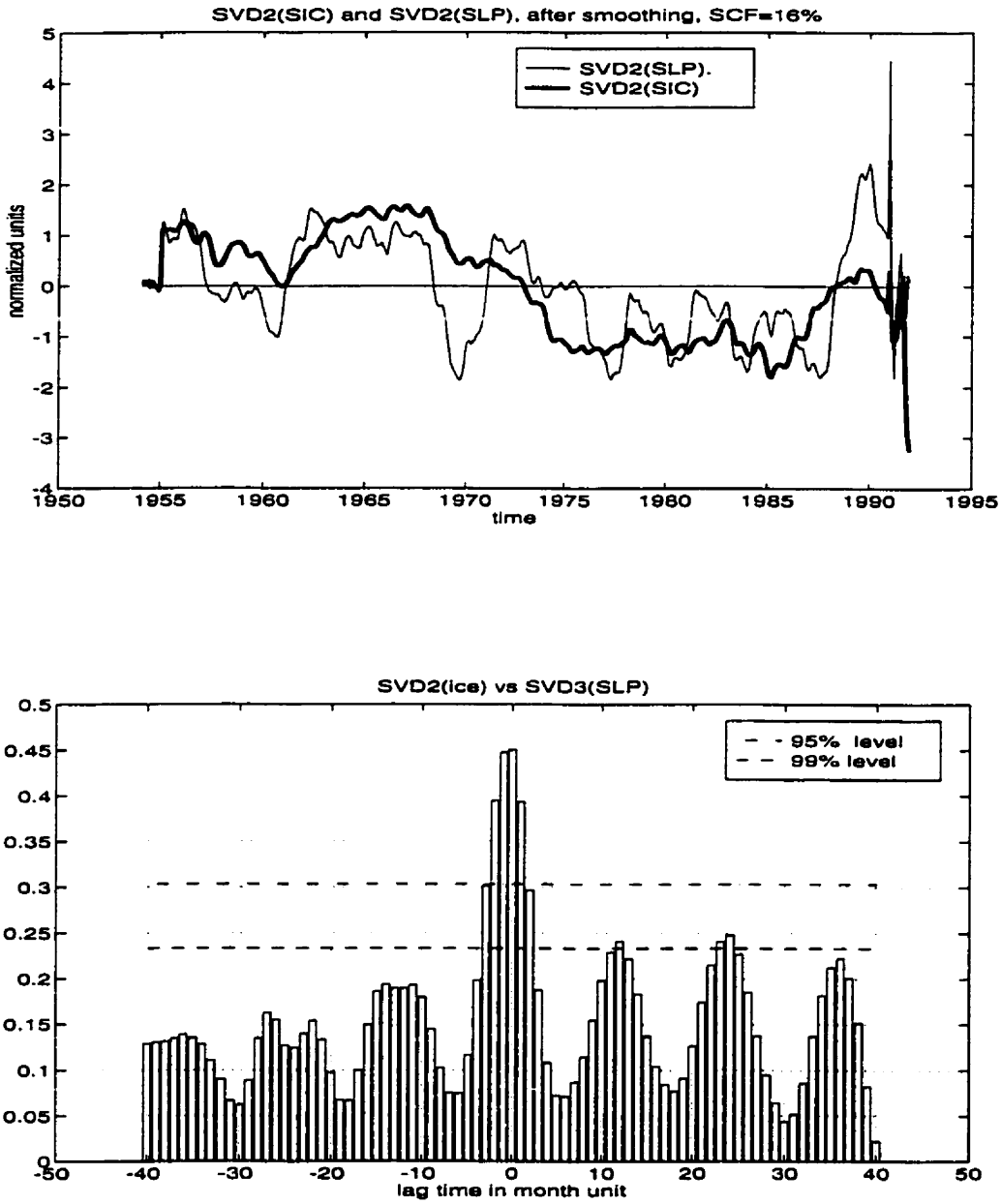

Figure 23: Top: smoothed time coefficients for SVD_2(SIC) and SVD_2(SLP). bottom: the temporal lag-correlation coefficients between the unsmoothed expansion coefficients of SVD_2(SIC) and SVD_2(SLP). Conventions are as in Fig. 10.

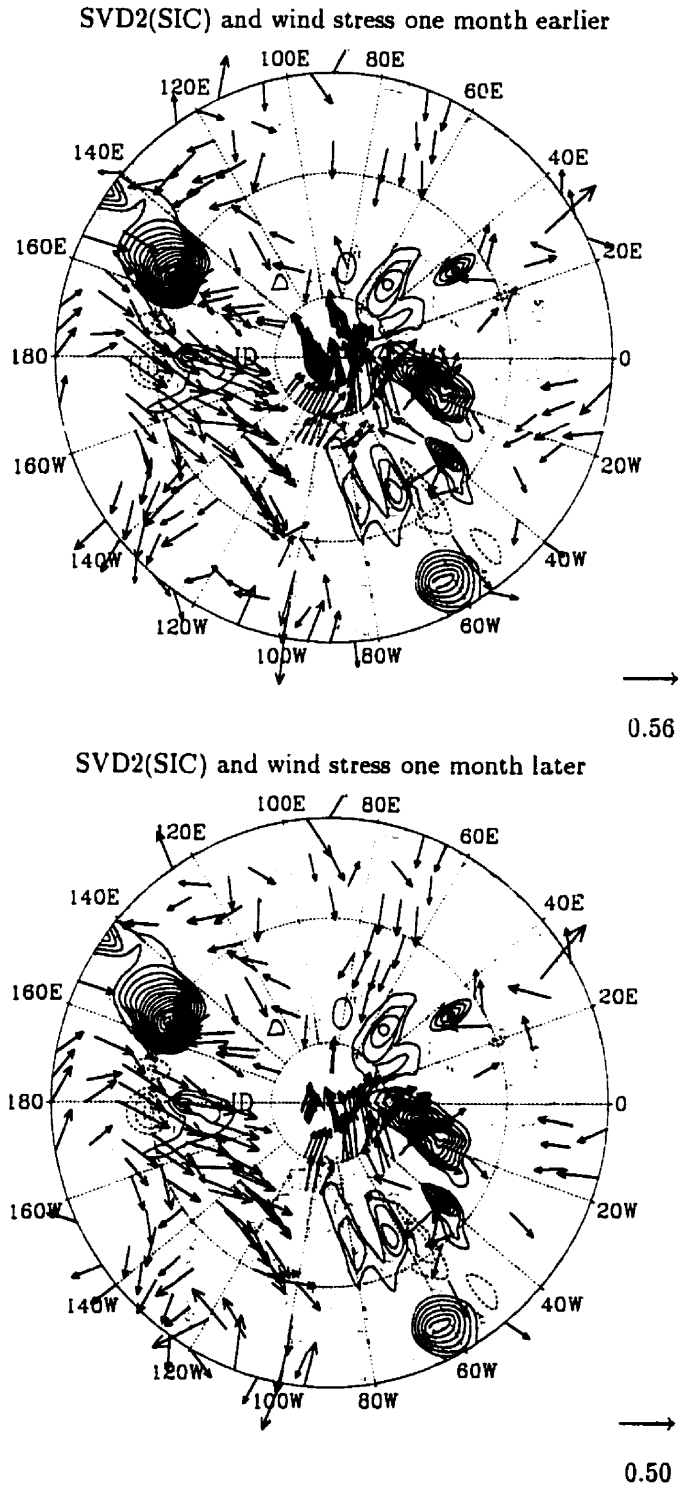

Figure 24: Wind stress anomalies associated with SVD_2(SIC). SVD_2(SIC) is the same as in Fig. 21. Conventions are as in Fig. 11. The lag-relationships between ice and wind stress are shown at the top of each map.

Composite SVD2(SLP) 2 months before
heavy ice conditions in the Sea of Okhotsk

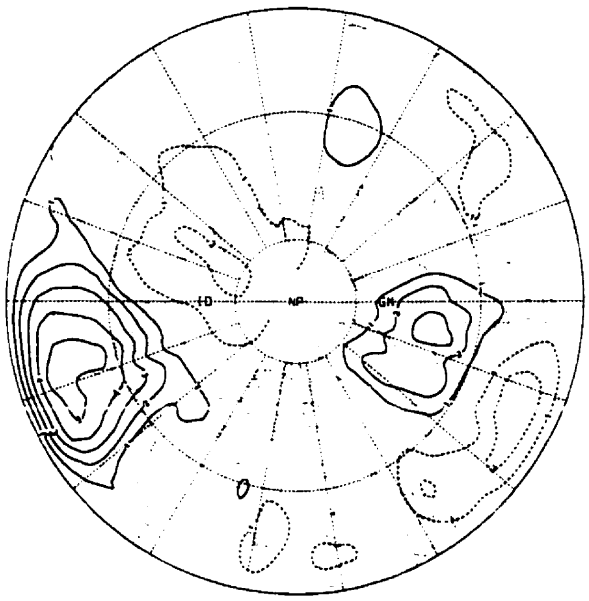

Composite SVD2(SLP) 2 months before
light ice conditins in the Sea of Okhotsk

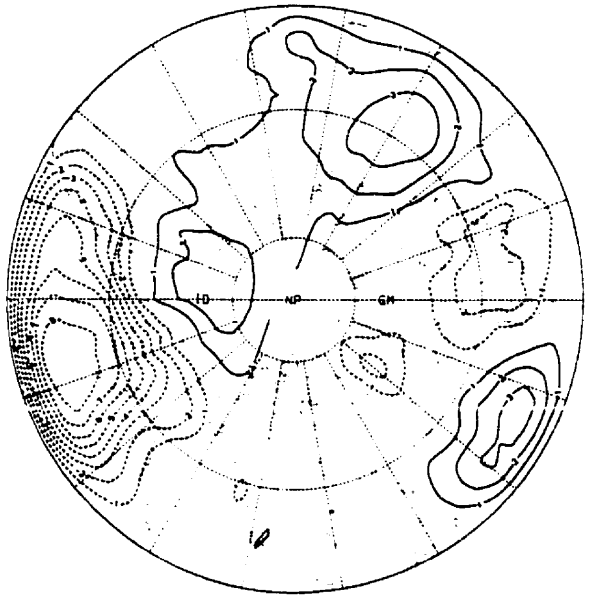

Composite SVD2(SLP) 2 months after,
heavy ice conditins in the Sea of Okhotsk

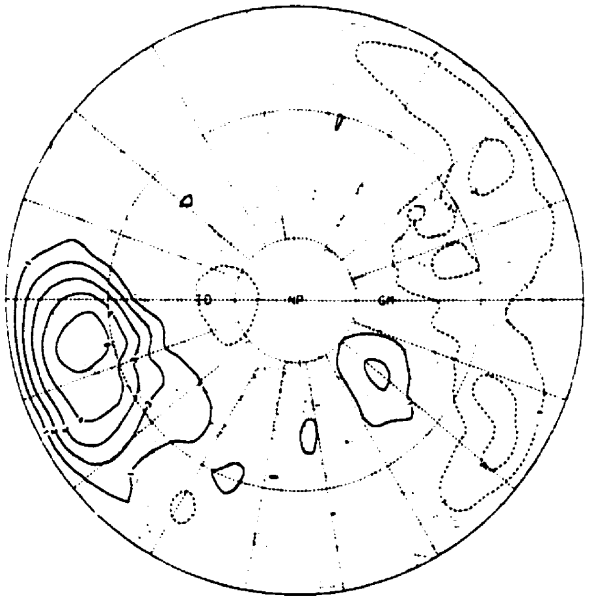

Composite SVD2(SLP) 2 months after
light ice conditions in the Sea of Okhotsk

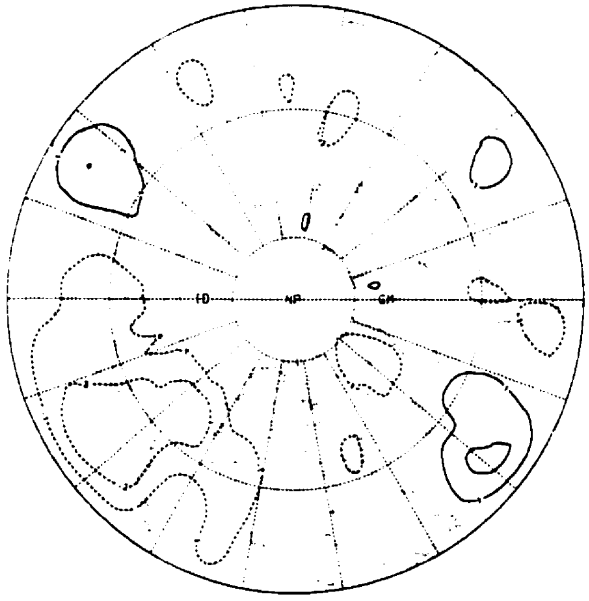

Figure 25: Composite maps of SLP anomalies based on SVD_2(SIC). Left-top: with SLP leading heavy ice conditions by two months in the Sea of Okhotsk and the BNGI regions. Right-top: with SLP leading light-ice conditions by two months. Left-bottom: with SLP lagging heavy-ice conditions by two months. Right-bottom: with SLP lagging light-ice conditions by two months.

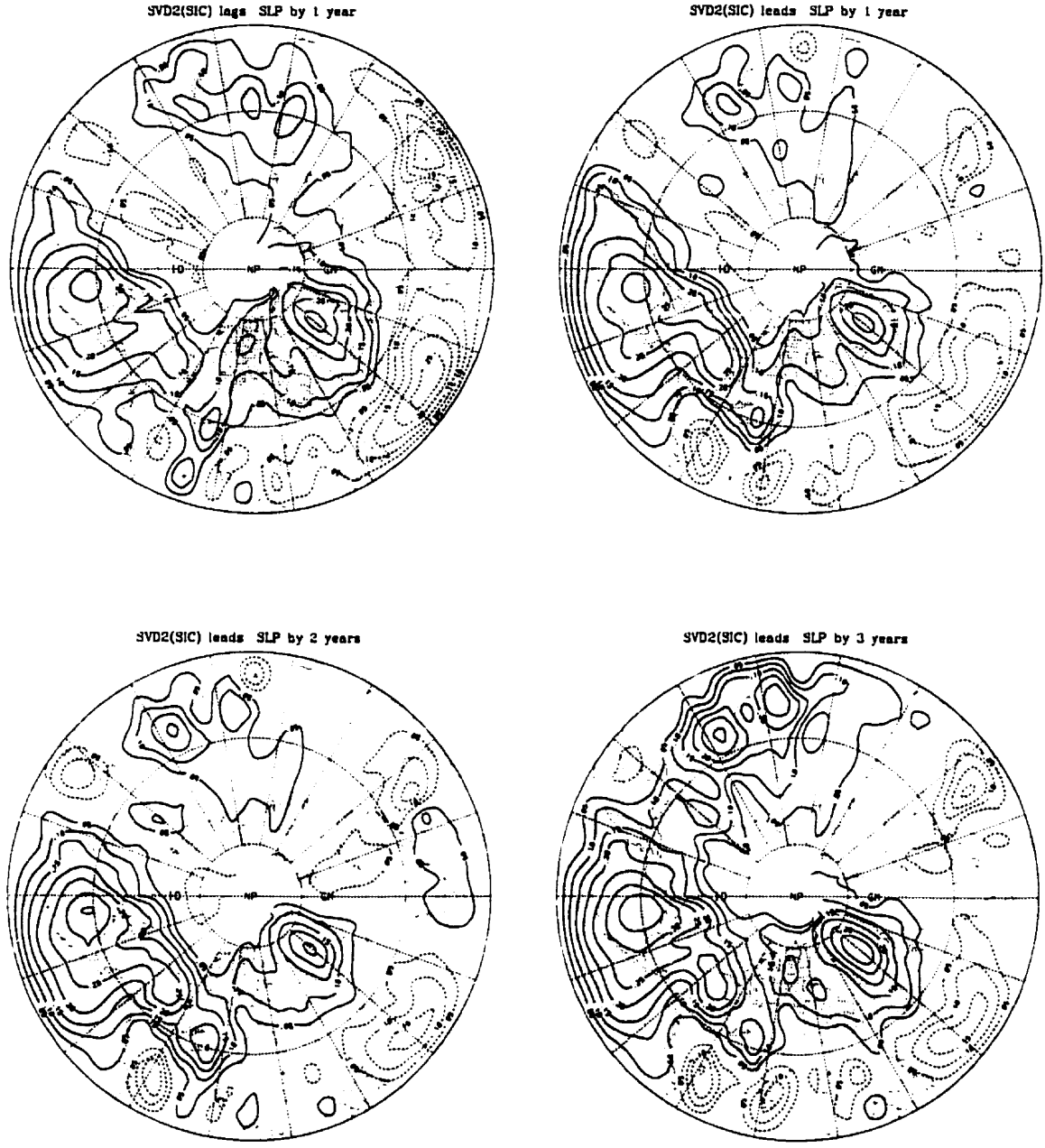

Figure 26: Same as Fig. 16, but between the time series of the expansion coefficient of SVD_2(SIC) and the time series of the SLP anomalies at each grid point, with the atmosphere leading ice by 1 year to the atmosphere lagging ice by 3 years. The length of the lag is shown at the top of each map. Conventions are as in Fig. 16.

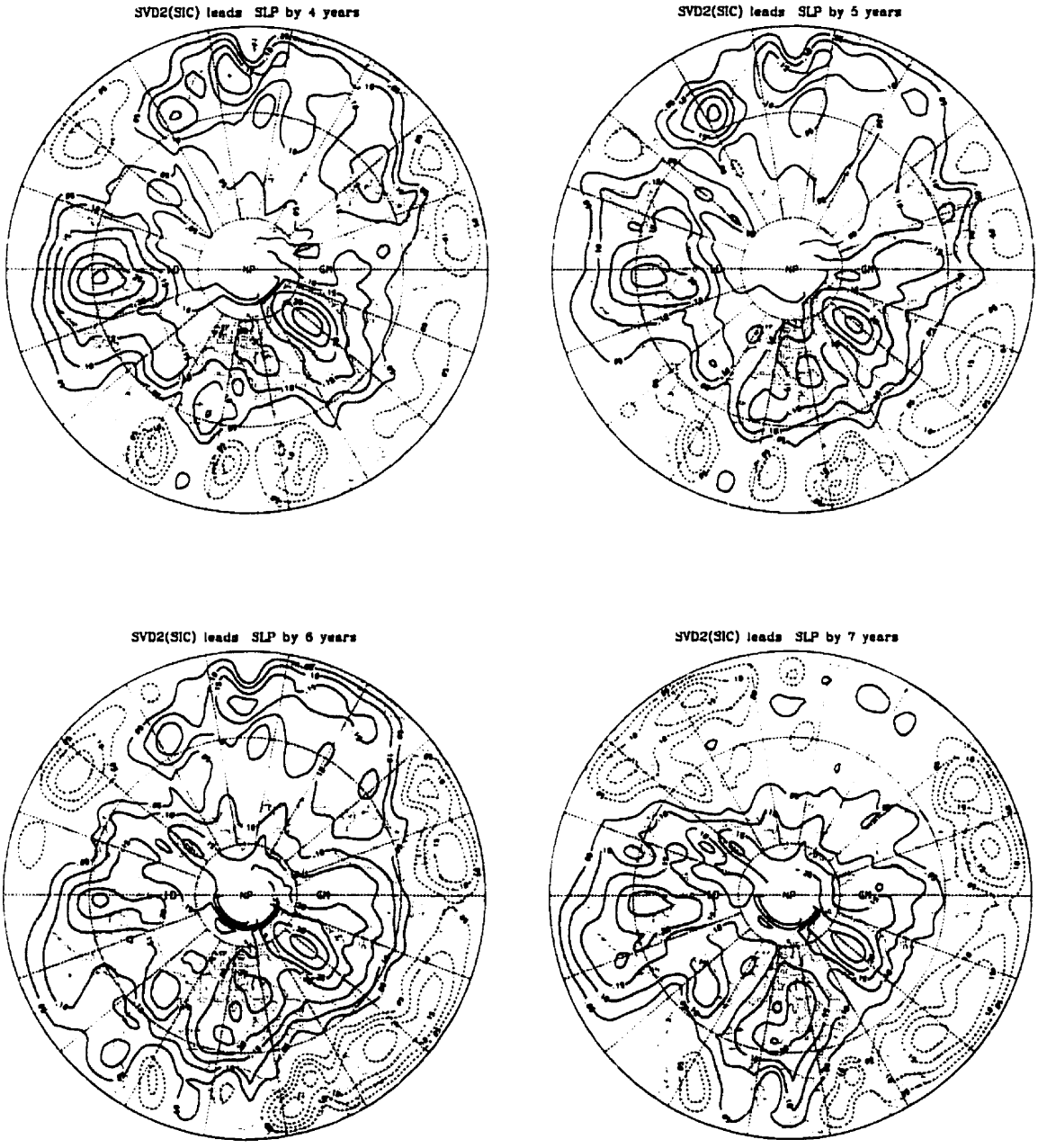

Figure 27: Same as in Fig. 26, but with the atmosphere lagging ice by 4 to 7 years.

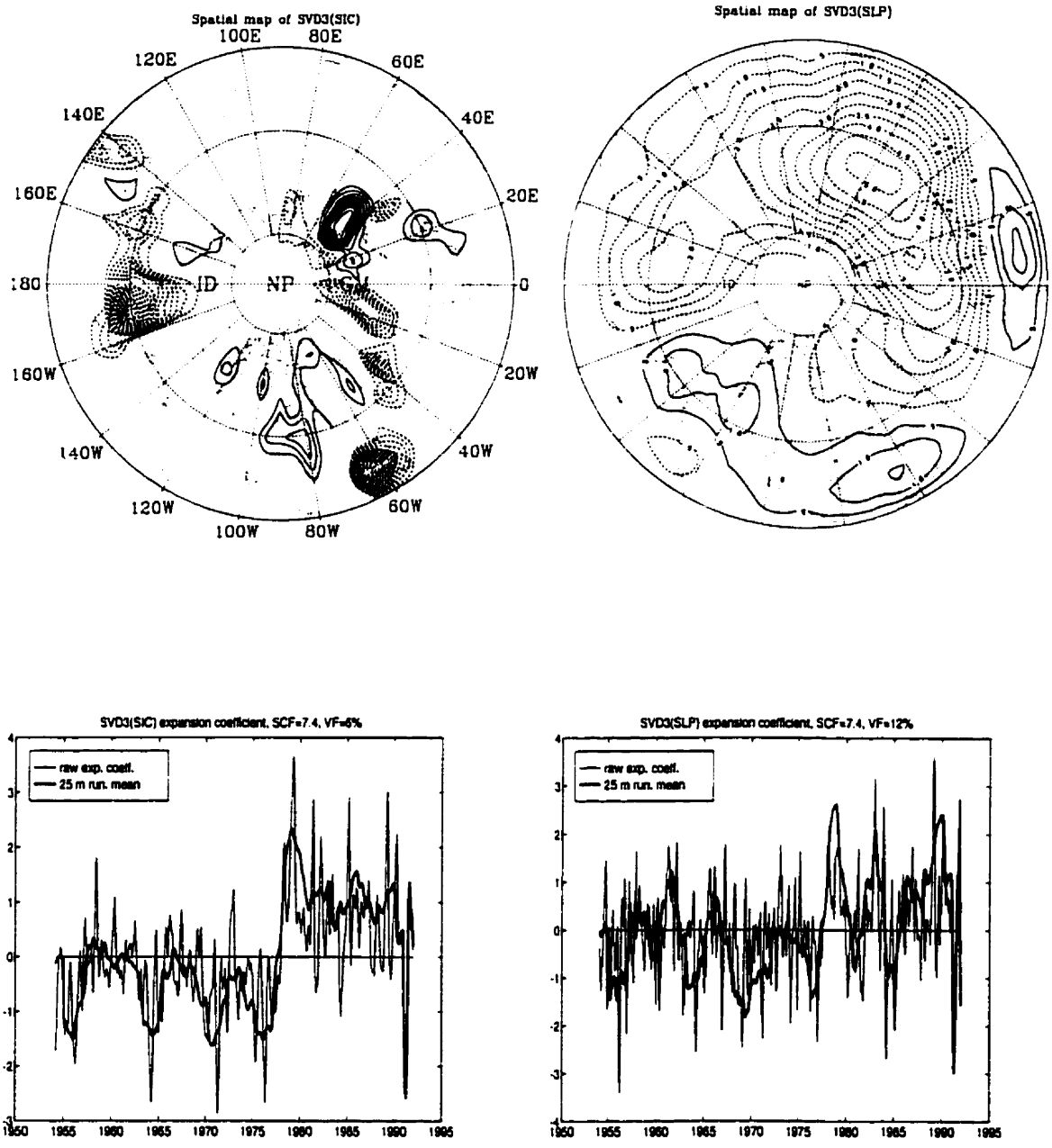

Figure 28: Spatial patterns and time coefficients of SVD_3(SIC) and SVD_3(SLP). Conventions are as in Fig. 3.

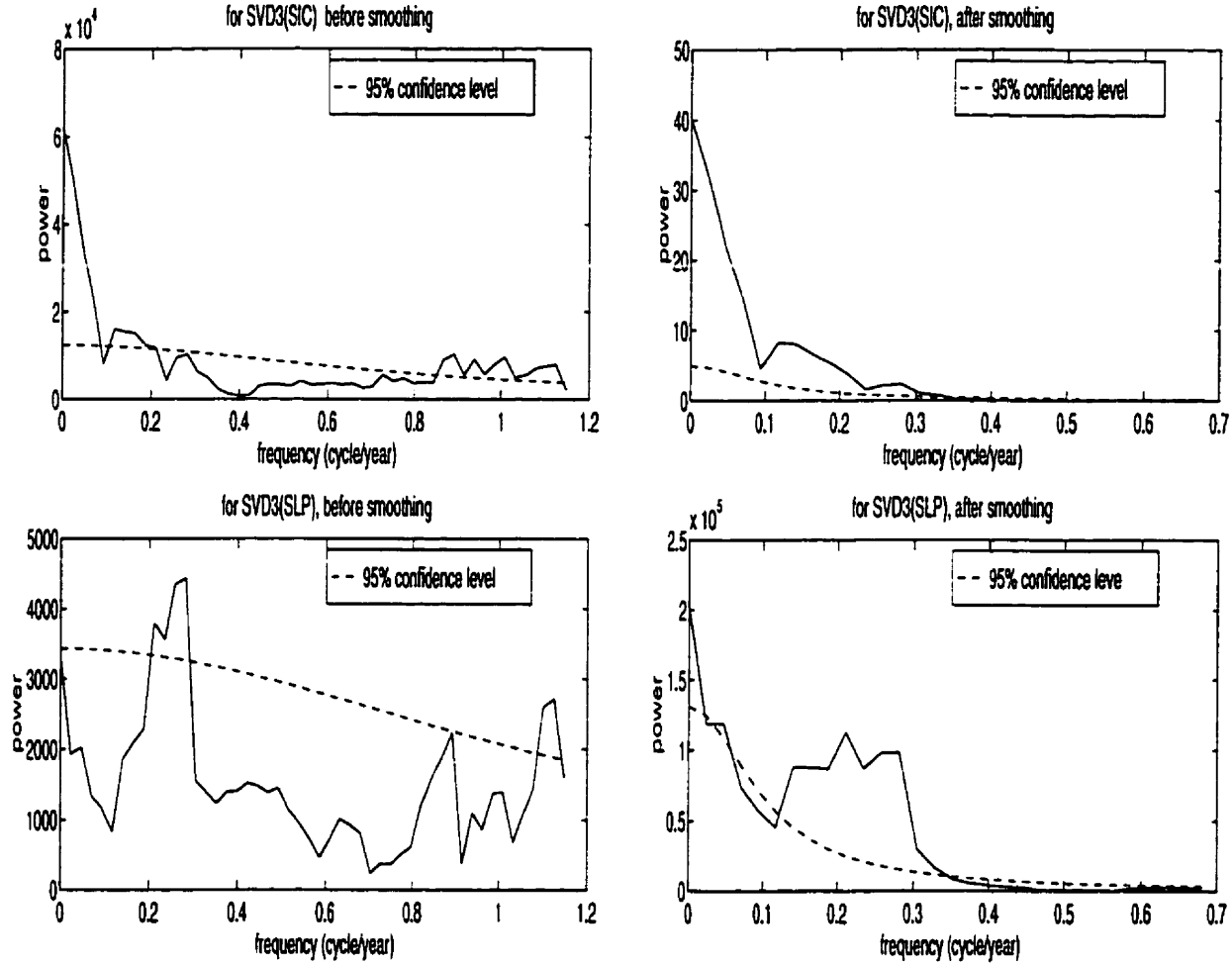

Figure 29: Power spectra of the smoothed and unsmoothed expansion time coefficients of SVD_3(SIC) (top two) and SVD_1(SLP) (bottom two). Conventions are as in Fig. 9.

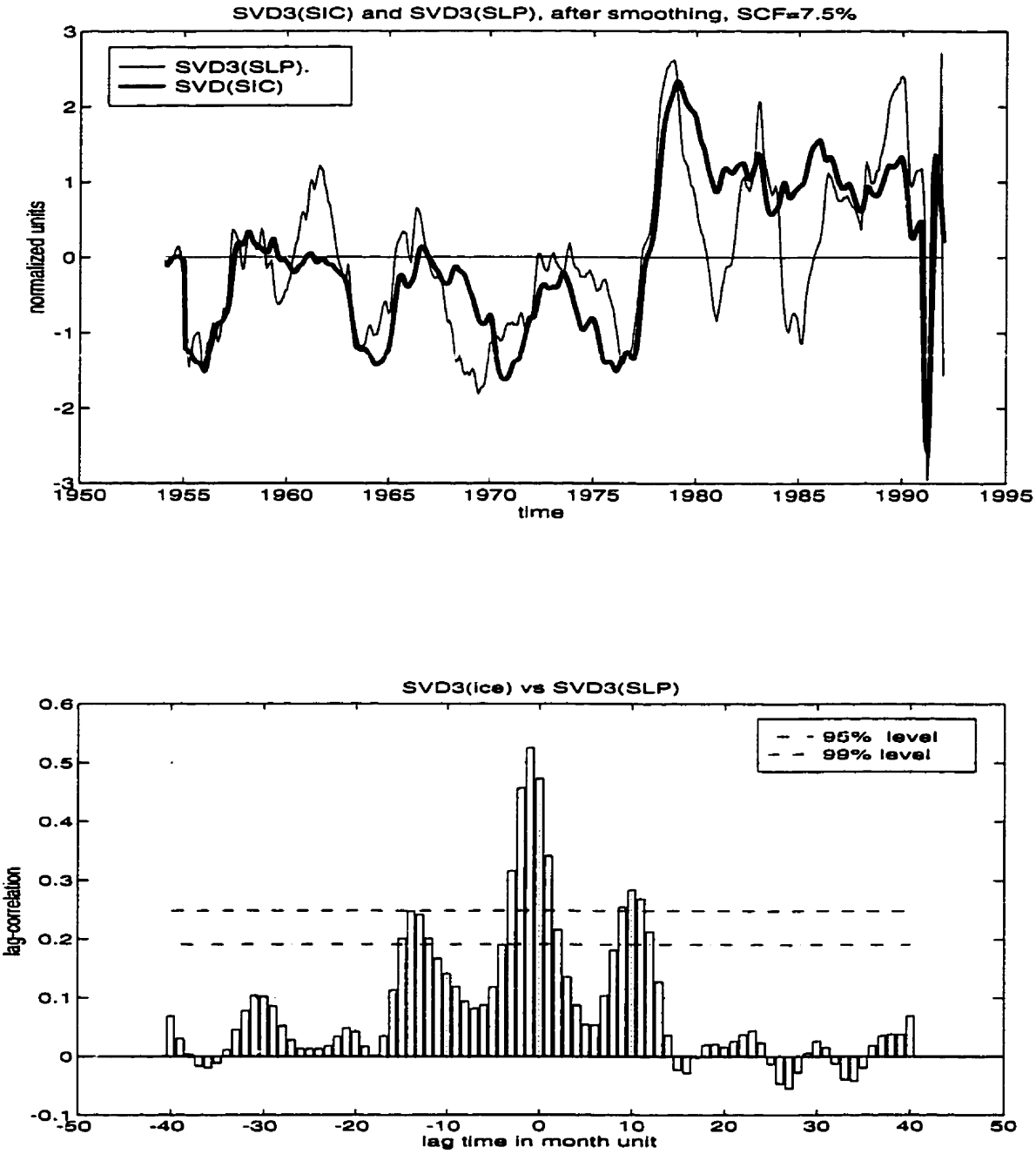

Figure 30: Top: smoothed time coefficients of SVD_3(SIC) and SVD_3(SLP). Bottom: the temporal lagged-correlations between SVD_3(SIC) and SVD_3(SLP). Conventions are as in Fig. 10.

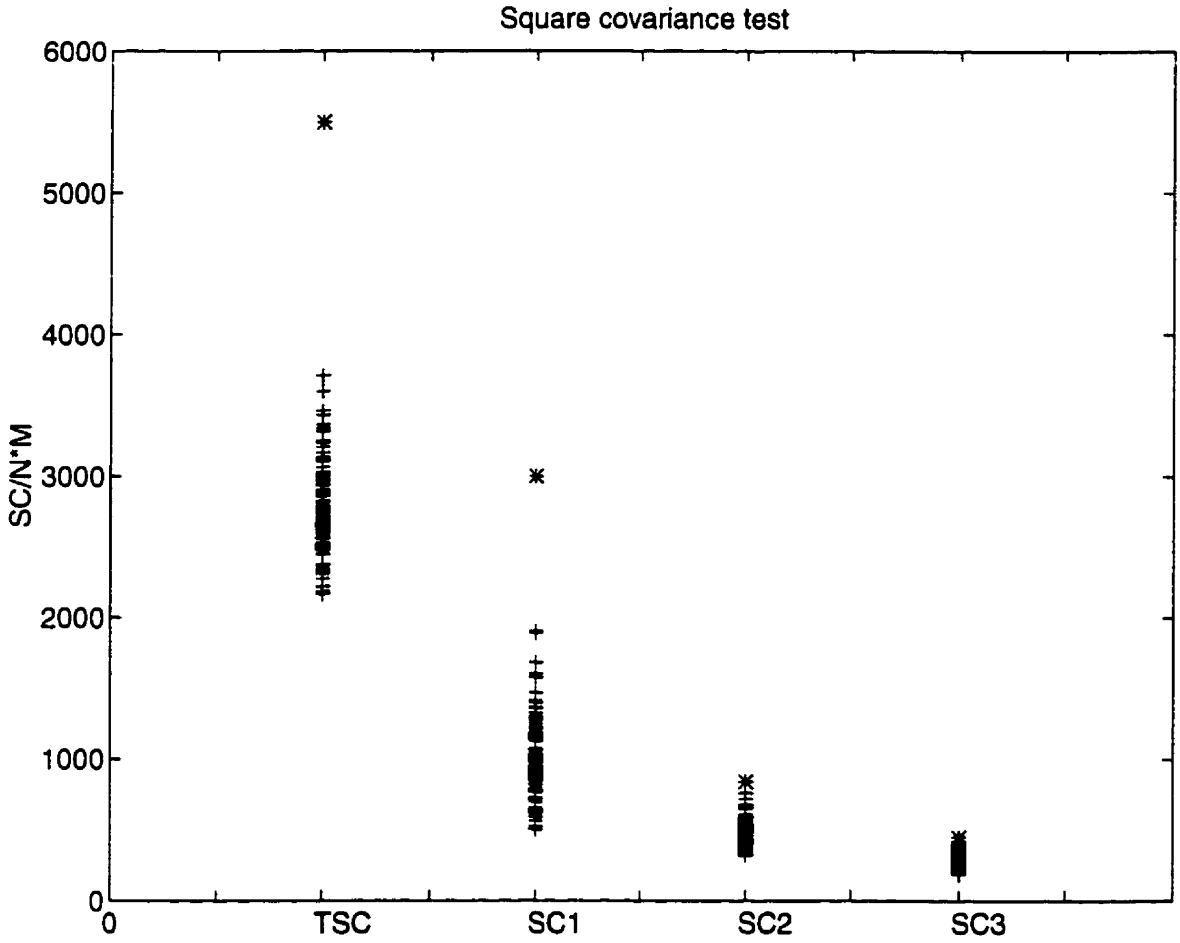

Figure 31: Results of the Monte Carlo test on the total square covariance (TSC) and the square covariance (SC) accounted for by the first three SVD modes from the observed SIC and SLP data sets (asterisks) and from the 100 scrambled data sets (crosses). All the SCs are normalized by dividing by the number of grid points of each variable (NxM = 458x720).

Bibliography

AGNEW, T. (1993). Simultaneous winter sea-ice and atmospheric circulation anomaly patterns. *Atmosphere-Ocean*, 31: 259–280.

BELKIN, I. M., LEVITUS, S., AND ANTONOV, J. (1998). 'Great Salinity Anomalies' in the North Atlantic. *Progress in Oceanography*. in press.

BJORNSSON, H. AND VENEGAS, S. A. (1997). A Manual for EOF and SVD Analyses of Climatic Data. Report 97-1, Centre for Climate and Global Change Research (CCGCR), McGill University, Montreal.

BRETHERTON, C. S., SMITH, C., AND WALLACE, J. M. (1992). An intercomparison of methods for finding coupled patterns in climate data. *Journal of Climate*, 5: 541–560.

BRYAN, F. (1986). High-latitude salinity effects and interhemispheric thermohaline circulations. *Nature*, 323: 301–304.

CHAPMAN, W. L. AND WALSH, J. E. (1993). Recent variations of sea ice and air temperature in high latitudes. *Bulletin of the American Meteorological Society*, 74: 33–47.

COLBOURNE, E., DEYOUNG, E., NARAYANAN, S., AND HELBIN, J. (1997). Comparison of hydrography during winter: 1900–1989. *Journal of Climate*, 6: 1743–1753.

DESER, C. AND BLACKMON, M. L. (1993). Surface climate variations over the North Atlantic Ocean during winter: 1900-1989. *Journal of Climate*, 6: 1743–1753.

DESER, C. AND TIMLIN, M. S. (1996). Decadal variations in sea ice and sea surface temperature in the subpolar North Atlantic, in: The Atlantic Climate Change Program, Proceedings From the Principal Investigators Meeting. *WHOI, Woods Hole, MA*.

DICKSON, R., MEINCKE, J., MALMBERG, S., AND LEE, A. (1988). The 'Great Salinity Anomaly' in the northern North Atlantic, 1968–1982. *Progress in Oceanography*, 20: 103–151.

DRINKWATER, K. (1994). Climate and oceanographic variability in the northwest atlantic during the 1980s and early 1990s. *NAFO SCR Doc.*, 94: 39.

FANG, Z. AND WALLACE, J. M. (1994). Arctic sea ice variability on a timescale of weeks and its relation to atmospheric forcing. *Journal of Climate*, 7: 1897–1913.

GLOWIENKA-HENSE, R. (1995). GCM response to an Antarctic Polynya. *Beitrage zur Physik der Atmosphare*, 68: 303–317.

GLOWIENKA-HENSE, R. AND HENSE, A. (1992). The effect of an Arctic polynya on the Northern Hemisphere mean circulation and eddy regime: a numerical experiment. *Journal of Climate*, 7: 155–163.

HERMAN, G. AND JOHNSON, W. (1978). The sensitivity of the general circulation to arctic sea ice boundaries: A numerical experiment. *Monthly Weather Review*, 106: 1649–1664.

HONDA, M., YAMAZAKI, K., TACHIBANA, Y., AND TAKEUCHI, K. (1996). Influence of Okhotsk sea-ice extent on atmospheric circulation. *Geophysical Research Letters*, 23: 3595–3598.

KNOX, J. L., HIGUCHI, K., SHABBAR, A., AND SARGENT, N. E. (1988). Secular variation of Northern Hemisphere 50 kPa geopotential height. *Journal of Climate*, 1: 500–511.

KOIDE, H. AND MOTOI, T. (1998). Decadal variability of the northern hemisphere sea-ice concentration during winter. *Geophysical Research Letters*. submitted.

MALMBERG, S. A. (1969). Hydrographic changes in the waters between Iceland and Jan Mayen in the last decade. *Jokull*, 19: 30–43.

MALMBERG, S. A. AND KRISTMANNSSON, S. S. (1992). Hydrographic conditions in Icelandic waters. *ICES Marine Science Symposia*, 195: 76–92.

MALMBERG, S. AND BLINDHEIM, J. (1994). Climate, cod and capelin in Northern Waters. *ICES Climate,Cod, and Capelin Symposium*, 198: 297–310.

MALMBERG, S., VALDIMARSSON, H., AND MORTENSEN, J. (1994). Long time series in Icelandic waters. *Ices C.M.*, S:8.

MALMBERG, S., VALDIMARSSON, H., AND MORTENSEN, J. (1996). Long time series in Icelandic waters in relation to physical variability in the northern North Atlantic. *NAFO Scientific Council Studies*, 24: 69–80.

MANABE, S. AND STOUFFER, R. J. (1994). Multiple-century response of a coupled ocean-atmosphere model to an increase of atmospheric carbon dioxide. *Journal of Climate*, 7: 5–23.

MANN, M. E. AND PARK, J. (1993). Spatial correlations of interdecadal variation in global surface temperatures. *Geophysical Research Letters*, 20: 1055–1058.

MYSAK, L. A. (1998). Interdecadal variability at northern high latitudes. In NAVARRA, A., editor, *Beyond El Nino: Decadal Variability in the Climate System*. Springer-Verlag.

MYSAK, L. A. AND MANAK, D. K. (1989). Arctic Sea-Ice Extent and Anomalies, 1953-1984. *Atmosphere-Ocean*, 27: 376–405.

MYSAK, L. A., MANAK, D. K., AND MARSDEN, R. F. (1990). Sea ice anomalies observed in the Greenland and Labrador Seas during 1901-1984 and their relation to an interdecadal Arctic climate cycle. *Climate Dynamics*, 5: 111–133.

MYSAK, L. A. AND POWER, S. B. (1991). Greenland Sea ice and salinity anomalies and interdecadal climate variability. *Climatological Bulletin*, 25: 81–91.

MYSAK, L. A. AND POWER, S. B. (1992). Sea-ice anomalies in the western Arctic and Greenland-Iceland sea and their relation to an interdecadal climate cycle. *Climate Bulleti*, 26: 147–176.

NORTH, G. R., BELL, T. L., CAHALAN, R. F., AND MOENG, F. J. (1982). Sampling errors in the estimation of empirical orthogonal functions. *Monthly Weather Review*, 110: 699–706.

PEIXOTO, J. P. AND OORT, A. H. (1992). *Physics of Climate.* American Institute of Physics, New York.

PENG, S. AND FYFE, J. (1996). The coupled patterns between sea level pressure and sea surface temperature in the mid-latitude North Atlantic. *Journal of Climate*, 9: 1824–1839.

POUNDER, E. R. (1965). *The Physics of Ice.* Pergamon Press, London.

PRINSENBERG, S., PETERSON, I.K., N., S., AND UMOH, J. (1996). Interaction between atmosphere, ice cover and ocean along Canada's east coast for 1962-1992. *Canadian Journal of Fisheries and Aquattic Sciences*, 53.

PROSHUTINSKY, A. AND JOHNSON, M. (1997). Two circulation regimes of the wind-driven Arctic ocean. *Journal of Geophysical Research*, 102: 12,493–12,514.

SCIREMAMMANO, F. (1979). A suggestion for the presentation of correlations and their significance levels. *Journal of Physical Oceanography*, 9: 1273–1276.

SERREZE, M. AND BARRY, R. (1988). Synoptic activity in the Arctic Basin, 1979-1985. *Journal of Climate*, 1: 1276–1259.

SERREZE, M. AND MCLAREN, A. (1989). Seasonal variations in sea ice motion and effects on sea ice concentration in the Canada Basin. *Journal of Geophysical Research*, 94: 955–970.

SLONOSKY, V. C. (1996). Arctic Sea Ice and Atmospheric Circulation Anomalies Since 1954. Master's thesis, McGill University, Montreal, P.Q., Canada. Also available as Report 96-14, Center for Climate and Global Change Research (CCGCR), McGill University, Montreal.

SLONOSKY, V. C., MYSAK, L. A., AND DEROME, J. (1997). Linking Arctic Sea-Ice and Atmospheric Circulation Anomalies on Interannual and Decadal Timescales. *Atmosphere-Ocean*, 35: 333–366.

STEWART, G. (1973). *Introduction to Matrix Computations*. Academic Press.

STRANG, G. (1988). *Linear Algebra and its Applications*. Harcourt, Brace and Jovanovitch.

TANG, B., FLATO, G. M., AND HOLLOWAY, G. (1994). A study of Arctic sea ice and sea level pressure using POP and Neural Network methods. *Atmosphere-Ocean*, 32: 507–529.

THORNDIKE, A. AND COLONY, R. (1982). Sea ice motion response to geostrophic winds. *Journal of Geophysical Research*, 87: 5845–5852.

TREMBLAY, L. B. AND MYSAK, L. A. (1997). Modeling Sea Ice as a Granular Material, Including the Dilatancy Effect. *Journal of Physical Oceanography*, 27: 2342–2360.

TREMBLAY, L. B. AND MYSAK, L. A. (1998). On the origin and evolution of sea-ice anomalies in the Beaufort-Chukichi Sea. *Climate Dynamics.* in press.

VENEGAS, S. A., MYSAK, L. A., AND STRAUB, D. N. (1996). Evidence for interannual and interdecadal climate variability in the South Atlantic. *Geophysical Research Letters*, 23: 2673–2676.

VENEGAS, S. A., MYSAK, L. A., AND STRAUB, D. N. (1997). Atmosphere-ocean coupled variability in the South Atlantic. *Journal of Climate*, 10: 2904–2920.

WALLACE, J. M., SMITH, C., AND BRETHERTON, C. S. (1992). Singular value decomposition of wintertime sea surface temperature and 500-mb height anomalies. *Journal of Climate*, 5: 561–576.

WALSH, J. E. (1983). The role of sea ice in climatic variability: theories and evidence. *Atmosphere-Ocean*, 21(3): 229–242.

WALSH, J. E. AND CHAPMAN, W. L. (1990). Arctic contribution to upper-ocean variability in the North Atlantic. *Journal of Climate*, 3: 1462–1473.

WALSH, J. E. AND JOHNSON, C. M. (1979a). An analysis of Arctic sea ice fluctuations. *Journal of Physical Oceanogrphy*, 9: 580–591.

WALSH, J. E. AND JOHNSON, C. M. (1979b). Interannual atmospheric variability and associated fluctuations in Arctic sea ice extent. *Journal of Geophysical Research*, 84: 6915–6928.

WALSH, J. (1994). A sea-ice data base. In FOLLAND AND ROWELL, editors, *Workshop on simulations of the climate of the twentieth century using GISST*, volume 56, pages 54–55, London Road, Bracknell, Berkshire, U.K. Hadley Centre.

YASHAYAEV, I. M. (1995). Annual and interannual variability of temperature and salinity in the Newfoundland Basin. *The Abstracts of the XXI General Assembly of the IAPSO, August 5–12, 1995, Hawaii.*